

# How sensitive are sediment dispersal and sea surface temperature to changing wind conditions?

---

A mapping approach in the coastal waters of Herschel Island, Yukon Territory, Canada, using Landsat (TM, ETM+ and OLI/TIRS) satellite image data from 1986 to 2016.

## **Master Thesis**

to attain the academical degree

Master of Science (M.Sc.) in Geoscience

submitted by

**Konstantin Paul Klein**

submitted at

Universität Potsdam

Faculty of Earth and Environmental Science



October 2018

## **Konstantin Paul Klein**

Geboren am 10.März 1992 in Berlin  
Adresse: Posthofstraße 17a, 14467 Potsdam  
Email: konstantinklein92@gmail.com  
Matrikelnummer: 760382

Erstgutachter: **Prof. Dr. Hugues  
Lantuit**

Adresse: AWI Potsdam,  
Telegrafenberg A6,  
14473 Potsdam

Email: Hugues.lantuit@awi.de

Zweitgutachter: **Dr. Frank Fell**

Adresse: Informus GmbH,  
Belziger Straße 44,  
10823 Berlin

Email: fell@informus.de

## Content

---

|  |    |
|--|----|
| 1. Introduction  | 1  |
| 2. Scientific Background   | 5  |
| 2.1 Suspended Sediment Transport in Coastal Waters                                 | 5  |
| 2.2 Turbidity, Suspended Particulate Matter (SPM) and Total Suspended Matter (TSM) | 6  |
| 2.3 Sedimentary transport at the Canadian Beaufort Shelf                           | 7  |
| 2.4 Climate Change and its Consequences in the Arctic                              | 9  |
| 2.5 Knowledge gaps   | 10 |
| 2.6 Landsat satellite remote sensing   | 11 |
| 3. Regional Setting  | 15 |
| 4. Materials & Methods   | 19 |
| 4.1. Landsat Images Acquisition  | 19 |
| 4.2. Landsat Images Pre-Processing   | 19 |
| 4.3. Landsat Images Processing   | 20 |
| 4.4. Boxplots  | 21 |
| 4.5. Wind Data   | 21 |
| 4.6. SPM Algorithms  | 22 |
| 5. Results   | 26 |
| 5.1. Landsat scene processing  | 26 |
| 5.2 Turbidity  | 27 |
| 5.3 Sea Surface Temperature  | 34 |
| 6. Discussion  | 39 |
| 6.1 Acquisition of Wind Data   | 39 |
| 6.2 Significance of the results without <i>in-situ</i> data                        | 40 |
| 6.3 Controlling factors  | 41 |
| 6.4 Comparison to other Modelling Approaches                                       | 43 |

|                                   |    |
|-----------------------------------|----|
| 6.5 Applicability of spatial data | 50 |
| 6.6 Outlook                       | 52 |
| 7. Conclusion                     | 53 |

## List of Figures

---

|   |           |
|---|-----------|
| <u>Figure 1: "Impact of thaw and erosion of Arctic permafrost coasts"</u>   | <u>2</u>  |
| <u>Figure 2: "Global projected change in mean flow for 2071-2100 relative to 1971–2000"</u>   | <u>4</u>  |
| <u>Figure 3: Hjulstrom diagram</u>  | <u>6</u>  |
| <u>Figure 4: "Summary of the principal sediment sources to the Canadian Beaufort Shelf sediment"</u>  | <u>7</u>  |
| <u>Figure 5: Compared Signal – to - Noise Ratio over Water of Landsat TM (left) and Landsat OLI (right)</u>   | <u>14</u> |
| <u>Figure 6: Map of the study area</u>  | <u>17</u> |
| <u>Figure 7: "Wind direction and frequency in the ice-free period (June-September)"</u>   | <u>18</u> |
| <u>Figure 8: "Mean monthly temperature and precipitation for Komakuk Beach and Shingle Point, Yukon Territory"</u>  | <u>18</u> |
| <u>Figure 9: Comparing SPM calculations on September 12, 2011, between (a) SPM calculations based on MODIS RRS data from Doxaran <i>et al.</i> (2012) and (b) SPM calculations based on Landsat TM SR</u> | <u>23</u> |
| <u>Figure 10: Comparing SPM calculations on August 21, 2009, between (a) SPM calculations based on MODIS RRS data from Doxaran <i>et al.</i> (2012). (b) SPM calculations based on Landsat TM SR</u>      | <u>24</u> |
| <u>Figure 11: Spectral data from the red band from the Landsat TM scene taken on September 12, 2011</u>   | <u>25</u> |
| <u>Figure 12: Mean surface reflectance in the red band, that was used as proxy for turbidity, for (a) changing wind conditions, (b) stable NW wind conditions and (c) stable E wind conditions</u>        | <u>28</u> |
| <u>Figure 13: Naming and positions of the zones that were used to extract values from for the box and whisker plots</u>   | <u>30</u> |
| <u>Figure 14: Box and whisker plot showing the surface reflectance values in the extracted zones displayed in Figure 13 for stable E wind conditions</u>  | <u>31</u> |
| <u>Figure 15: Box and whisker plot showing the surface reflectance values in the extracted zones displayed in Figure 13 for stable NW wind conditions</u>   | <u>32</u> |

|  |    |
|--|----|
| <u>Figure 16: Mean surface reflectance from Workboat Passage in the red band, that was used as proxy for turbidity, for (a) changing wind conditions, (b) stable NW wind conditions and (c) stable E wind conditions</u>   | 33 |
| <u>Figure 17: Mean at-sensor (uncorrected) temperature from thermal infrared channels, for (a) changing wind conditions, (b) stable NW wind conditions and (c) stable E wind conditions</u>                                | 35 |
| <u>Figure 18: Mean at sensor (uncorrected) temperature from thermal infrared channels of Workboat Passage, for (a) changing wind conditions, (b) stable NW wind conditions and (c) stable E wind conditions</u>            | 36 |
| <u>Figure 19: Box and whisker plot showing the at-sensor (uncorrected) temperatures in the extracted zones displayed in Figure 13 for stable E wind conditions</u>   | 37 |
| <u>Figure 20: Box and whisker plot showing the at-sensor (uncorrected) temperatures in the extracted zones displayed in Figure 13 during stable NW wind conditions</u>   | 38 |
| <u>Figure 21: Bathymetry in the region of Herschel Island</u>  | 42 |
| <u>Figure 22: Bathymetry in the Workboat Passage (area between the Yukon main land and Herschel Island) with underlying turbidity calculations from this study during stable E wind conditions</u>                         | 43 |
| <u>Figure 23: Optical comparison of (a) the mean reflectance in the red band derived in this study and (b) the modelled turbidity derived by the model from Nechad <i>et al.</i> (2009) under stable E wind conditions</u> | 45 |
| <u>Figure 24: Turbidity profile along the coast of Herschel Island, extracted from the modelled turbidity from Nechad <i>et al.</i> (2009)</u>   | 46 |
| <u>Figure 25: Positioning of the profile line presented in Figure 24</u>   | 47 |
| <u>Figure 26: SPM model from MODIS aqua data calculated by Doxaran <i>et al.</i> (2012) at September 12, 2011</u>  | 48 |
| <u>Figure 27: Comparison of (a) the TSM model from Tang <i>et al.</i> (2013), and the SPM models from Nechad <i>et al.</i> (2010) using (b) NIR and (c) red band reflectances</u>  | 49 |
| <u>Figure 28: Example for the difficulties associated with using the USGS provided cf-mask</u>   | 51 |

## List of Tables

---

|   |           |
|---|-----------|
| <u>Table 1: Summary of the impact of climate change in the Arctic</u>   | <u>22</u> |
| <u>Table 2: Used Landsat scenes</u>   | <u>27</u> |
| <u>Table 3: Comparing modelled output values from different models and this study in the nearshore zone of Herschel Island (east of Collinson Head) and the Mackenzie Delta</u> | <u>50</u> |

## List of Annotations

---

|         |   |
|---------|---|
| AVHRR   | Advanced Very High Resolution Radiometer      |
| AOI     | Area of Interest                              |
| CZCS    | Coastal Zone Color Scanner                    |
| DEM     | Digital Elevation Model                       |
| ETM+    | Enhanced Thematic Mapper +                    |
| FTU     | Formazine Turbidity Unit                      |
| MODIS   | Moderate-Resolution Imaging Spectroradiometer |
| MSS     | Multispectral Scanner                         |
| NIR     | Near Infrared                                 |
| OLI     | Operational Land Imager                       |
| RRS     | Remote Sensing Reflectance                    |
| SeaWiFS | Sea-viewing Wide Field-of-view Sensor         |
| SLC     | Scan line Corrector                           |
| SOC     | Soil Organic Carbon                           |
| SPM     | Suspended Particulate Matter                  |
| SR      | Surface Reflectance                           |
| SST     | Sea Surface Temperature                       |
| STD     | Standard Deviation                            |
| SWIR    | Shortwave Infrared                            |
| TIRS    | Thermal Infrared Scanner                      |
| TIRS    | Thermal Infrared                              |
| TM      | Thematic Mapper                               |
| TOA     | Top-of-Atmosphere                             |
| TSM     | Total Suspended Matter                        |
| USGS    | United States Geological Survey               |
| YCP     | Yukon Coastal Plain                           |



## Zusammenfassung

---

Die Arktis ist, bedingt durch den globalen Klimawandel, tiefgreifenden Veränderungen ausgesetzt. Die Erdoberflächentemperatur und Abflüsse steigen an, während Permafrost-Küsten stärker erodieren und der darin gespeicherte Kohlenstoff freigesetzt wird. Viele dieser Faktoren erhöhen die Menge an SPM (suspended particulate matter) auf den Arktischen Schelfen und bislang ist wenig darüber bekannt, wie die ökologischen und geologischen Reaktionen der Schelfe ausfallen werden. Um das Verständnis der Entwicklung der Arktischen Schelfe unter Einfluss des Klimawandels zu vertiefen, wird in dieser Masterarbeit ein Kartierungsversuch von Sedimentverteilung und Meeresoberflächentemperatur (SST) in den Küsten- und Ufergewässern von Herschel Island auf dem Kanadischen Beaufort Schelf präsentiert.

30 Jahre Landsat Satelliten Bilddaten wurden unter wechselnden jahreszeitlichen Windbedingungen (Ost- und Nordwestwind) analysiert und interpretiert. Da keine *in – situ* Messungen zur Kalibrierung der spektralen Daten vorliegen, wurden für beide gesuchten Größen Proxys gewählt, um einen relativen Überblick über den Untersuchungsbereich zu erhalten: Surface Reflectance des roten Bandes (655 nm) für Trübung, das als Proxy für die Sedimentverteilung benutzt wurde, und unkorrigierte At-Sensor Temperaturen des Infrarotkanals (10,4–12,5  $\mu\text{m}$ ) für SST. Von allen Szenen mit vergleichbaren Windbedingungen wurde der Mittelwert berechnet, was in einer sehr guten Repräsentation über den gesamten Beobachtungszeitraum resultiert.

Während konstanten Ostwinden sind sowohl die Werte der Trübung als auch der SST im Mittel höher als während stabilen NW-Winden. Ein Grund dafür könnte der Einfluss des Mackenzie River Plumes sein, der während stetigen Ostwinden Sediment und Frischwasser über das Kanadische Beaufort Schelf verteilt. Die niedrigen Werte während stabiler NW-Winde deuten auf die deutlich geringen Sediment- und Frischwassereintrag der anderen Quellen des Schelfs hin. Die Trübheit zeigt einen starken Gradienten von der Küste hin zum ‚offenen Ozean‘, was darauf hindeutet, dass ein Großteil der gelösten Sedimentfracht im Meerwasser in den Küstengewässern abgelagert und transportiert wird. Die SST zeigt keinen so starken Gradienten, obwohl Tiefenwasseraufstieg an der NW-Küste von Herschel Island zu großen Temperaturunterschieden während stabiler Ostwinde führt.

Die Ergebnisse wurden mit anderen Modellen verglichen, um auch ohne *in-situ* Daten einen Eindruck über die zu erwartende Größenordnung der absoluten Werte zu erhalten. Die Modellierung der Trübheitswerte und SPM-Konzentration erfolgte nach Vorgabe von Nechad et al. (2009, 2010), aus der entsprechende Trübheitswerte von weniger als 30 FTU und SPM-Konzentrationen zwischen 10 – 30 g/m<sup>3</sup> resultieren. Diese Werte sind in sehr gutem Einklang mit den Modellergebnissen von Doxaran et al. (2012).

Die hauptsächlichen Einschränkungen des hier präsentierten Modells liegen in der geringen zeitlichen Auflösung der Landsat Satelliten (16 Tage) und der atmosphärischen Korrektur (Surface Reflectance), bedingt durch das geringe Signal-Rausch-Verhältnis der älteren Landsat Sensoren. Während neuere Sensoren wie Landsat 8 (OLI) oder Sentinel 2 letzteres Problem lösen können, ist die zeitliche Auflösung noch immer eine große Einschränkung von hochauflösender Ozean-Farb-Fernerkundung. Mit *in-situ* Messungen zur Kalibrierung der spektralen Daten wird erwartet, dass das hier präsentierte Modell konsistente Daten zur SPM Konzentration und SST auf dem gesamten Kanadischen Beaufort Schelf liefern kann.

## Abstract

---

The Arctic is subject to substantial changes due to the greenhouse gas induced climate change. Ground temperatures and river discharge are rising, (permafrost) coasts are eroded and the carbon stored in them is released. The aforementioned factors contribute suspended sediment to the Arctic shelves which represent an uncertainty regarding future ecological and geological reactions. In order to increase the understanding of the development of Arctic shelves due to the changes described, this Master's thesis presents a mapping approach of sediment dispersal and sea surface temperature (SST) in the coastal and nearshore zone of Herschel Island on the Canadian Beaufort Shelf.

In this regard, 30 years of Landsat satellite imagery were analyzed and interpreted under different seasonal wind conditions (E and NW wind). Due to the absence of *in-situ* measurements to calibrate the spectral data, proxys were chosen for both values to receive a relative overview of the study area: the surface reflectance of the red band (655 nm) for turbidity (which acts as proxy for sediment dispersal) and at-sensor (uncorrected) temperature from thermal infrared channels (10,4–12,5  $\mu\text{m}$ ) for SST. For scenes with similar wind conditions, the mean was calculated, resulting in a very good representation over the observation period.

During stable E wind conditions, the mean values of both turbidity and SST were higher than during NW wind conditions. This may result from the influence of the Mackenzie River Plume, distributing suspended sediment and fresh water over the Canadian Beaufort Shelf during stable E wind conditions. The low values during stable NW wind conditions indicate that the sediment and fresh water input from other sources than the Mackenzie River to the Canadian Beaufort Shelf are of minor importance compared to it. Turbidity shows large gradients from the nearshore to the offshore zone, indicating that large parts of the suspended sediment are deposited and transported in the nearshore zone. SST does not have such a strong gradient; however, upwelling causes large differences at the NE coast of Herschel Island during stable E wind conditions.

The resulted values have been compared to other modelling approaches to assess the magnitude of absolute values representing the reflectance values. Modelling turbidity and SPM after Nechad et al. (2009, 2010) results in values of 20 - 30 FTU and 10 – 30  $\text{g}/\text{m}^3$  along the coast, respectively. These values are in good agreement with SPM modelling from Doxaran et al. (2012).

Limitations of the presented modelling method are the low temporal resolution of Landsat satellites of 16 days and the atmospheric correction to surface reflection due to the low radiometric resolution of the older Landsat satellite sensors. While newer sensors such as Landsat 8 (OLI) and Sentinel 2 can overcome the last limitation, the temporal resolution is still a limitation for high resolution ocean color remote sensing. With the calibration of the spectral data with *in-situ* measurements, this model is expected to derive consistent SPM concentration and SST data for the whole Canadian Beaufort Shelf.

# 1. Introduction

---

The Arctic is an area of rising scientific interest, because the effects caused by global climate change are expected to be stronger in the Arctic than anywhere else on Earth (Holland and Bitz, 2003; IPCC, 2013). Even though climate changes are very common in the history of our planet, the human - induced greenhouse warming, which started in the 19<sup>th</sup> century, seems to be unique in its pace. While past climate changes were often caused by tectonic or astronomic forcing, humans influenced the Earth's climate significantly by producing large amounts of greenhouse gases since the onset of the industrial revolution (IPCC, 2013). This ongoing process cannot be stopped abruptly, even if greenhouse gas emissions are suddenly stopped. The risk of irreversible changes increases with advancing warming.

The Arctic is one of the regions on Earth that is most affected by this warming (Barker, 2007). The mean annual surface temperature is projected to rise by up to ~ 10°C during the 21 century (IPCC, 2013). This would have enormous consequences on terrestrial and marine ecosystems, as well as on the humans living in the high latitudes (Klein et al., 2016; Hansen et al., 2010; Günther et al., 2013; Lantuit et al., 2012; Walsh et al., 2017; Romanovsky et al., 2010; Figure 1). A detailed description of the evidence, the driving forces and the implications of global climate change in the Arctic is given in section 2.4.

Thawing and erosion of permafrost are associated with climate warming and will result in a large release of  $CO_2$  (Romanovsky et al., 2010; Vonk et al., 2012). The Arctic area contains more than 50 % of the globally soil organic carbon (SOC, Dixon et al., 1994; Dittmar and Kattner, 2003). Most of it is stored in permafrost (terrestrial and subsea), which is sensitive to climate warming (Hugelius et al., 2014). The SOC is bound to soil particles and can be transferred into  $CO_2$  in the soils by microorganisms when permafrost thaws. It can also be directly released into the nearshore zone when the sediment is eroded at the coast.

Sedimentary input (from coastal erosion and from rivers) to the Arctic nearshore zone and shelf areas rose significantly in the past decades (Peterson, 2006; McClelland et al., 2006). The mean annual discharge of the Eurasian rivers entering the Arctic Ocean increased by 10 -14 % in the latter half of the 20<sup>th</sup> century. The annual discharge of the

Mackenzie River rose by 22 % together with an increase of SPM concentration of 46 % from 2003 to 2013 (Yang et al., 2015; Doxaran et al., 2015). Syvitski (2002) predicted an increase of 10 % in sediment load for every 20 % increase in discharge for Arctic rivers by climate modelling; in case of the Mackenzie River this value strongly underestimates reality.

Arctic coasts are also actively degrading leading to an enhanced input of sediment (Lantuit et al., 2012). The mean annual erosion rate of arctic coasts is 0.5 m/a. Higher values up to 10 m/a occur near deltas of big rivers entering the Arctic Ocean (Mackenzie, Lena, Yenisei, Ob, Kolyma).

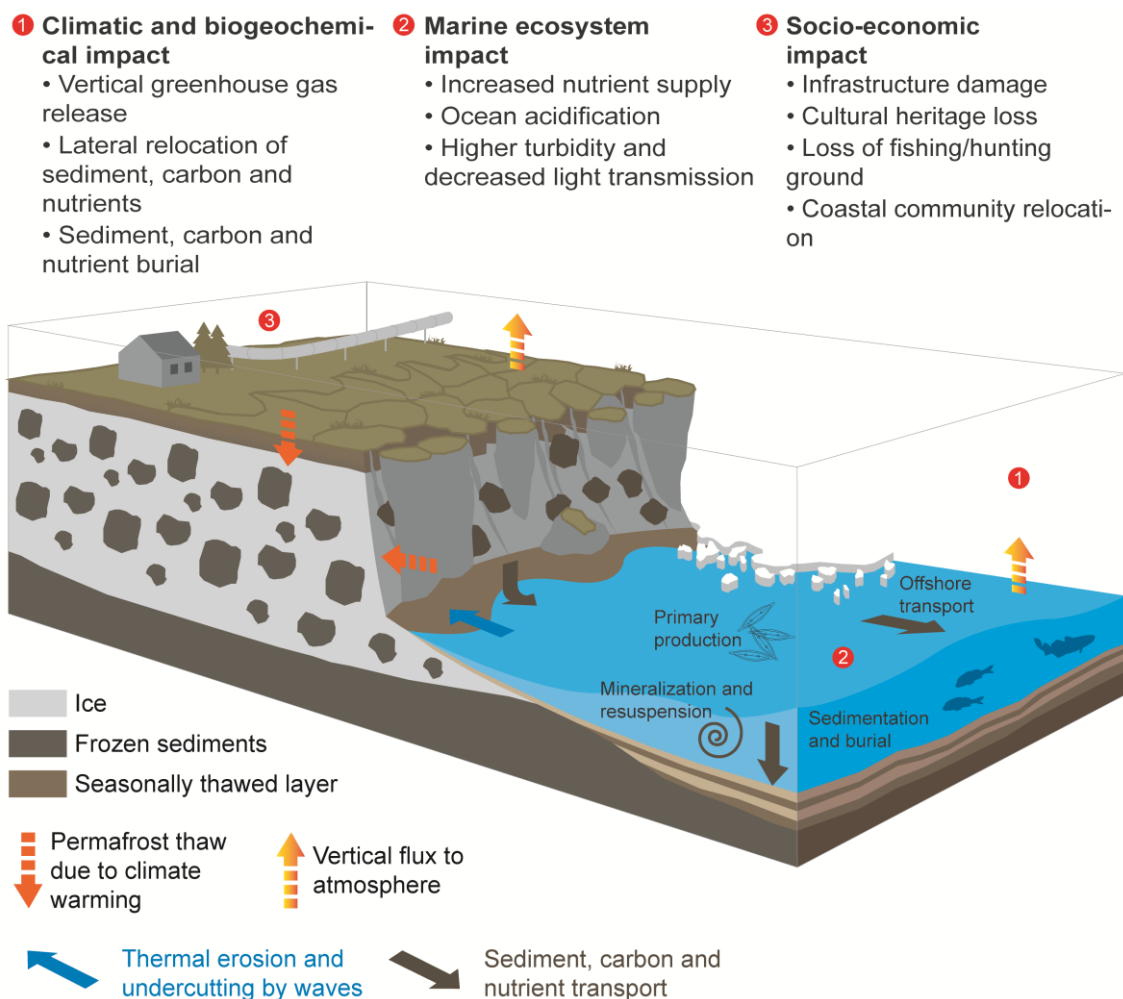


Figure 1: "Impact of thaw and erosion of Arctic permafrost coasts: (1) climatic and biogeochemical consequences [...] due to vertical and lateral carbon mobilization onshore, in the nearshore and offshore. (2) Marine ecosystem perturbations [...] due to release of nutrients, pollutants, carbon and sediments to the nearshore zone [...]. (3) Socio-economic impacts in the coastal zone [...]: infrastructure damage, loss of cultural heritage, fishing and hunting grounds, and the threat of coastal community relocation" (Fritz et al., 2017).

Stable (or even aggrading) coasts are present in the American Chukchi Sea, the Canadian and Greenland Archipelago, Svalbard, the Barents Sea and the Kara Sea.

Climate models project an increase in river discharge for the whole Arctic by up to 50 % and regionally even more in the end of the 21st century compared to the end of the 20th century (Van Vliet et al., 2013, Figure 2). These numbers and projections are available because rivers in the Arctic have been well studied during the last decades. However, pan – Arctic long-term datasets of changing coastal erosion do not exist (Lantuit et al., 2012). Therefore, climate models are not yet able to project coastal erosion rates in the future. However, an increase is likely, since increasing erosion rates have already been observed for short stretches of coast (Jones et al., 2009; Günther et al., 2013; Radosavljevic et al., 2015).

Arctic shelves are very important for regional ecosystems and economy. They are the main area of primary production (Arrigo et al., 2008), which is highly dependent on light penetration into water and thus sensitive to changing discharge regimes of the entering rivers (Carmack and Wassmann, 2006). The amount of fresh water input to Arctic shelves is necessary for several species of amphidromous fishes that are essential food sources for native communities (Carmack and Wassmann, 2006; Dunton et al., 2006). Coastal areas in the Arctic are of high regional economic interest and very vulnerable to climate warming due to industry, housing (Raynolds et al., 2014) and cultural heritage (Radosavljevic et al., 2015). These components are therefore highly susceptible to an increase and/or a decrease in the input of sediment and organic matter to the nearshore zone.

Remote sensing provides a large amount of data for investigations of remote areas. Data can be acquired more easily over longer times without the need of personal presence at the sampling location. Yet, most sensors are limited either in spatial or temporal resolution, meaning high temporal coverage causes a loss of spatial resolution and *vice versa* (Hilker et al., 2009). In this study, the higher spatial resolution was identified to be more important than temporal coverage to investigate small scale hydrodynamic features.

It is unknown, whether sediment mobilized by coastal erosion in the Arctic stays in nearshore areas or gets transported offshore. Additionally, the contribution of large rivers (which are experiencing rising discharge conditions) to these nearshore areas is

often poorly resolved. So far, only large-scale studies on these topics have been performed (Doxaran et al., 2012; Heim et al., 2014), which are not adequate for the investigations of smaller nearshore areas, which are often very local by nature and are not resolved by the large pixels used in these studies. In order to fill this gap, I present the first high resolution remote sensing study on sediment transport in Arctic nearshore areas.

Identifying the driving forces and understanding the processes of climate change is one main objective of Arctic research. At the Alfred Wegener Institute in Potsdam, the southern Beaufort Sea, including the Yukon Coastal Plain and Herschel Island, are extensively studied by the Helmholtz Young Investigators Group COPER (“Coastal permafrost erosion, organic carbon and nutrient release to the Arctic nearshore zone”). The research of COPER focusses on organic material in permafrost sediments, coastal erosion in the Arctic and transport pathways of organic material in the coastal and nearshore zone.

In this context, this Master’s thesis will operate as a test to provide a first qualitative overview of sediment transport pathways in the coastal and nearshore zone of Herschel Island. Specifically, this thesis has the objective to identify SPM and SST dispersal patterns depending on wind forcing. Therefore, 30 years of Landsat satellite image data was analyzed under changing seasonal meteorological conditions with a focus on SPM and SST. This study could be the first step in understanding transport regimes on Arctic shelves under rising discharge conditions.

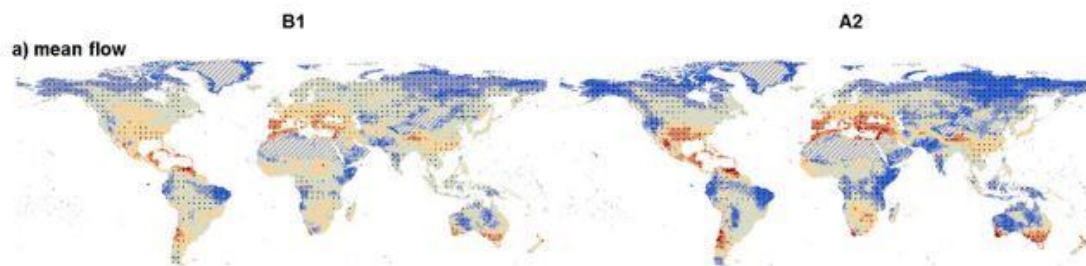


Figure 2: "Global projected change in mean flow for 2071 - 2100 relative to 1971 - 2000 averaged for the (...) GCMs for both the SRES A2 and B1 emissions scenario." For every used climate scenario, the mean flow in the Arctic will rise significantly (Van Vliet et al., 2013).

**Flow change (%)** ■ < -50 ■ -50 to -25 ■ -25 to 0 ■ 0 to 25 ■ 25 to 50 ■ > 50  masked



## 2. Scientific Background

---

### 2.1 Suspended Sediment Transport in Coastal Waters

---

Water transports sediment in coastal waters as bedload or in suspension (Hjulström, 1939). The main factor differentiating these two modes of transport is the flow velocity of water. The driving forces of flow velocity vary in different settings. While discharge is the main driving force of flow velocity in rivers, the tidal amplitude, wind stress and bathymetry are responsible for the flow velocity in coastal waters, except for estuarine regions, where all factors play an important role (Figure 3). The position of suspended particles in the water column is determined by the turbulence of water, i.e. the rate of internal lateral mixing of water. At increasing turbulence, the water has more energy available to transport suspended particles higher above the riverbed or seafloor.

Sediment dispersal in coastal surface waters is linked to sediment transport. The flow velocity of water is mainly driven by water depth, small scale hydrographic features and climate, mainly wind patterns and rainfall due to varying discharge of delivering rivers (Doerffer et al., 1989). These parameters act upon sediment dispersal at different scales in space and time. At shallow water depths, less energy is needed to carry suspended sediment to the water surface. Increasing wind speed causes higher shear stress on the water surface, so that suspended particles can be transported over large distances, when water depth remains low (i.e. at shelves). Higher river discharges thus have a higher erosional potential, resulting in higher concentrations of suspended particles, combined with higher flow velocities, lead to increased turbulence. Small hydrographic features like underwater sills or sandbanks have the potential to modify larger scale processes regionally due to current changes. This may affect ecological processes like phytoplankton growth, sedimentation rates and resuspension (Simpson and Brown, 1987; Doerffer et al., 1989).

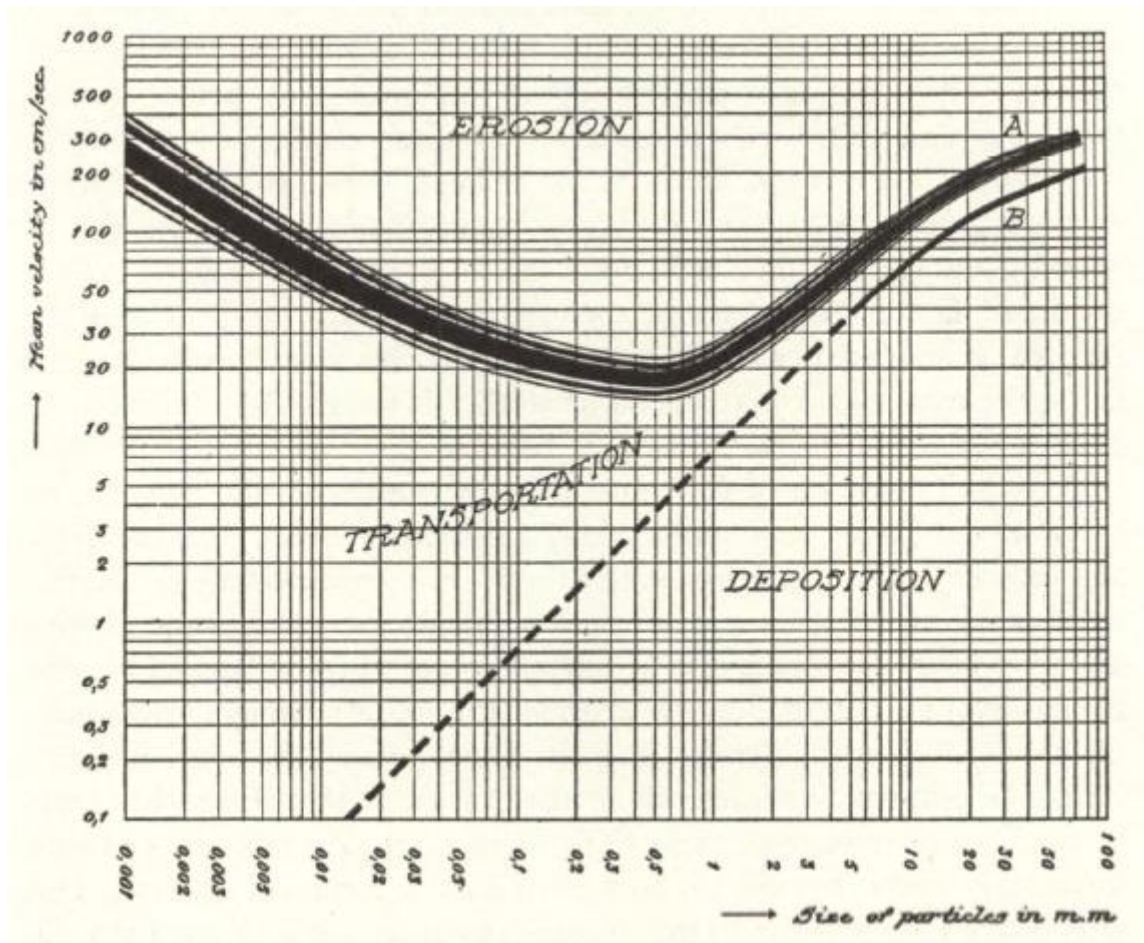


Figure 3: Hjulström diagram. Approximations for erosion and deposition of uniform material in water. Transport is mostly limited to particles smaller than 1 mm in diameter. Note that there are several other factors influencing the transport of sediment in water, such as surface roughness of the particle, its weight and cohesion, but all of them are somehow correlated to the particle size (Roughness and weight: positive, cohesion: negative). Hjulström 1939.

## 2.2 Turbidity, Suspended Particulate Matter (SPM) and Total Suspended Matter (TSM)

Sediment dispersal refers to the transport of SPM in the water. Turbidity refers to the optical measurement of suspended particles within the water column. Turbidity and SPM values often correlate with each other, because increasing turbidity is caused by higher SPM concentration due to resuspension (Bustamante et al., 2009; Nechad et al., 2009). Thus, it should be possible to derive SPM values from turbidity measurements (and the other way around), when *in-situ* measurements are available (Dogliotti et al., 2015). Global algorithms to calculate turbidity have been proposed (Nechad et al., 2009), but validation datasets are too limited to apply transfer functions between turbidity and SPM at the global level, even though several authors successfully applied transfer function at the local level (Dogliotti et al., 2015). Global TSM models still have

higher errors than turbidity models (30% compared to 6 %, Nechad et al., 2010; Dogliotti et al., 2015), hence are not that applicable, especially for low concentrations.

TSM refers to the transport of SPM in water and ecological processes (Ruddick et al., 2004). The expressions TSM and SPM are often used as synonyms, but they differ: TSM contains SPM plus organic components like algae. Even though SPM is more useful for sedimentation models, TSM is often derived directly from satellite images, because the differentiation of SPM and organic material based multispectral data is complicated (Dogliotti et al., 2015).

### 2.3 Sedimentary transport at the Canadian Beaufort Shelf

---

The goal of this thesis is to investigate sediment dispersal in coastal areas of the Canadian Beaufort Shelf. The Sediment of the Canadian Beaufort Shelf is nearly exclusively delivered by the Mackenzie River (Hill et al., 1991, Figure 4). Even though coastal erosion has nearly doubled compared to the 80's (Jones et al., 2009; Radosavljevic et al., 2015), its input is still very low compared to the Mackenzie River.

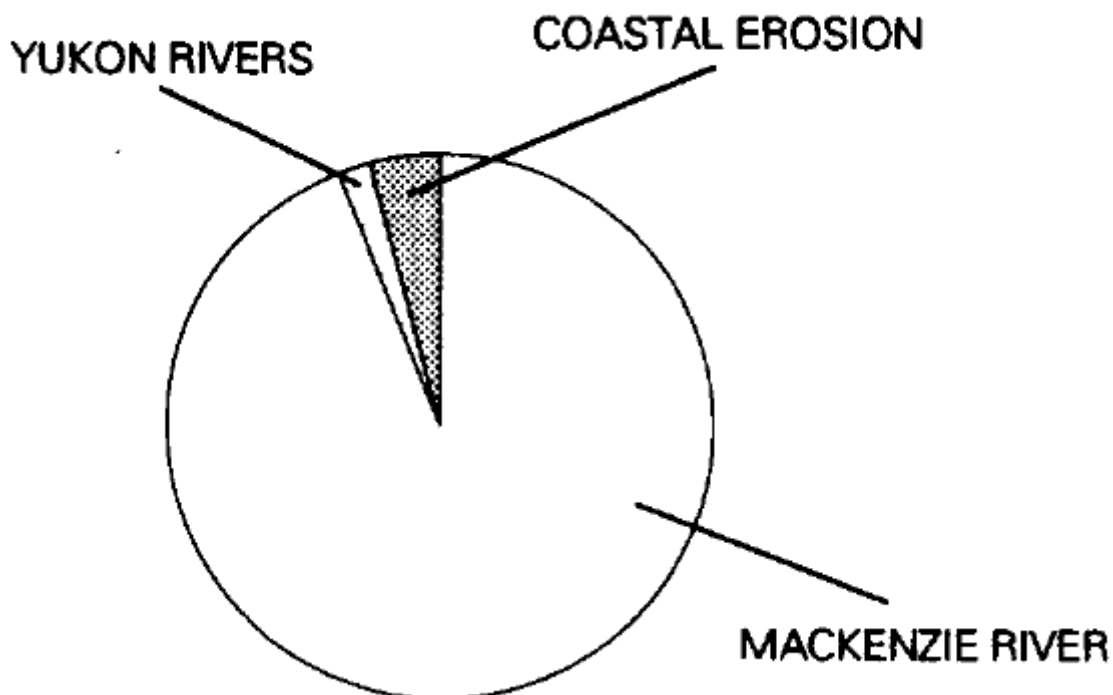


Figure 4: "Summary of the principal sediment sources to the Canadian Beaufort Shelf sediment" (Hill et al., 1991).

Reports about the mean annual discharge of the Mackenzie River vary substantially. Holmes et al. (2002) report a mean annual discharge of the Mackenzie River of 281 km<sup>3</sup>/a, while O'Brien et al. (2006) report 333 km<sup>3</sup>/a and Doxaran et al. (2012) 330 km<sup>3</sup> only during the ice-free season (3-4 months).

According to Holmes et al. (2002), estimations on mean annual sediment flux for the Mackenzie River vary from 15 Mt/a to 230 Mt/a (Holmes et al., 2002 and citations therein). In the early years of Mackenzie River sediment flux observations (1960-80's), only small observation periods were used (< 4 years). Since the database became more extensive during the 1990's, several authors estimated a mean annual sediment flux of 125 Mt/a.

This wide span of mean annual sediment flux rates may result from the structure of the Mackenzie Delta and the placement of gauging stations. The most important gauging station, Arctic Red River (Tsiigehtchic), lies slightly upstream of the meeting point of the Mackenzie and the Arctic Red River, so discharge values at the river mouth are only derived from a gauging station located ~ 400 km upstream of it. Additionally, the Peel River discharges into the Mackenzie Delta too, but is technically not a tributary of the Mackenzie River. This results in widely different results in the literature, even though the discharge of the Mackenzie River is one of the best documented for the big Arctic Rivers (Holmes et al., 2002).

The sedimentary transport on the Canadian Beaufort Shelf is strongly influenced by the presence of an ice cover for approximately 7-9 months per year (Hill et al., 1991). During winter, the fresh water accumulates under the ice, forming essentially a lake (unofficially Lake Herlinveaux, Macdonald et al., 1995; Doxaran et al., 2012), so sediment transport is probably not completely interrupted. Studies on sediment transport under the ice cover are rare, but it is likely, that it is limited because of i) the Mackenzie River discharge regime and ii) the elimination of wind stress (Hill et al., 1991).

During summer, sedimentary transport is controlled by the Mackenzie River Plume dispersal, bottom currents and waves (Hill et al., 1991). The extent of the Mackenzie Plume, an up to 5 m thick mixed layer of fresh and shelf water, is controlled by the wind conditions and the Mackenzie River discharge. Sediment plumes of other rivers along the Yukon coast are much smaller. Their extent is often limited by barrier islands in front of their deltas (i.e. Malcom River, Firth River).

SPM concentrations are high in shallow waters (100 mg/L, up to 5 m depth) and decrease rapidly to less than 20 mg/L beyond the 10 m isobaths (Hill et al., 1991). In easterly wind conditions, the sediment plume may cover large parts of the Canadian Beaufort Shelf, while westerly winds keep the sediment near the delta. Most of the sediment settles down along the shelf; only small parts leave it (Doxaran et al., 2012).

During the open water season, bottom currents are wind driven, with decreasing dependency at increasing water depths (Hill et al., 1991). Bathymetry is influencing the flow, which is strongest, if wind blows parallel to the isobaths.

Wave energy in the Beaufort Sea is controlled by two factors: the available fetch and the wind direction (Hill et al., 1991). Even though fetch length may exceed 1000 km in late summer, wave heights are predominantly below 4 m (Thomson and Rogers, 2014; Hill et al., 1991). Most wave energy accumulates in wave heights below 2 m. Despite the bimodal wind pattern, the dominant moving direction is from west to east, while storm waves usually move from northwest to southeast.

During NW wind conditions, the waves have more potential to transport sediment due to stronger winds (storms) and longer fetch. Thus, the wave induced sediment transport on the Canadian Beaufort Shelf depends on the number of storms per year, which varies between 0 and 9 (Couture, 2010). According to the morphology of the coast and its islands off the coast, areas with SE coastal exposure are in a wave shadow and less affected by wave induced sediment transport (i.e. Thetis Bay, Figure 6, Solomon, 2005; Forbes, 1997).

## 2.4 Climate Change and its Consequences in the Arctic

---

Even though the greenhouse gas induced climate change is mainly caused by communities living in the temperate regions of the Earth, its consequences are most amplified in the polar and tropical regions (Holland and Bitz, 2003). This leads to drastic changes in terms of sea ice extent, permafrost temperature, and ecosystem function.

Arctic coastal ecosystems will mainly change due to permafrost thaw (Tanski et al., 2017), sea ice extent changes (Walsh et al., 2017) and rising sea levels (Radosavljevic et al., 2015; Comiso and Hall, 2014). This will likely have substantial impacts on Northern

Communities (Serreze et al., 2007), Arctic fauna (Stirling and Parkinson, 2006) and the worldwide climate (Manabe, S. and Stouffer, 1980, Table 1).

Reduced sea ice extent leads to bigger fetch lengths and higher wave energy with the potential to increase coastal erosion (Serreze et al., 2007; Fritz et al., 2017). Together with higher SST and air temperatures (Manabe, S. and Stouffer, 1980; Hansen et al., 2010), melting coastal permafrost and thermokarst evolution will degrade human infrastructure (Raynolds et al., 2014) and cultural heritage throughout the Arctic (Radosavljevic et al., 2015; Fritz et al., 2017). This will lead to substantial costs in the future; Raynolds et al. (2014) estimated 6 billion \$ from 2015-2030 only for Alaska. Considering the small Arctic Ocean coastline of Alaska (3.3 % of the whole Arctic Ocean coastline) and the predominantly low coastal erosion rates (< 1 m/yr, Lantuit et al., 2012), pan-Arctic costs could easily exceed 100 billion \$ until 2030.

Marine ecosystems will also be affected by changes in the coastal zone. The disappearance of sea ice and the rise in sea surface temperatures can lead to drastic impacts (Walsh et al., 2017). These include increasing primary production (Arrigo et al., 2008), increased fresh water input from rivers (Yang et al., 2015; Doxaran et al., 2015) and borealization of marine species (Fossheim et al., 2015). Several of these amplify each other: increased river discharge transports more nutrients to the shelves, where primary production increases, producing food sources for bigger marine species. On the other hand, increasing primary production leads to higher turbidity and thus less light penetration in the water (Arrigo et al., 2008).

## 2.5 Knowledge gaps

---

Changes in river discharges and their impacts on Arctic coastal ecosystems are subject of several studies. These studies show, that mean daily flow rose in the past 30 years (Yang et al., 2015) and is projected to rise by up to 50 % until the end of the century (Van Vliet et al., 2013). Syvitski (2002) and Gordeev (2006) project an increase of 10 % of sediment load per 20 % increase of discharge and an increase of 30 % of sediment load per 2 °C warming in the drainage basin. Considering a projected warming in the Arctic of up to ~10°C until 2100 (IPCC, 2013), sediment load of Arctic rivers would rise up to 275 %.

Doxaran et al. (2015) measured discharge and sediment load of the Mackenzie River from 2003-2014. Their results show an increase of river discharge of 25 % together with an increase of 50 % of particulate export to the Beaufort Sea. SPM concentration in the river plume rose by 46 % in the same time. These values indicate that, in case of the Mackenzie River, the modelled values strongly underestimate reality.

All these studies use either *in-situ* measurements, low spatial resolution remote sensing or modelling approaches (or a combination of them). Studies using high spatial resolution remote sensing are rare, because those sensors typically have a lower temporal resolution than low spatial resolution sensors. On the other hand, high spatial resolution remote sensing allows the investigation of coastal and nearshore areas, where dynamic processes act up on small spatial scales.

Resuspension of sediments, SPM concentrations in coastal waters and coastal erosion have large potential impacts throughout the Arctic (Doxaran et al., 2015; Fritz et al., 2017). Yet, only small spatial scale studies on these impacts have been made (Vonk et al., 2012). To investigate those processes in a whole coastal environment, high spatial resolution remote sensing is needed.

In this study, we will use the extensive and powerful archive of Landsat satellite imagery and its high spatial resolution over more than 30 years to resolve nearshore sediment dispersal processes and SST in a test site located in the southern Beaufort Sea.

## 2.6 Landsat satellite remote sensing

---

The first Landsat satellite was started in July 1972, carrying the Multispectral Scanner (MSS), collecting data with a spatial resolution of 79 meters, which were resampled to 60 meters (US Geological Survey, 2016). The spectral resolution was limited to 4 bands, ranging from visible (green) to NIR wavelengths. Landsat 2 and 3, started in January 1975 and March 1978, respectively, carried the same sensor as Landsat 1. All 3 satellites orbited at an altitude of 920 km. The resulting temporal resolution (repeat coverage) was 18 days.

The Thematic Mapper (TM) was onboard of Landsat 4 and 5, started in July 1982 and March 1984, respectively (US Geological Survey, 2016). With TM, two additional bands in the SWIR part of the spectrum became available, as well as a thermal IR band. The spatial resolution was increased to 30 m, while the TIR band collected data with a

spatial resolution of 120 m, that were resampled to 30 m. Landsat 4 and 5 orbited the Earth at an altitude of 705 km. This results in a temporal resolution of 16 days. Both satellites had a temporal offset of 8 days, resulting in a temporal resolution of 8 days of any Landsat scene on the globe, when both satellites were working (March 1984 – December 1993).

| Theme                      | Location               | Time Frame | Evidence  | Climate Drivers   | Implications  | Source, Citation   |
|----------------------------|------------------------|------------|---|---|---|--|
| Weather                    | Alaska                 | 1945-2008  | $\delta^{18}\text{O}$ record                          | changed synoptic patterns                                     | expansion of thermokarst                                  | Klein <i>et al.</i> 2016                                   |
|                            | Arctic                 | 1970-2010  | Goddard Institute for Space Studies (GISS) analysis   |   |   | Hansen <i>et al.</i> 2010                                  |
| Permafrost and Thermokarst | Herschel Island        | 2013, 2014 | Carbos loss at RTS degradation                        | Global warming, changes in snow                               | Mobilization of Carbon                                    | Tanski <i>et al.</i> 2017                                  |
| Coastal Erosion            | Herschel Island        | 1952-2011  | Rising coastal erosion since 2000                     | Changing strom regime, increased summer SST, rising sea-level | Loss of cultural heritage and infrstructure               | Radosavljevic <i>et al.</i> 2015                           |
|                            | Alaska                 | 1955-2007  | Increased coastal erosion since 1955                  |   |   | Jones <i>et al.</i> 2009                                   |
| Rivers                     | Mackenzie              | 1975-2011  | Higher seasonal variability, higher mean annual flow  | Increasing precipitation                                      | Higher flood risk, higher erosion rates                   | Yang <i>et al.</i> 2015                                    |
|                            |                        | 2003-2013  |   |   |   | Doxaran <i>et al.</i> 2015                                 |
| Glaciers                   | Worldwide              | 1971-2009  | Decreasing coverage area                              | Global warming  | Sea level rise, increased Albedo                          | Cosimo <i>et al.</i> 2014, IPCC 2013                       |
| Vegetation                 | Eurasia, North America | 1970-2000  | Changed vegetation types                              | Global warming, changing precipitation                        | Reduced boreal forest                                     | Buermann <i>et al.</i> 2014                                |
| Fauna                      | Barents Sea            | 2004-2012  | Borealization of fish                                 | Rising sea surface temperatures                               | Species turnover  | Fossmann <i>et al.</i> 2015                                |
|                            | Arctic                 | 2006, 2007 | Increased primary production                          | Decreased sea ice extend                                      | Changes in marine ecosystems, changed marine biochemistry | Arrigo <i>et al.</i> 2008                                  |
| Humans                     | Alaska                 | 1949-2011  | Infrastructure degradation, loss of cultural heritage | Global warming  | Loss of money   | Raynolds <i>et al.</i> 2014                                |
|                            | YCP, Herschel Island   | 1952-2011  |   |   |   | Radosavljevic <i>et al.</i> 2015, Fritz <i>et al.</i> 2017 |

Table 1: Summary of the impacts of climate change on the biophysical and socio-economic environment, including the location of report, the time frame of report, evidence, climate drivers, implications and sources /citations.

Landsat 6 carried the Enhanced Thematic Mapper (ETM), but it failed to reach its orbit in October 1993 (US Geological Survey, 2016). Landsat 7, started in April 1999, carries the Enhanced Thematic Mapper Plus (ETM+) that has, additionally to TM, a panchromatic band with a spatial resolution of 15 meters onboard. The spatial resolution of the TIR band was increased to 60 meters. Unusual artifacts began to appear on May



31, 2003, which are caused by the failure of the Scan Line Corrector (SLC), resulting in a loss of ~22 % of the initial image data (Storey et al., 2005). All efforts in fixing the SLC-problem were unsuccessful; however, Landsat 7 is still in its orbit and acquires data worldwide.

Landsat 8, started in February 2013, is the most recent Landsat satellite in space (US Geological Survey, 2016). It carries the push-broom Operational Land Imager (OLI) and the Thermal Infrared Sensor (TIRS). OLI contains similar spectral bands as ETM+, with additional ones in the deep blue part of the spectrum and a Cirrus band, located between the NIR and the SWIR parts of the spectrum. TIRS contains two TIR bands that were designed to allow split-window surface temperature retrieval algorithms. Landsat 7 and 8 use the same orbits as Landsat 4 and 5. Landsat 9 is planned to be launched in 2020.

Landsat has been used to quantify suspended particles for many decades (MacFarlane and Robinson, 1984; Doerffer et al., 1989; Ritchie et al., 1990; Vanhellemont and Ruddick, 2014), even though the Landsat sensors were initially built for land surface applications (8 bit radiometric resolution for ETM+ and earlier sensors). The high spatial resolution (30 m from Landsat TM on) was deemed critical by many investigators to investigate local coastal environments or lakes, because sensors designed for sea surface applications commonly have much coarser spatial resolution (Coastal Zone Color Scanner (CZCS, 1978): 800m; Sea-Viewing Wide Field-of-View Sensor (SeaWiFS, 1997): 1.1 – 4.5 km; Moderate-resolution imaging spectroradiometer (MODIS, 1999): 250 – 1000 m). The main difficulties associated with the use of Landsat satellite image data at the sea surfaces arise from the small signal-to-noise ratio associated with the radiometric resolution (Doerffer et al., 1989), as well as the low temporal resolution (repeat coverage) of 16 days (MacFarlane and Robinson, 1984).

The use of Landsat to retrieve suspended sediment information has been associated with many challenges. While MacFarlane and Robinson (1984) received satisfactory results by correlating Landsat MSS data to suspended sediment concentrations, Doerffer et al. (1989) report about the limitations of Landsat TM, concerning sensitivity, radiometric resolution and spectral bandwidth. According to their results, Landsat TM could only be used with an averaging over 5x5 pixel, resulting in a resolution of 150 m, which is still a much higher spatial resolution than the sensors commonly used for these applications,

but not as high as expected. In contrast, Ritchie et al. (1990) found that the correlations of Landsat MSS and TM with suspended sediment concentrations do not differ significantly from reality. The usage of Landsat MSS and TM to extract suspended sediment concentrations remain a contentious issue until today.

Landsat 8 greatly improved on former Landsat platform for SPM retrieval applications. Vanhellemont and Ruddick (2014) showed the enormous advantages of the 12 bit radiance digitalizing system and longer integration times of the scanner for marine applications (resulting in higher signal-to-noise ratio, Figure 5), even though the spectral bands have not changed significantly. Together with the high spatial resolution, Landsat 8 is a very powerful all-rounder for land and sea surface remote sensing. However, the temporal resolution is still as low as before.

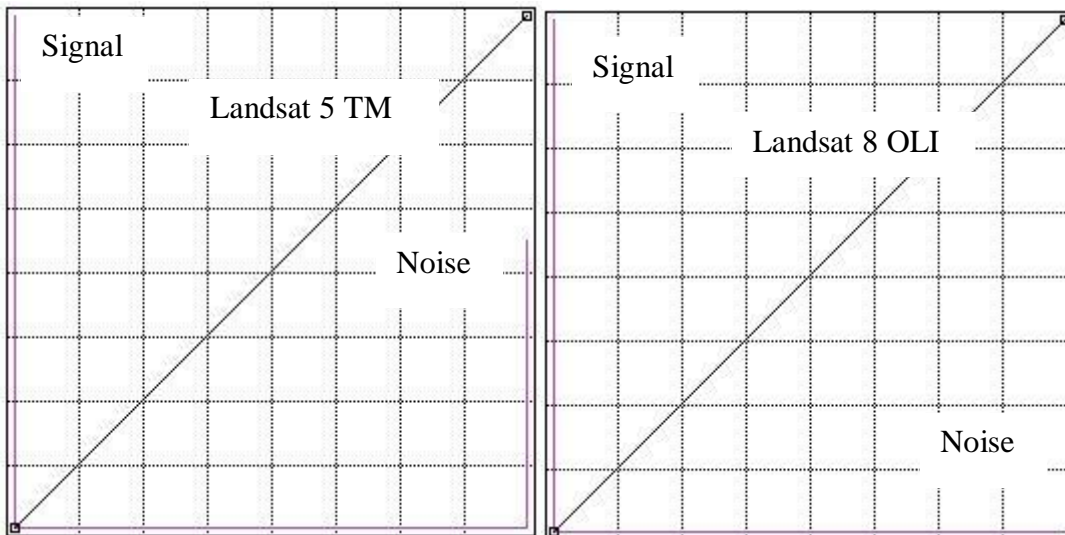


Figure 5: Compared Signal – to - Noise Ratio over Water of Landsat TM (left) and Landsat OLI (right). The longer integration time of the push – broom – scanner and the increased radiometric resolution increases the signal – to - noise ratio of Landsat OLI significantly compared to Landsat TM.

For coastal applications, Landsat provides features that are not offered by other satellites. The most important one may be the extensive archive of comparable data that is very useful to detect multi-year surface changes. Its high spatial resolution is also an asset to resolve small scale current features in the nearshore zone. However, as this sensor was originally designed for land surface applications, the retrieval of suspended sediment concentrations is still a challenging task.

### 3. Regional Setting

---

The Canadian Beaufort Shelf covers less than 2 % of the Arctic coast shelf area (~64 000 km<sup>2</sup>) and is narrow (100 km) compared to the Eurasian shelves (Stein and MacDonald, 2014; O'Brien et al., 2006). It extends from the Alaskan peninsula to the Canadian archipelago (Hill et al., 1991). The shelf has a gentle relief up to approximately 80 m water depth, where the shelf break is located. Notable exceptions are the Mackenzie Trough (often called Mackenzie Canyon), an up to 300 m deep glacial valley located north east of Herschel Island, and several smaller valleys with low relief. Throughout the Holocene, the seafloor has been covered with up to 30 m of sediment, predominantly clay-sized with some silt (Pelletier, 1975).

The Mackenzie River is the main fresh water and sediment source of the Canadian Beaufort Shelf (Doxaran et al., 2012; O'Brien et al., 2006; Holmes et al., 2002). It drains an area of approximately 1 805 000 km<sup>2</sup>. The average discharge at Arctic Red River (Tsiigehtchic) gauging station is 9 910 m<sup>3</sup>/s. Its ice-free season starts typically in mid-May, when warm fresh water arrives at the delta, providing enough heat to break up the ice 1-2 weeks prior to comparable coasts without significant river inflows (Mulligan et al., 2010). However, it is not unusual to find sea ice at the Canadian Beaufort Shelf until mid-July (Doxaran et al., 2012). The peak discharge is typically in early June (up to 25000 m<sup>3</sup>/s), while discharge in winter is as low as 4000 m<sup>3</sup>/s (December-May).

The Yukon Coastal Plain (YCP) is the above sea level lying extension of the Canadian Beaufort Shelf. It extends from the Mackenzie Delta in the east to the Canada - Alaska border in the northwest, where it becomes the Arctic Coastal Plain of Alaska (Fritz et al., 2012). Large parts of the YCP form an erosional surface cutting into Tertiary sandstones and shale, which are covered by a thin layer of unconsolidated sediments (Brigham-Grette and Carter, 1992; Fritz et al., 2012). During the Late Wisconsin, the YCP was partly covered by the Laurentide Ice Sheet, which reaches its maximal extension probably between 23 and 18 ka BP, when it extended slightly west of Herschel Island (Dyke and Prest, 1987). The western parts of the YCP, which probably were not covered by glaciers during the whole Quaternary, are characterized by alluvial fans formed by streams from the British Mountains, merged deltas and coastal lagoons

(Scudder, 1997). Permafrost on the YCP is continuous; ice content is high and ice wedges are abundant (Mackay, 1971).

The focus of this study is on the coastal and nearshore zone of Herschel Island (69°36' N; 139°04' W, Figure 6), located at the most northern point of the Yukon Territory, Canada, in the western part of the Canadian Beaufort shelf, covering an area of 108 km<sup>2</sup> (Lantuit and Pollard, 2008). It is part of the Yukon Coastal Plain and is an ice-pushed structure that formed during the westward advance of the Laurentide ice sheet in the Buckland Stage of the Wisconsin Glaciation. The island is separated from the mainland by the very shallow Workboat Passage (< 3 m deep, ca. 2 km wide), where longshore currents often cause resuspension of sediments. The north coast is exposed to the maximum wave energy of the Beaufort Sea in late summer, while the east coast gets protected by the island itself (Hill et al., 1991). The coast of Herschel Island is dominated by steep cliffs, which are up to 50 m high (Mackay, 1971; Fritz et al., 2012). The coastal slopes are affected by excessive thermo-erosion, with several retrogressive-thaw-slumps and active-layer detachment slides (Lantuit and Pollard, 2008).

The arctic climate at Herschel Island and the southern Beaufort Sea is characterized by long, cold winters and short summers. Temperatures vary from about -30 °C in winter (December-February) up to 15 °C in summer, with a peak in July and a mean annual temperature of -9.4 °C (Giovando and Herlinveaux, 1981; Burn and Zhang, 2009; Figure 8). During open water seasons, winds dominantly blow from E and NW directions, while NW wind conditions are more common in August and September, when storms become more frequent (Hill et al., 1991; Figure 7). Although fetch lengths in the Beaufort Sea may extend 1000 km and significant wave heights may exceed 4 m, thereby enhancing coastal erosion, the sedimentary input from coastal erosion to the Beaufort Sea is very low compared to the one of the Mackenzie River (below 5 %, Hill et al., 1991; Radosavljevic et al., 2015).

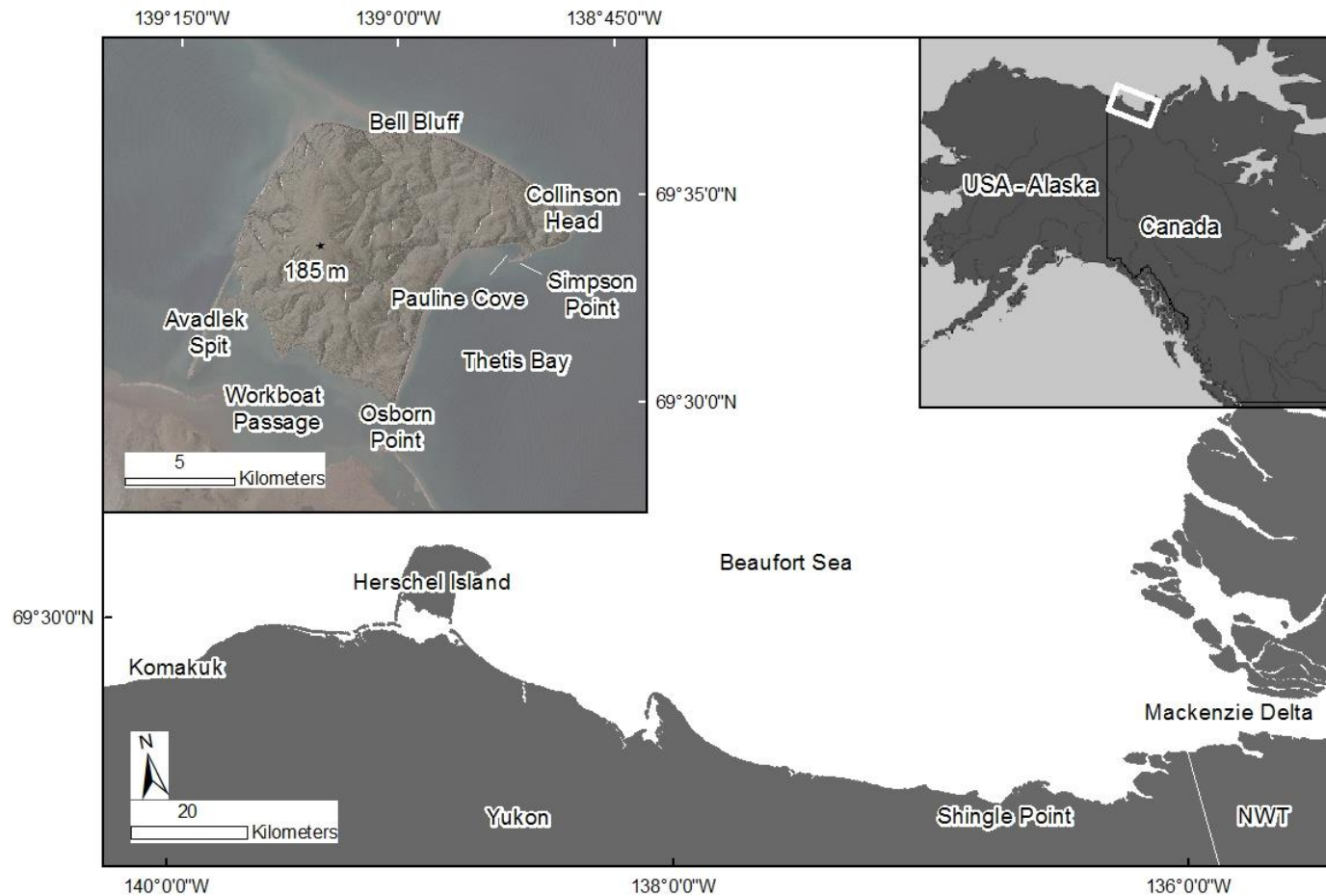


Figure 6: Map of the study area. Upper right: Location of the study area (white rectangle) near the northernmost border of Canada and the USA. Lower center: closer view on the white rectangle from the upper right picture, including the Mackenzie Delta, the southern Canadian Beaufort Shelf, the Yukon Coastal Plain and Herschel Island. Upper left: area of interest of this study. A Landsat 8 (OLI) true color (band composition 432) image is underlying by a hillshaded 2 m DEM at Herschel Island and a hillshaded 16 m DEM at the Yukon Coastal Plain. Important geographical locations are mentioned around Herschel Island, as well as the highest point in the western central part of the island (185 m, Burn and Hattendorf, 2011).

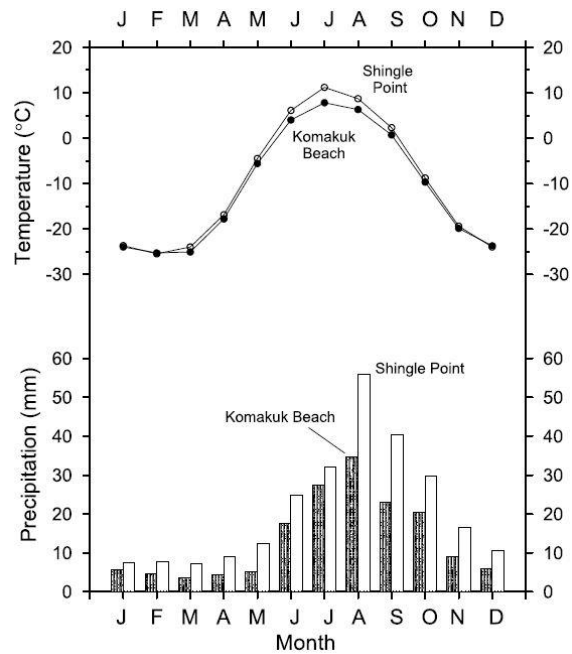


Figure 8: “Mean monthly temperature and precipitation for Komakuk Beach and Shingle Point, Yukon Territory. The mean annual temperatures at Shingle Point and Komakuk Beach are  $-9.9^{\circ}\text{C}$  and  $-11^{\circ}\text{C}$ , respectively, and mean annual precipitation totals are 254 and 164 mm.” (Burn and Zhang, 2009). Data is provided by Environment Canada.

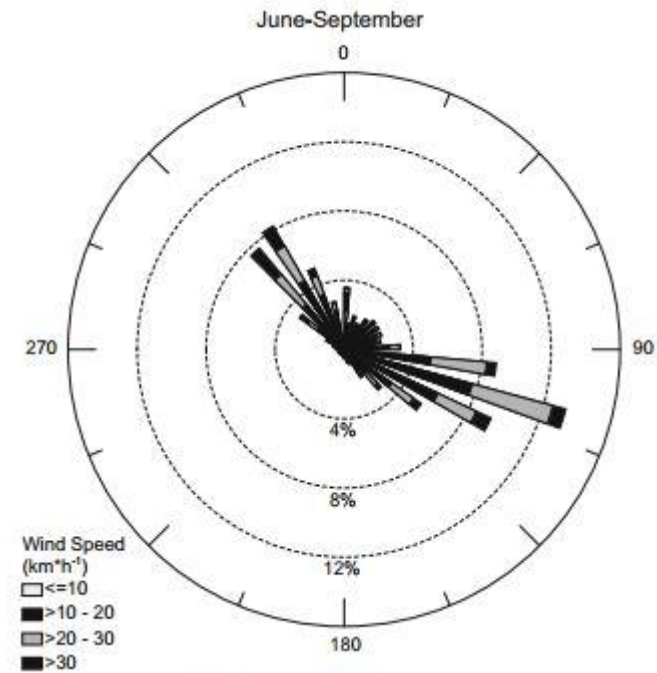


Figure 7: "Wind direction and frequency in the ice-free period (June-September), observed at the weather station on Simpson Point, Herschel Island, from 2009 to 2012." (Radosavljevic et al., 2015).

## 4. Materials & Methods

---

### 4.1. Landsat Images Acquisition

---

Landsat images were downloaded from the United State Geological Survey (USGS; <http://usgs.gov/>). Included are images with data from Landsat TM (Thematic Mapper) from 1986 to 2011, ETM+ (Enhanced Thematic Mapper +) from 1999 to 2016 and OLI/TIRS (Operational Land Imager/Thermal Infrared Sensor) from 2013 to 2016. Images from Landsat ETM+ after 2003 were mostly excluded, since the SLC failed onboard. Only ETM+ image data from path 67 was used in this study, because the AOI lies within the central part of the image, where the loss of data is minimal (Storey et al., 2005). Considering the long arctic winter with continuous ice cover, only images from June, July, August and September without significant sea ice and cloud cover has been chosen. Due to the temporal resolution of all used Landsat satellites (16 days), five images could be used per year in maximum. In total there were 68 useable images (TM: 48, ETM+: 12, OLI/TIRS: 8).

### 4.2. Landsat Images Pre-Processing

---

To get at-sensor radiance, level 1G data was calibrated with the published coefficients (ETM+, OLI) or with the scene-specific calibrator values (onboard, TM, Masek et al., 2006). Calibrated images were then corrected to top-of-atmosphere (TOA) reflectance through correction for solar zenith, Sun-Earth distance, bandpass (sensor-specific) and solar irradiance. To get an accurate estimation of Surface Reflectance (SR), scattering and absorption of radiance by the atmosphere need to be compensated. The Landsat SR product is acquired from TOA reflectance ( $\rho_{TOA}$ ), which can be expressed as

$$\rho_{TOA} = T_g(O_3, CO_2, NO_2, CH_4) \cdot [\rho_{R+A} + T_{R+A} \cdot T_g(H_2O) \cdot \rho_S \cdot (1 - S_{R+S} \cdot \rho_S) - 1]$$

with

$\rho_S$  = surface reflectance

$T_g$  = gaseous transmission

$T_{R+A}$  = Rayleigh and aerosol transmission

$\rho_{R+A}$  = Rayleigh and aerosols atmospheric intrinsic reflectance

$S_{R+A}$  = Rayleigh and aerosols spherical albedo.

For a more detailed description of the atmospheric correction of Landsat images, see Masek et al. (2006). It is known, that Landsat SR is well correlated to MODIS SR, even though Landsat ETM+ SR values tend to be ~1% higher in mean, with decreasing offset at rising wavelengths (blue band: nearly 100 % higher values; NIR band: nearly identical values). Nonetheless, this atmospheric correction is still the best one known (Nazeer et al., 2014), with the best approximation for land and sea surfaces.

### 4.3. Landsat Images Processing

---

The SR pre-processed images were classified using the USGS cf-mask to eliminate land, sea ice, clouds and cloud shadow. This masking is not perfect; cloud shadows cannot be masked fully without hitting the absorption of suspended particles. The result is a raster image with (nearly) only water surfaces (sea, lakes and rivers). A pre-defined area of interest (AOI) around Herschel Island was used to extract the image to save computing resources. All scenes without artefacts and matching wind conditions (see below) were used to calculate mean statistical parameters for visualization.

Thermal Infrared image data from all Landsat satellites do not receive an atmospheric correction, thus they are only available as L1T data product. According to Wukelic et al. (1989), the conversion from digital numbers to spectral radiance ( $R_\lambda$ ) and then to uncorrected temperature (at-sensor temperature,  $T_U$ , [K]) is given by

$$R_\lambda = R_M \times DN + R_A$$

and

$$T_U = K_2 \times \left[ \ln \left( \frac{K_1}{R_\lambda} \right) + 1 \right] - 1$$

with

$R_M$  = radiance multiplier

$R_A$  = radiance add

$K_1, K_2$  = thermal constants



where  $R_M$ ,  $R_A$ ,  $K_1$  and  $K_2$  are given by the Landsat Metafile (MTL). These at-sensor temperatures are not surface temperatures, but are good approximations of sea surface temperatures. Even though corrected temperature values get closer to measured surface temperatures, they are still not exact. The higher computation investment was not considered to warrant the slightly increased accuracy, hence uncorrected temperatures are sufficient for this study. The conversion to corrected temperatures using the downwelling sky irradiance for a clear sky and measured surface temperatures is described in Wukelic et al. (1989). All calculations were made with ESRI ArcMAP 10.4.1.

#### 4.4. Boxplots

---

In order to facilitate interpretation of the imagery, a set of test areas was established along the coast of Herschel Island. 17 zones were defined in total to cover different coastal orientations and distances from the shoreline (Figure 13). Each of these zones was made of 200 cells, which were then averaged to aggregate means or medians to form indices representative for each zone. These values were extracted using raster to point in the spatial analyst toolbox in ArcMap. The attribute tables were then exported as .txt and processed in Microsoft Excel. Boxplots were compiled in MATLAB.

#### 4.5. Wind Data

---

Wind data was collected from the climate archive of the Canadian government (<http://climate.weather.gc.ca>). The investigated weather stations were Herschel Island and Komakuk Beach. Data from Komakuk Beach was used, when the station on Herschel Island failed and before 1994, when hourly weather monitoring on Herschel Island started. Hourly weather monitoring on Komakuk Beach started in 1994, too, but 4 measurements/day were collected from 1973 on (00:00, 06:00, 12:00 and 18:00). To receive consistent data, only measurements from 00:00, 06:00, 12:00 and 18:00 were extracted from this dataset from 1994 on.

Wind speed and direction were acquired for the date of the Landsat scene and two days in advance, in total 12 measurements per scene. When six out of the last eight measurements (date of the scene plus one in advance) or 9 out of 12 had comparable wind directions, the conditions were assumed to be continuous and the scene was used in this study. In total, 18 scenes show continuous ESE wind conditions (TM: 13, ETM+:

4, OLI: 1), 8 continuous NW wind conditions (TM: 4, ETM+: 3, OLI: 1) and 9 changing wind conditions (TM: 9, ETM+:1).

#### 4.6. SPM Algorithms

---

Even though no in-situ data was available in this study, an attempt to calculate a SPM model based on Landsat SR data was initiated. Two MODIS scenes processed by Doxaran et al. (2012) based on field data were used to validate these attempts, since usable Landsat scenes of the same date existed (August 21, 2009 and September 12, 2011).

Even though the results of the SPM algorithm may differ due to different atmospheric correction methods (SR and RRS), SR Landsat data products were used, because the low signal-to-noise ratio over water surfaces makes RRS data products unusable (Doerffer et al., 1989).

The model was based on SR data from the red and NIR channels. Different combinations of these bands were used to calculate SPM to cover a wide range of concentrations: the red band was used to calculate low concentrations ( $\sim < 10 \text{ g/m}^3$ ); the band ratio (red/NIR) for medium concentrations ( $\sim 10 - 30 \text{ g/m}^3$ ); the halved sum of both bands showed the best results for high concentrations ( $\sim > 30 \text{ g/m}^3$ ). The whole model can be expressed as

$$SPM \left[ \frac{g}{m^3} \right] = \frac{C_L M_L \times C_M M_M \times C_H M_H}{C_L + C_M + C_H + C_1}$$

where  $C_L$ ,  $C_M$  and  $C_H$  are constants for low, medium and high concentrations and  $M_L$ ,  $M_M$  and  $M_H$  their respective models.  $C_1$  counteracts the unlikely case, if  $C_L + C_M + C_H$  being 0, the calculations wont fail, which was sometimes apparent in cloud shadows. The exact equations for  $C_L$ ,  $C_M$ ,  $C_H$ ,  $M_L$ ,  $M_M$  and  $M_H$  are given in the Appendix.

The model results show good agreements with the MODIS calculated SPM at September 12, 2011 (Figure 9). Both low and high concentrations were well represented, while medium concentrations were slightly overestimated (concentrations  $\sim 10 \text{ g/m}^3$  are calculated as  $\sim 15 \text{ g/m}^3$ ). All spatial SPM features were well displayed.

The SPM calculations from the Landsat scene of August 21, 2009, showed weak results for medium and high concentrations, which were mostly overestimated (Figure 10). Only low concentrations were well calculated by the model. Spatial SPM features were moderately displayed.

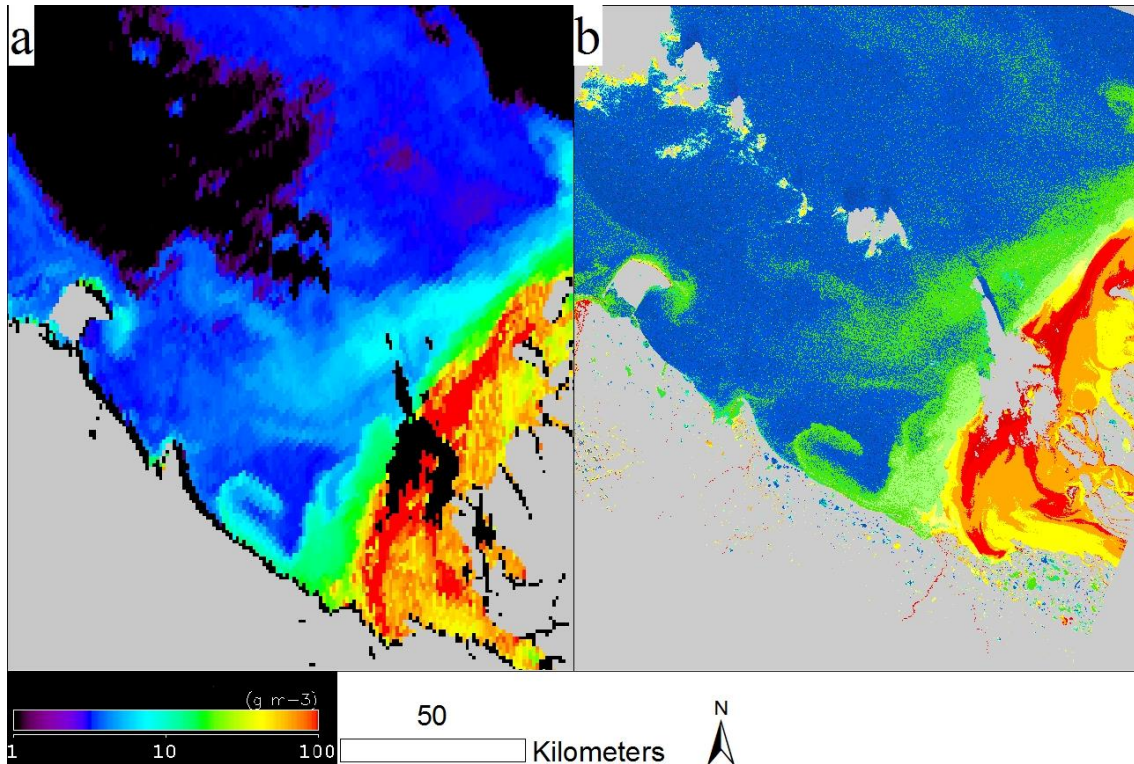


Figure 9: Comparing SPM calculations on September 12, 2011, between (a) SPM calculations based on MODIS RRS data from Doxaran et al. (2012) and (b) SPM calculations based on Landsat TM SR data with the model introduced in section 4.6. Both models have a logarithmic scale. No data is displayed in grey. The resulting datasets are in good agreement for low and high SPM concentrations, while medium concentrations are overestimated in (b).

After comparing the results for both pairs of scenes and numerous tuning attempts, development was stopped. Even though the results were satisfying, further development of an overall SPM model would have to rely on *in-situ* data.

Since no model attempt, including subsequent fine tuning of the algorithm, resulted in good agreements for both compared scenes, we compared data from the red band (655 nm, Figure 11) from the Landsat TM scene from August 21, 2011 with the modelling results from Doxaran et al. (2012). Generally, reflectance in the red band is well correlated to turbidity (Dogliotti et al., 2015) and thus, it should be well correlated to SPM concentrations. Comparing Figure 11 to Figure 9, the same spatial dispersal

patterns are displayed. The correlation in high, medium and low SPM concentrations is moderate. However, there are no absolute values available for turbidity in Figure 11.

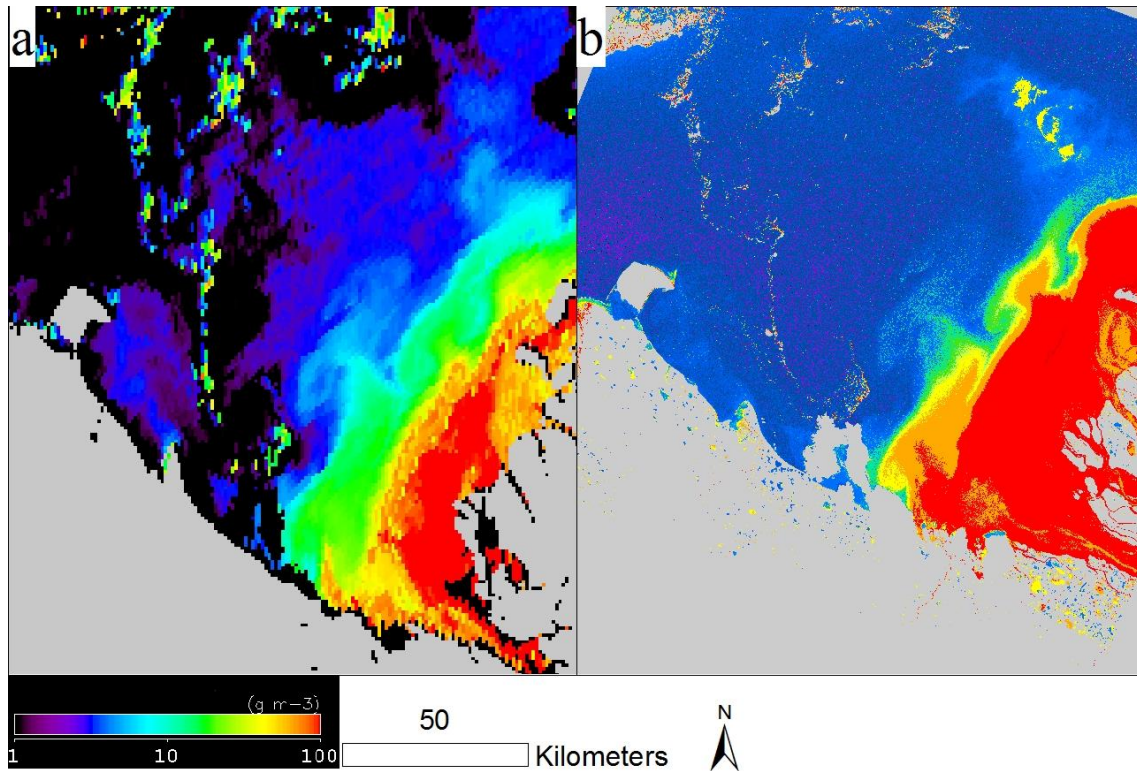


Figure 10: Comparing SPM calculations on August 21, 2009, between (a) SPM calculations based on MODIS RRS data from Doxaran et al. (2012) and (b) SPM calculations based on Landsat TM SR data with the model introduced in section 4.6. Both models have a logarithmic scale. No data is displayed in grey. The resulting datasets are in good agreement for low SPM concentrations, while medium and high concentrations are overestimated in (b).

The comparison between the SPM model and the red band showed that the red band was sufficient to resolve dispersal patterns in the nearshore zone. The advanced SPM model did not bring significantly superior additional information. Moreover, the computation of absolute values without *in-situ* measurements remains difficult, even though the developed model computed partly good results. Furthermore, the applicability of Landsat SR data for the development of related models is uncertain. Therefore, all the aforementioned factors led to the omission of the developed SPM model, leaving only the dataset of the red band for usage of this thesis.

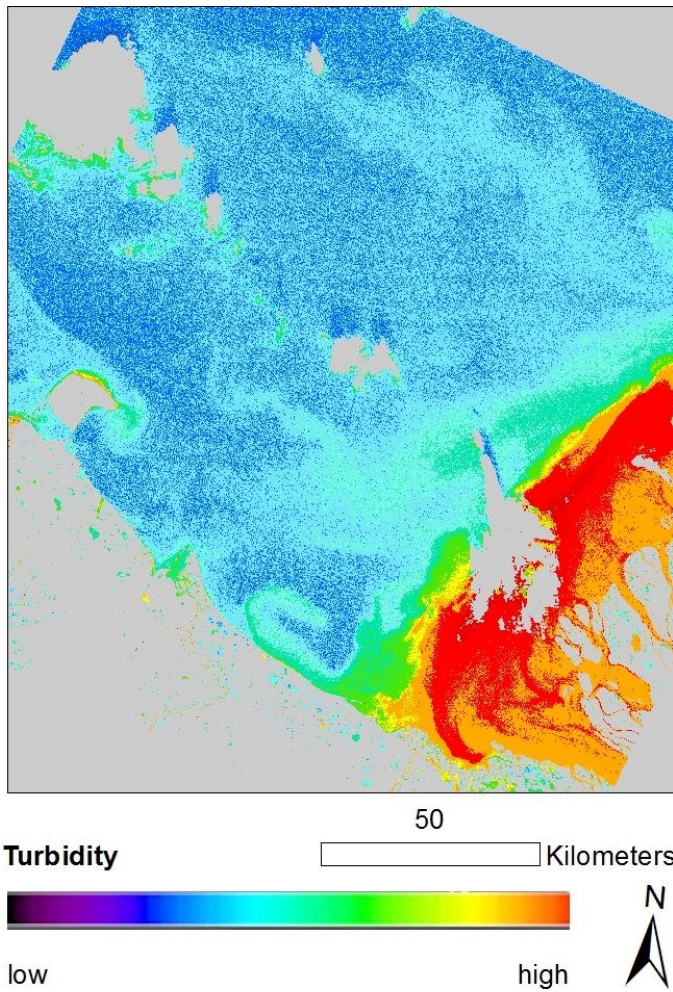


Figure 11: Spectral data from the red band from the Landsat TM scene taken on September 12, 2011. The spectral data is displayed in a logarithmic scale. No data is displayed in grey. Due to the absence of *in-situ* measurements and validation datasets, no absolute values were calculated. The comparison with Figure 9 shows similar dispersal patterns. High, medium and low SPM concentrations are moderately displayed.

## 5. Results

---

### 5.1. Landsat scene processing

---

35 images were used in total for the analysis (TM: 25; ETM+: 8; OLI: 2, Table 2). Several ‘anomalies’ had to be removed from the image before processing. These anomalies are caused by small sea ice floes (in early summer and late autumn) or by small clouds and their shadows that were not recognized by the USGS cf-mask. They had to be removed manually.

Furthermore, the USGS cf-mask had problems in recognizing small or thin parts of water or land surfaces (Figure 28). This often resulted in wrong statistical calculations in Pauline Cove and, at E wind conditions, west of Avadlek Spit, while Avadlek Spit itself is often not recognized as land surface. These areas have been masked afterwards.

| Acquisition Date (YYYY-MM-DD) | Sensor | Path/Row | Winddirection |
|-------------------------------|--------|----------|---------------|
| 1986-09-14                    | TM     | 67/11    | changing      |
| 1990-08-17                    | TM     | 66/11    | E             |
| 1990-09-16                    | TM     | 68/11    | NW            |
| 1990-09-25                    | TM     | 67/11    | NW            |
| 1992-08-06                    | TM     | 66/11    | E             |
| 1992-08-20                    | TM     | 68/11    | changing      |
| 1992-08-29                    | TM     | 67/11    | changing      |
| 1994-07-27                    | TM     | 66/11    | changing      |
| 1994-08-12                    | TM     | 66/11    | changing      |
| 1994-09-11                    | TM     | 68/11    | E             |
| 1995-07-12                    | TM     | 68/11    | E             |
| 1997-07-19                    | TM     | 66/11    | E             |
| 1998-07-22                    | TM     | 66/11    | E             |
| 1997-08-02                    | TM     | 68/11    | NW            |
| 1998-07-13                    | TM     | 67/11    | E             |
| 1999-08-08                    | TM     | 68/11    | E             |
| 1999-08-10                    | TM     | 66/11    | E             |
| 1999-09-02                    | TM     | 67/11    | E             |
| 1999-09-10                    | ETM+   | 67/11    | E             |
| 1999-09-18                    | TM     | 67/11    | E             |
| 1999-09-26                    | ETM+   | 67/11    | NW            |
| 2001-08-30                    | ETM+   | 67/11    | changing      |
| 2002-09-11                    | ETM+   | 66/11    | NW            |
| 2004-08-22                    | ETM+   | 67/11    | E             |
| 2006-07-26                    | TM     | 68/11    | E             |

|            |      |       |          |
|------------|------|-------|----------|
| 2007-08-23 | TM   | 67/11 | changing |
| 2008-06-30 | ETM+ | 67/11 | E        |
| 2009-07-27 | TM   | 67/11 | NW       |
| 2009-08-21 | TM   | 66/11 | changing |
| 2009-09-05 | ETM+ | 67/11 | NW       |
| 2010-08-15 | TM   | 67/11 | E        |
| 2011-09-12 | TM   | 66/11 | changing |
| 2013-07-15 | OLI  | 66/11 | E        |
| 2014-07-02 | OLI  | 66/11 | NW       |
| 2016-08-07 | ETM+ | 67/11 | E        |

Table 2: Used Landsat scenes after eliminating all anomalies. Data was acquired from the USGS. The retrieve of wind data and the classification is described in section 4.

## 5.2 Turbidity

The mean surface reflectance in the red band, which was used as proxy for turbidity, shows highest values during stable E wind conditions and lowest values during stable NW wind conditions (Figure 12). An area of high turbidity is consistently present at the NE coast of Herschel Island, which is dominated by high cliffs. Another area along the SE coast was also characterized consistently by high turbidity. Under stable E wind conditions, dispersal patterns at the NE coast showed longshore drift extending towards the west, resulting in a broader area of high turbidity at the NW coast than in (a) and (b).

The Workboat Passage is, under all three conditions, an area of increased turbidity and shows clear sediment pathways patterns (Figure 16), even though they are best displayed in (c) and very hardly recognizable in (b). A thin area around the whole island, showing high turbidity values under all conditions, can be attributed to coastal erosion and resuspension due to waves.

Interestingly, panels (a) and (b) (changing wind direction and NW winds) show quite similar dispersal patterns and a large difference to (c). Satellite images from the whole Canadian Beaufort Shelf indicate that the larger extent of the Mackenzie River Plume may be the major influence causing this difference. On the other hand, other rivers entering the Arctic Ocean, such as the Firth River, entering the Arctic Ocean SW of Herschel Island, may only have minor influence on sediment dispersal.

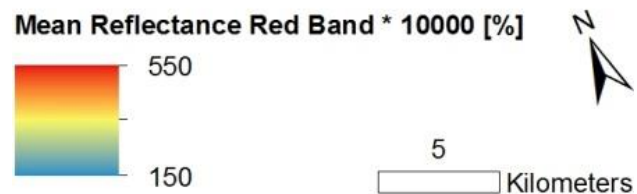
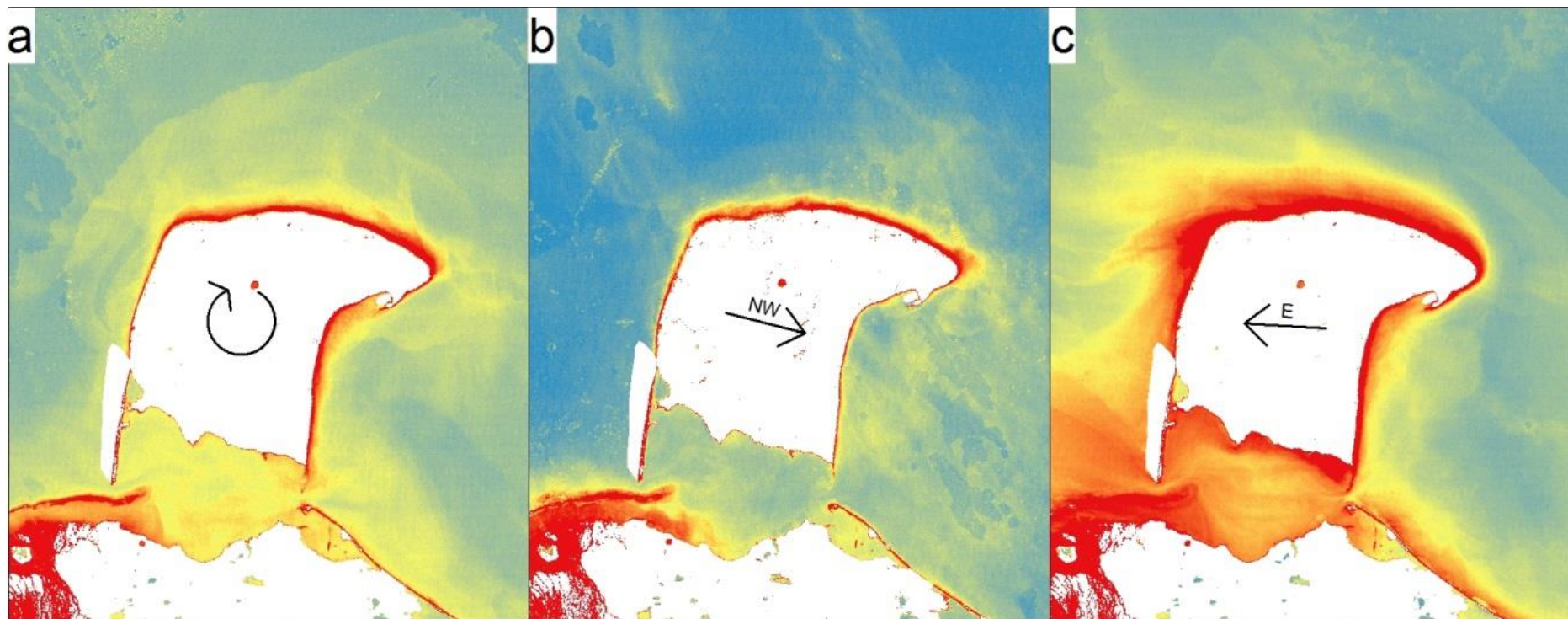


Figure 12: Mean surface reflectance in the red band, that was used as proxy for turbidity, for (a) changing wind conditions, (b) stable NW wind conditions and (c) stable E wind conditions. Prevailing wind conditions are mentioned with arrows in the centre of each picture. The number of used scenes per wind condition can be seen in Table 2. Red areas indicate areas of high turbidity, white areas indicate land surfaces or areas of failed atmospheric correction. Turbidity is highest in (c) and lowest in (b). Note the similar dispersal patterns in (a) and (b) compared to (c).



The comparison of the values retrieved at selected test areas spread along the Herschel Island coastline show similar patterns along the NE coast of Herschel Island during both NW and E wind conditions: turbidity decreases with increasing distance to the coast (zones 1-3, 5-7, 8-9), even when overall sediment concentration values are higher during E wind conditions (Figure 14, Figure 15). The same trend is present at the Workboat Passage during E wind conditions (zones 11 – 13), while during NW wind conditions, the values do not change significantly with increasing distance from the coast. Zones 14 and 15 do not show significant differences at both conditions. Under E wind conditions, zone 16 (Thetis Bay) has much higher values than zone 17 (Collinson Head), while during NW wind conditions, the contrary is the case. Interestingly, zones 11-17 show no significant differences during NW wind conditions, while the same zones show high variations during E wind conditions.

Generally, the range of the values (size of boxes and length of whiskers) observed in the test areas increases with decreasing distance to the coast; the only exception being zone 11 during E wind conditions. Additionally, the range of values (length of lines extending the boxes) for NW wind conditions is higher than at E wind conditions. There are also more outliers (red crosses) outside the 99 % confidence interval present for NW wind conditions.

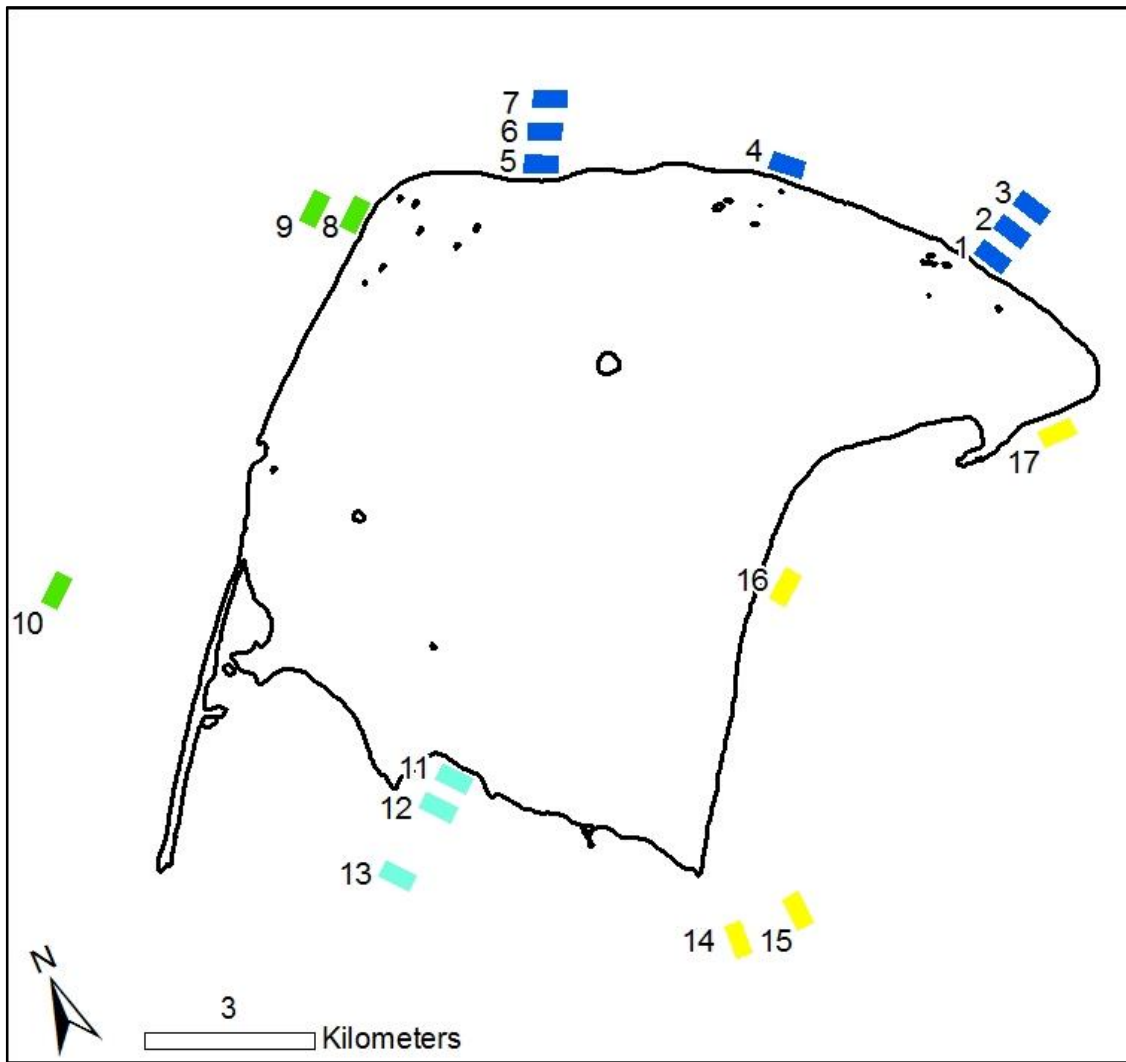


Figure 13: Naming and positions of the zones that were used to extract values from for the box and whisker plots. Zones 1 to 7 (blue) are located at ne NE coast, 8 to 10 (green) at the NW coast, 11 to 13 (cyan) in the Workboat Passage, 14, 15 (yellow) next to the eastern outflow of the Workboat Passage, 16 (yellow) at the SE coast in the Thetis Bay and 17 (yellow) at the SE coast near Collinson Head. Each number corresponds to the zone right of it. The coastline of Herschel Island is displayed in black.

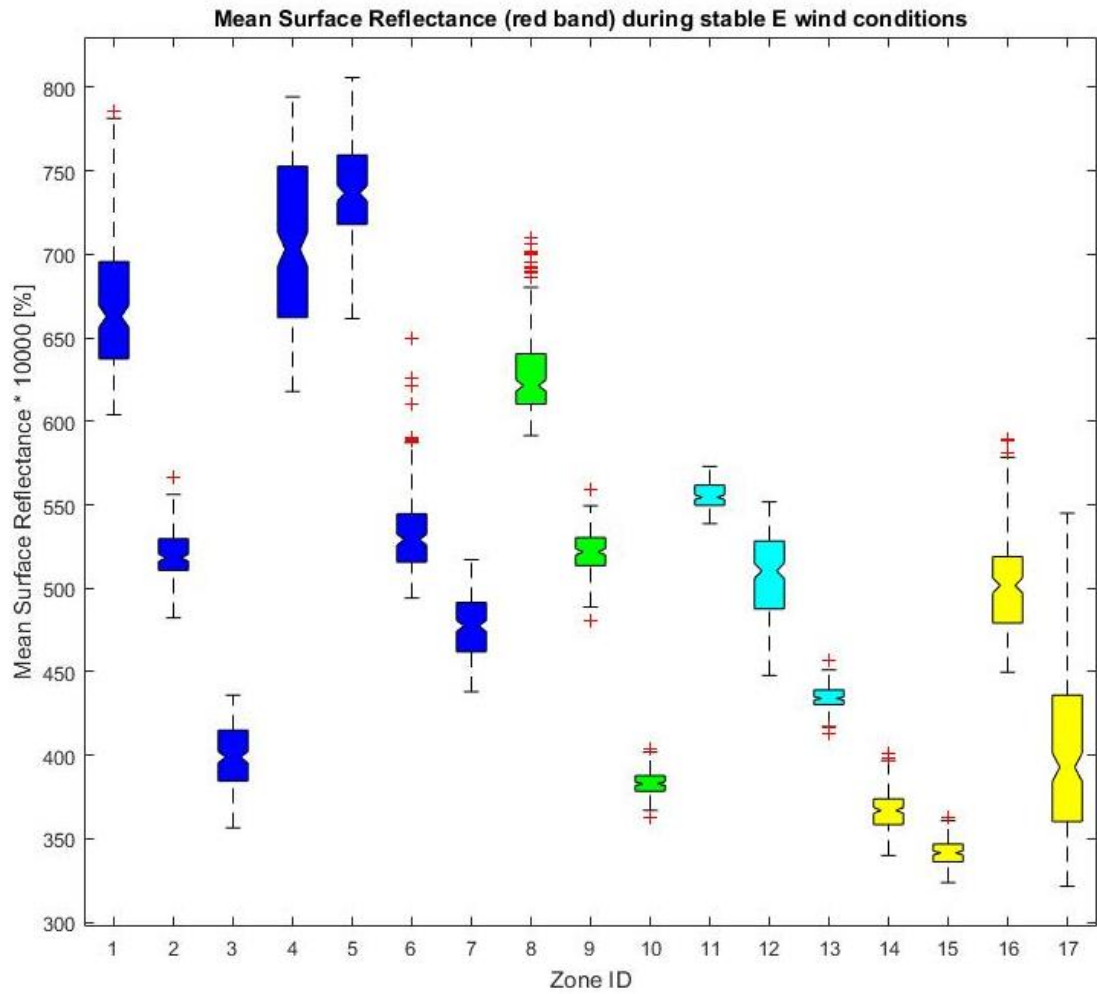


Figure 14: Box and whisker plot showing the surface reflectance values in the extracted zones displayed in Figure 13 for stable E wind conditions. 200 values are used per zone. Notches indicate the median value of the zone, the edges of the box indicate the 75 (upper edge) and 25 (lower edge) percentile. Whiskers (lines extending the boxes at the top and bottom) show the range of the data. Outliers (red crosses) are data points outside the 99 % confidence interval. Box and whisker plot was created using MATLAB.

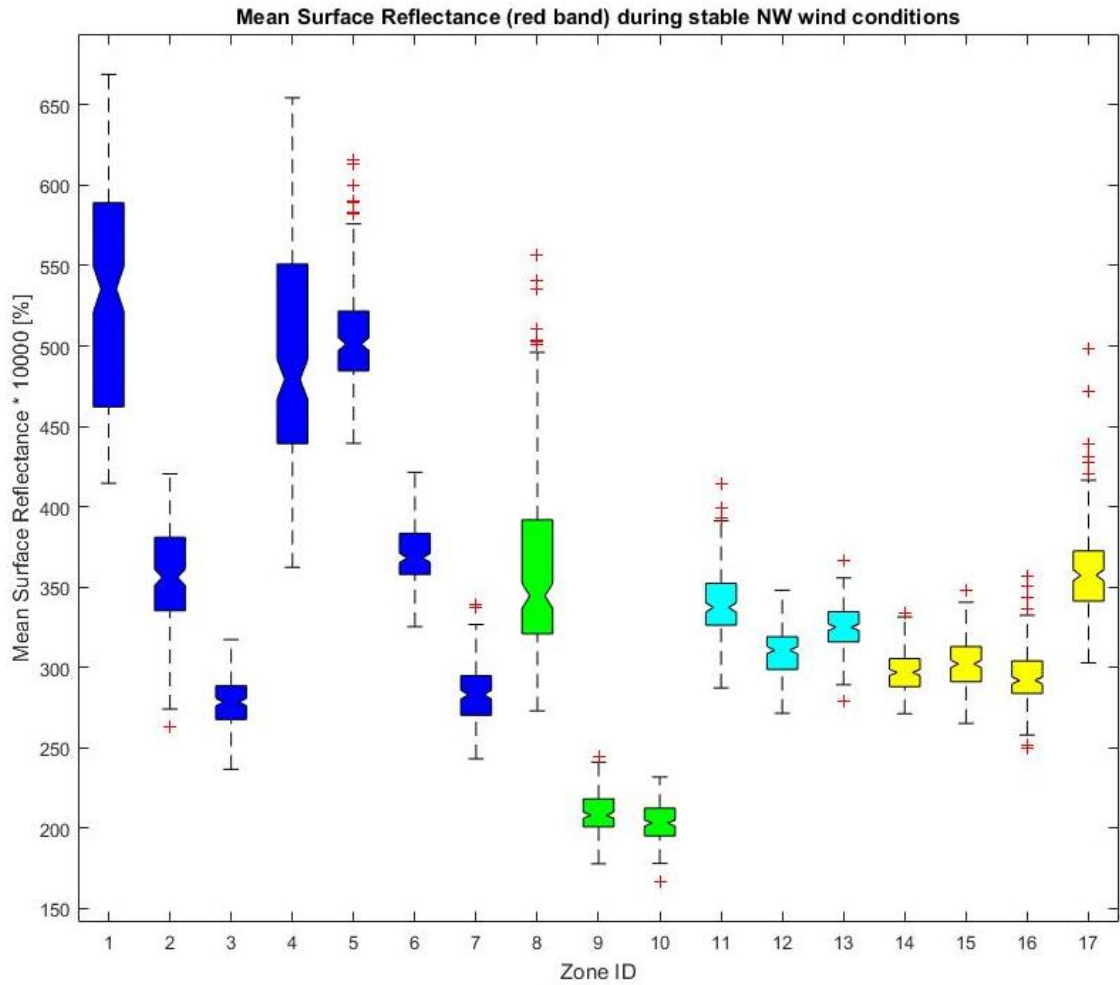


Figure 15: Box and whisker plot showing the surface reflectance values in the extracted zones displayed in Figure 13 for stable NW wind conditions. 200 values are used per zone. Notches indicate the median value of the zone, the edges of the box indicate the 75 (upper edge) and 25 (lower edge) percentile. Whiskers (lines extending the boxes at the top and bottom) show the range of the data. Outliers (red crosses) are data points outside the 99 % confidence interval. Box and whisker plot was created using MATLAB.

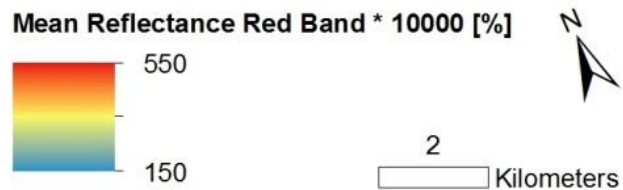
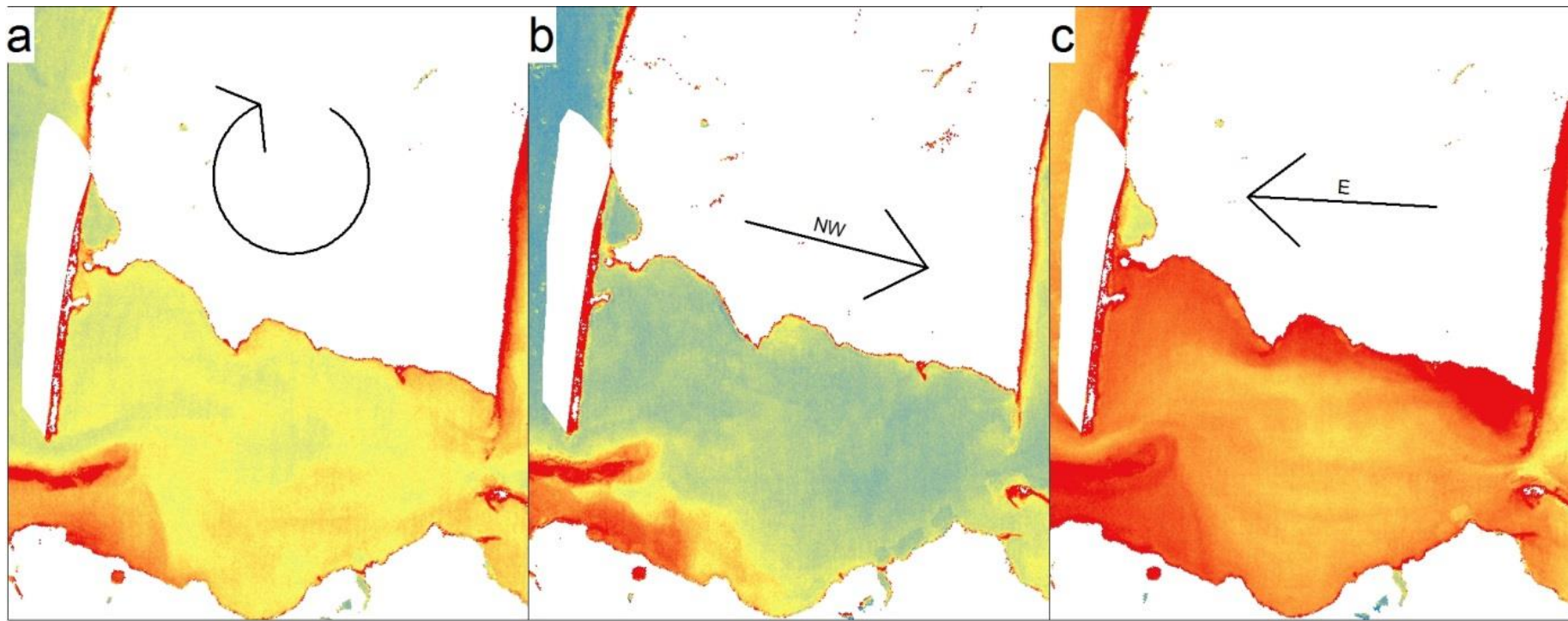


Figure 16: Mean surface reflectance from Workboat Passage in the red band, that was used as proxy for turbidity, for (a) changing wind conditions, (b) stable NW wind conditions and (c) stable E wind conditions. Prevailling wind conditions are mentioned with arrows in the centre of each picture. The number of used scenes per wind condition can be seen in Table 2. Red areas indicate areas of high turbidity, white areas indicate land surfaces or areas of failed atmospheric correction. The Workboat Passage shows increased turbidity values under all three conditions, but turbidity is not as high as along the north coast.

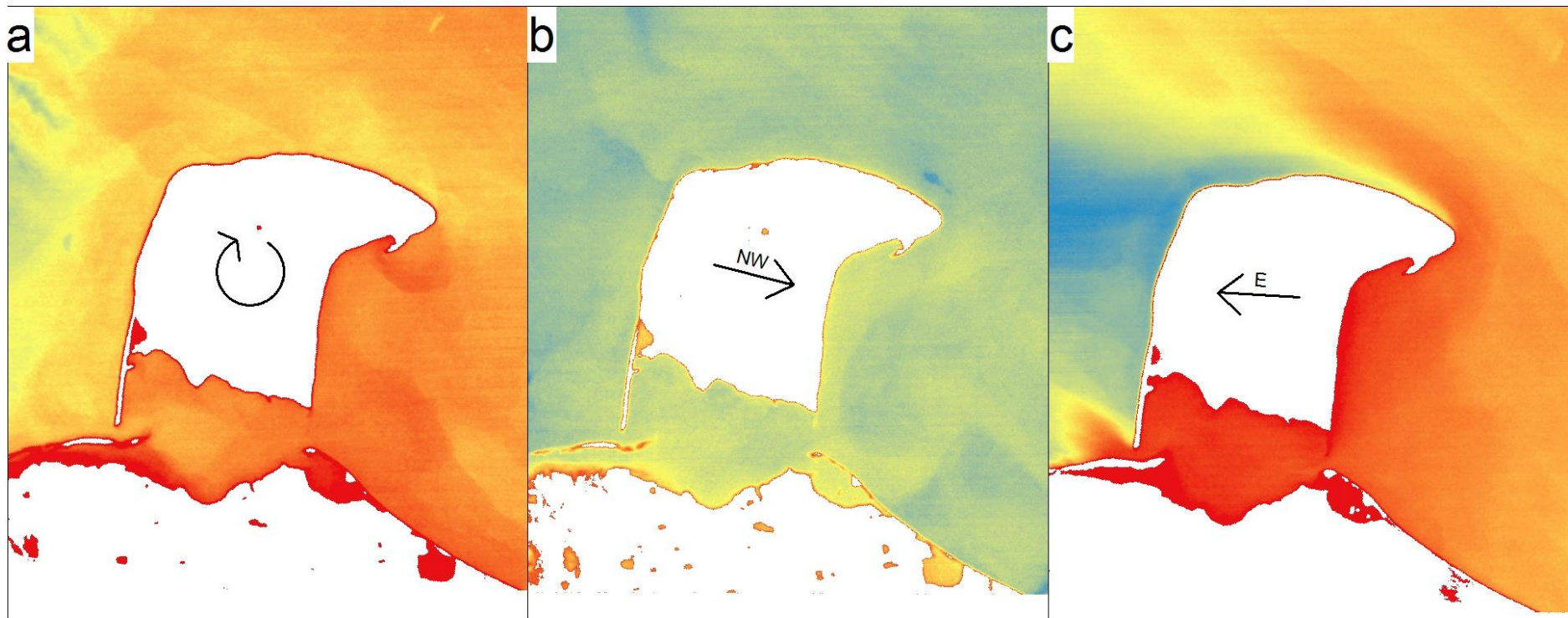
### 5.3 Sea Surface Temperature

---

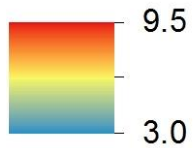
The uncorrected SST was calculated from the thermal infrared channels of Landsat TM, ETM+ and TIRS. The highest values were detected during stable E wind conditions along the SE coast of Herschel Island, as well as the lowest values near the NW coast (Figure 17 (c)). Figure 17 (a, changing wind conditions) shows nearly as high values at the SE coast as for E wind conditions, while values nearly as low as for E wind conditions were detected along the NW coast during stable NW wind conditions (Figure (b)). However, both do not contain the wide span of Figure (c), so the distribution of SST is much more uniform.

The SST spatial distribution show similar dispersal patterns compared to the ones for turbidity under changing and stable NW wind conditions, but absolute values are higher under changing wind conditions. This can be recognized at the SE and NW coasts (decreasing SST with increasing distance from the coast), as well as NE of Collinson Head. In contrast, when there are E wind conditions, SSTs rise with increasing distance from the coast along the NE coast and low SST are more uniformly distributed near the NE coast.

The Workboat Passage shows, in contrast to Figure 16, quite uniform SSTs for all three wind conditions (Figure 18). The SSTs behind the barrier islands near the Yukon coast is higher than in the Workboat Passage for all three wind conditions, but the freshwater input of the Firth River is not large enough to heat up the whole Workboat Passage. In contrast, the warm water from the Mackenzie River has the ability to heat it up.



Mean At-Sensor Temperature (°C)



5 Kilometers



Figure 17: Mean at-sensor (uncorrected) temperature from thermal infrared channels, for (a) changing wind conditions, (b) stable NW wind conditions and (c) stable E wind conditions. Prevailing wind conditions are mentioned with arrows in the centre of each picture. The number of used scenes per wind condition can be seen in Table 2. Red areas indicate areas of high SST, white areas indicate land surface areas. Land surface areas were eliminated using the difference of land and SST. Mean SST is highest in (c) and lowest in (b). Note the very cold SST in (c) at the NW coast of Herschel Island and the large contrast to the SE coast.

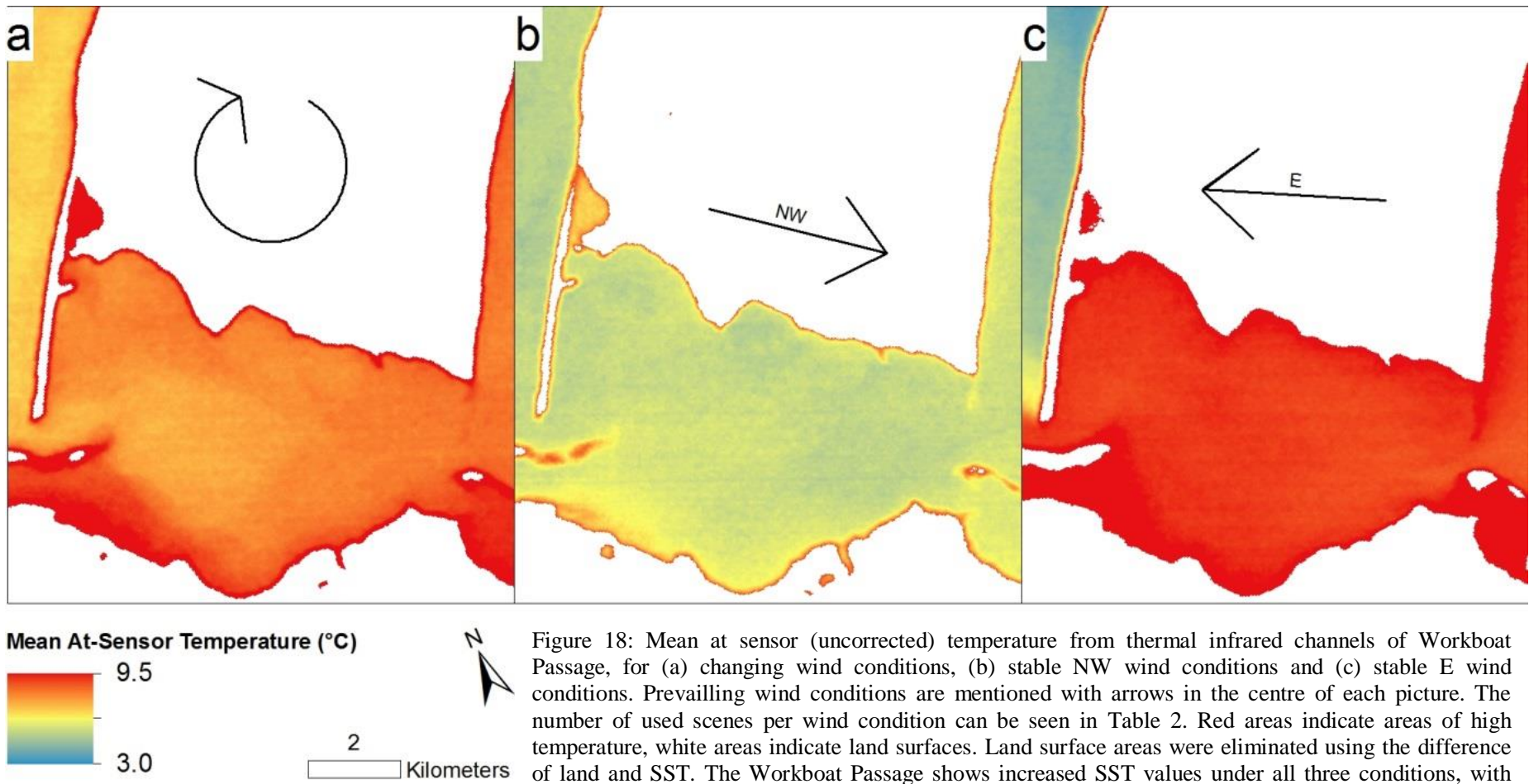


Figure 18: Mean at sensor (uncorrected) temperature from thermal infrared channels of Workboat Passage, for (a) changing wind conditions, (b) stable NW wind conditions and (c) stable E wind conditions. Prevailing wind conditions are mentioned with arrows in the centre of each picture. The number of used scenes per wind condition can be seen in Table 2. Red areas indicate areas of high temperature, white areas indicate land surfaces. Land surface areas were eliminated using the difference of land and SST. The Workboat Passage shows increased SST values under all three conditions, with highest values under E wind conditions.



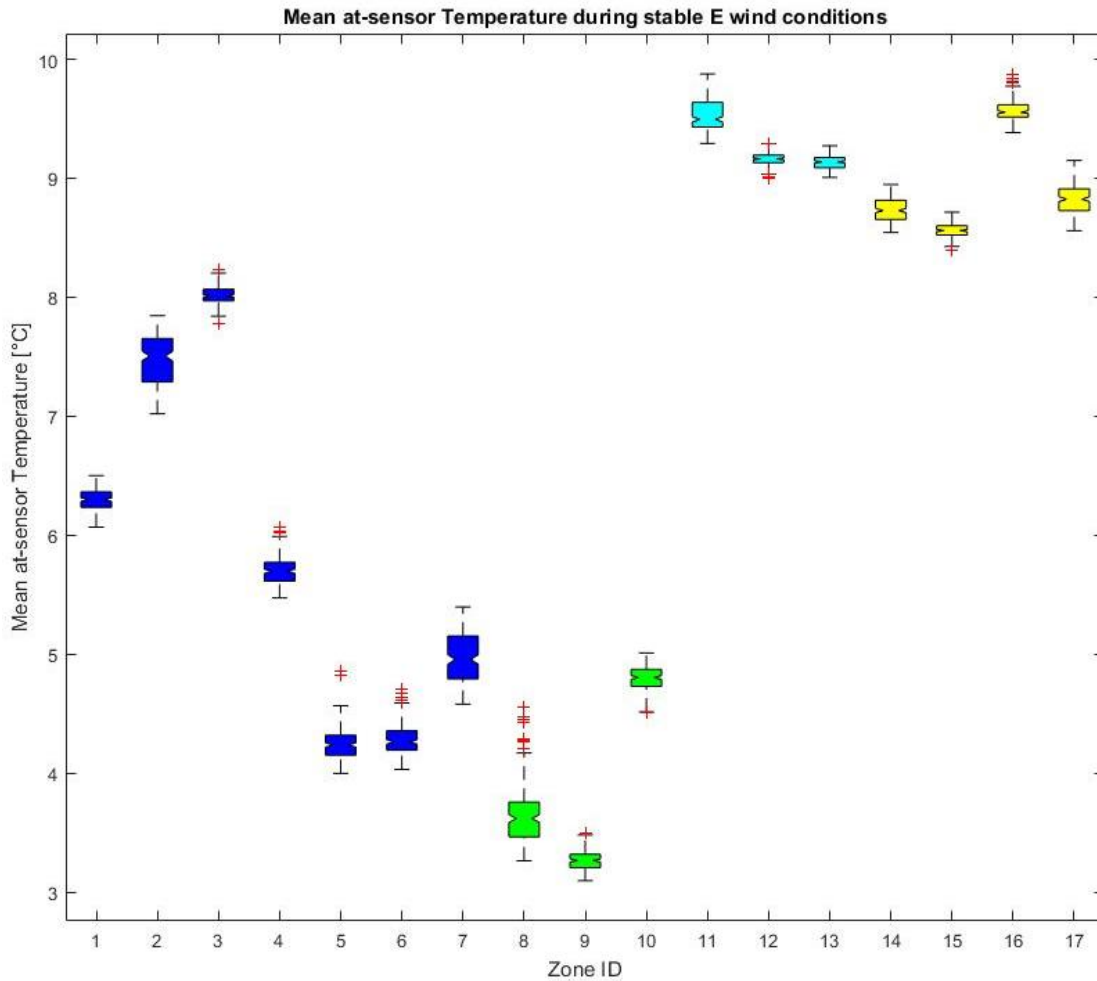


Figure 19: Box and whisker plot showing the at-sensor (uncorrected) temperatures in the extracted zones displayed in Figure 13 for stable E wind conditions. 200 pixels are used per zone. Notches indicate the median value of the zone, the edges of the box indicate the 75 (upper edge) and 25 (lower edge) percentile. Whiskers (lines extending the boxes at the top and bottom) show the range of the data. Outliers (red crosses) are data points outside the 99 % confidence interval. The box and whisker plot was created using MATLAB.

The comparison of values retrieved from selected test areas around the coast of Herschel Island (box and whisker plots, Figure 19, Figure 20) extracted from SST calculations highlights the different dispersal patterns along the NE coast and the similar patterns in the Workboat Passage and along the SE coast of Herschel Island. The SST show a clear increasing trend with increasing distance from the NE coast during E wind conditions, while it is the contrary under NW wind conditions (zones 1-7). The SST at the NW coast is higher under NW wind conditions than E wind conditions (zones 8-10).

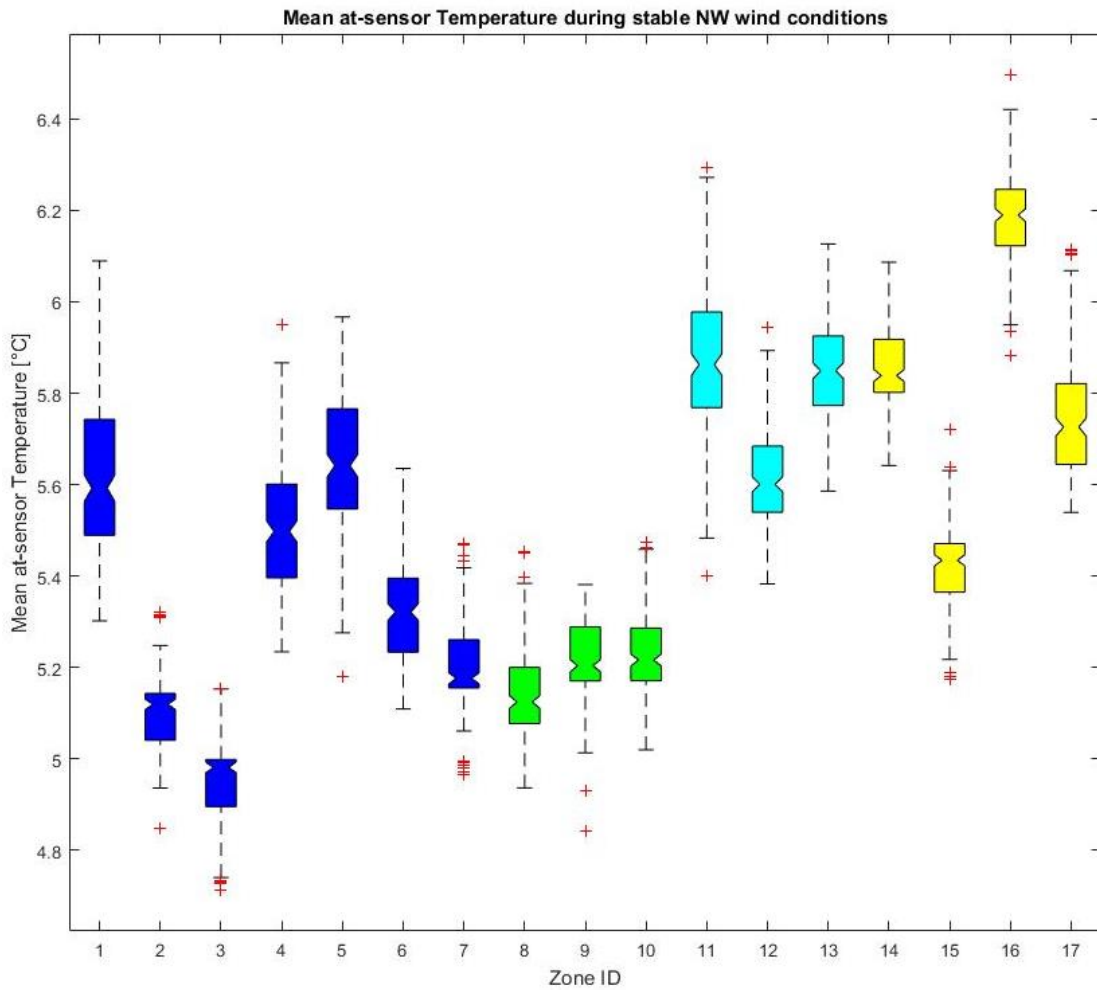


Figure 20: Box and whisker plot showing the at-sensor (uncorrected) temperatures in the extracted zones displayed in Figure 13 during stable NW wind conditions. 200 pixels are used per zone. Notches indicates the median value of the zone, the edges of the box the 75 (upper edge) and 25 (lower edge) percentile. Whiskers (lines extending the boxes at the top and bottom) show the range of the data. Outliers (red crosses) are data points outside the 99 % confidence interval. The box and whisker plot was created using MATLAB.

In the Workboat Passage, SST is much higher under E wind conditions and shows a smaller range. Generally, the range of values (size of boxes and length of whiskers) is higher under NW wind conditions, while there are more outliers outside the 99 % confidence interval under E wind conditions. In contrast to the turbidity, SST for E winds show no large variations in the zones 11 – 17 (Workboat Passage, Thetis Bay, Collinson Head), while the variations at NW wind conditions are higher for SST.

## 6. Discussion

---

### 6.1 Acquisition of Wind Data

---

Wind data was acquired in 6 h intervals to minimize the effects of different sampling methods over time (before 1994 it was measured in 6 h intervals; after 1994 hourly). The wind data was used to reconstruct the general wind direction patterns over several days, so the number of data points is sufficient for this task, even though some data is lost in the process. However, manually controlled random samples in the hourly dataset showed no significant anomalies compared to the 6 h interval used values per day. Moreover, this technique is the only way to provide consistent and comparable results for the whole observation period.

Wang et al. (2013) have shown that wind direction and wind speed changed significantly in the Beaufort region between 1970 and 2013. While mean wind speed in the coastal areas of the Canadian Beaufort Sea decreased slightly, maximum wind speed increased in June for most parts of the Canadian Beaufort Sea and in September in the Mackenzie Delta region. Wind direction changed in July and August slightly clockwise and in September anti-clockwise, meaning the wind direction in July and August changed to some degree to more easterly winds and to more northwesterly winds in September.

Fichot et al. (2013) argued, based on the  $S_{275-295}$  algorithm, that the general transport direction on the Canadian Beaufort shelf changed between 2002 and 2011 from eastward (NW wind) to northwestward (E Wind). The data used in this study does not show this trend; the number of used scenes with stable E wind conditions from 1997 – 2002 is even higher than from 2011 – 2016. This could show that the  $S_{275-295}$  algorithm is not the best method to distinguish fresh water from ocean water; nonetheless, it delivers sufficient results in detecting organic matter (Mannino et al., 2014).

The number of used scenes in this study before 2000 (21) is higher than the ones used after 2000 (14). The applied acquisition method might lead to the conclusion of a more variable wind regime after the year 2000; however the poor temporal resolution of Landsat satellites requires a comprehensive dataset for final confirmation. The used

Landsat dataset, despite its caveats, cannot confirm or infirm the wind pattern changes observed in the literature.

## 6.2 Significance of the results without *in-situ* data

---

In remote sensing, ground validation is an essential part of the retrieval of land or sea surface information. However, in remote locations such as the Arctic coast, field validation is often challenging and remote sensing studies often rely on the relative comparison of spectral data to introduce new analytical approaches. Considering the aim of this thesis (performing a test study), this approach provides satisfactory results. An estimation of absolute turbidity and SPM values remains difficult with the used dataset, but relative differences of turbidity and SST can be resolved. Therefore, the products are a good basis method developing models in the absence of *in-situ* data. The results of this thesis clearly show differences in turbidity and SST under different wind conditions in the nearshore zone of Herschel Island.

The strong gradients of turbidity from the nearshore to offshore zone indicate that most of the suspended material in the nearshore zone of Herschel Island is transported alongshore and only limited amounts are transferred offshore. Estimations on the amount of suspended sediment transported away from the coast are rare; Pfalz (2017) estimated that ~ 20 % of the eroded material by the Yukon rivers (Mackenzie excluded) and coastal erosion is stored in Herschel Basin, meaning large parts of the rest would be deposited in coastal areas.

Bailard (1982) suggests, that the discrimination between onshore and offshore sedimentation of suspended sediment is a function of wave height. His modeling results indicate a threshold value of significant wave height of 1 m to transport suspended sediment offshore. According to Hill and Nadeau (1989), significant wave height in the Beaufort Sea exceeds 1.2 m only during strong storm events and the majority of waves are below 0.8 m of significant wave height. Even though Bailards model was constructed for a tropical beach, general material behavior is comparable and thus, the model is appropriate for this comparison. This supports the hypothesis, that most of the suspended sediment in the nearshore zone of Herschel Island gets not transported offshore.

Bloesch (1982) measured resuspension in Lake Erie (Ontario, Canada) using sediment traps in several water depths: 9 m (nearshore), 25 m (mid-shore) and 40 m (offshore). His results show that resuspension in the nearshore zone occurs more frequently than offshore. In the nearshore zone, resuspension is mainly caused by waves, while bottom currents are the main cause for offshore resuspension. Héquette and Hill (1993) measured strong seaward directed bottom currents caused by strong NW storms along the Beaufort Sea coast. The strong currents reach speeds up to 0.5 m/s (mean currents speed: 0.08 – 0.16 m/s, Fissel and Birch, 1984), playing a possible role in offshore sediment dispersal.

Unfortunately, the resuspension caused by these bottom currents cannot be detected by multispectral satellite imagery. However, it supports the hypothesis, that suspended sediment is transferred offshore during storm events and transported alongshore during moderate wind conditions.

### 6.3 Controlling factors

---

Brenon and Le Hir (1999) pointed out several factors influencing turbidity in coastal and estuarine waters. Those are (i) bathymetry, (ii) material behavior, (iii) tides and (iv) freshwater input by rivers. Bathymetry may be the major influencing factor, while it's the only factor influencing the other ones listed (Hill et al., 1991).

Comparing bathymetric data to the mean turbidity around Herschel Island, substantial differences around the island are visible under stable E winds (Figure 21). While high turbidity along the SE coast is mostly restricted to areas of depths below 6 m, high turbidity along the NE coast is present until depths of 30 m. Towards Herschel Basin in the SE of Herschel Island, turbidity rapidly decreases, as well as towards the NE below 30 m depth. At the W coast, a harsh break is present along the 20 m isobath.

The high resolution bathymetry of the Workboat Passage shows high depths at the in- and outflow (up to 10 m) and increasing depths from the Yukon main land towards Herschel Island, until the coast raises out of the ocean (Figure 22). Interestingly, turbidity is higher in areas of higher depths and lower in the center of the Workboat Passage. This may indicate that water flows throughout the Workboat Passage predominantly in the northern parts, causing resuspension and 'carving out' small

scaled valleys at the seafloor. Turbidity at the in- and outflow is low compared to the rest of the Workboat Passage.

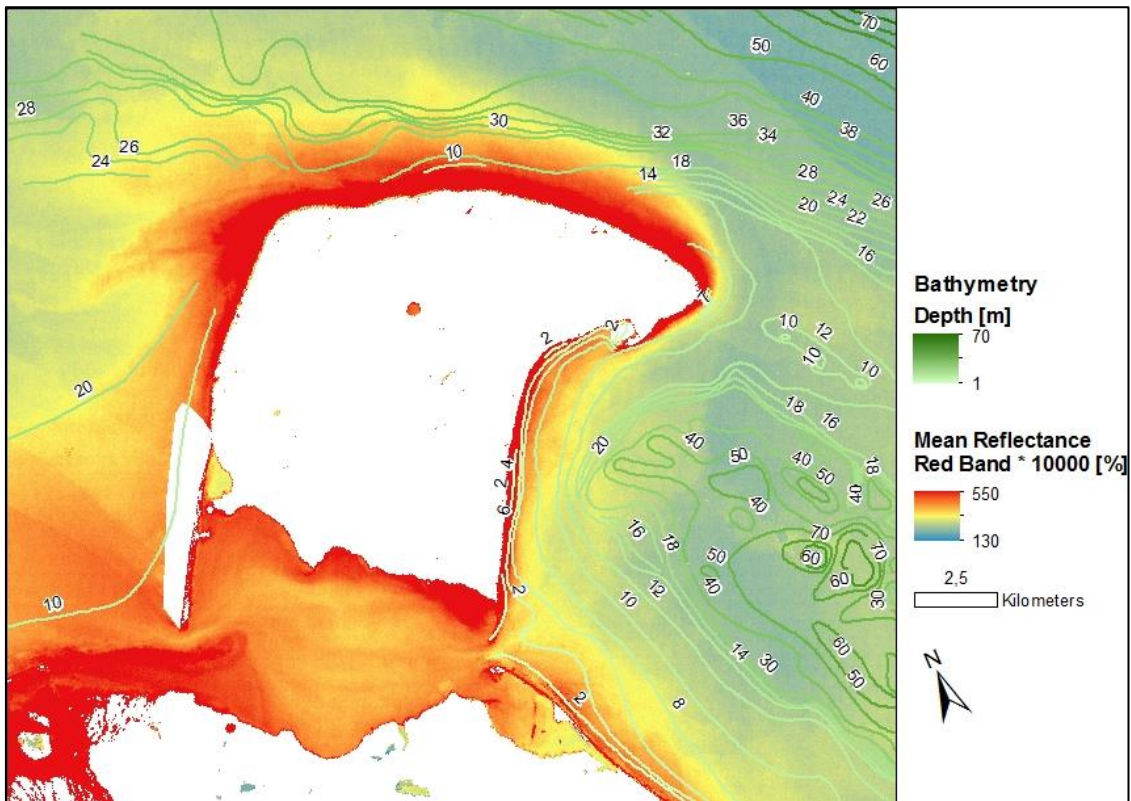


Figure 21: Bathymetry in the region of Herschel Island, with underlying turbidity calculations from this study during stable E wind conditions. Areas of high turbidity reach depths of up to 30 m along the NE coast and 20 m along the NW coast. Along at the E coast, high turbidity is detected until depths of 6 m. Nautical charts of the Beaufort Sea, Federal publications Inc.

Wind speed is the main driving force of nearshore bottom currents (Hill et al., 1991; Héquette and Hill, 1993). In surface and coastal waters, currents strongly correlate with wind direction and strength. This correlation is weaker, when bottom water becomes decoupled from the wind affected surface water. According to Hill et al. (1991), the entrainment of sediment by bottom currents is common in the nearshore zone and rare offshore. It's influence on sediment dispersal is suggested to be relatively high in the nearshore zone, but difficult to measure (Hill et al., 1991). Since tidal range is small in the Beaufort Sea (0.4 m), their effects on resuspension of sediments only affects a small fringe around the coasts.

The influence of the material behavior is mainly based on physical parameters such as its mass and particle cohesion (Hjulström, 1939). An increase in the mass of particles of the Mackenzie River was suggested by Doxaran et al. (2015). Sediments in the

nearshore zone of Herschel Island shifted from predominantly silty (Pelletier et al., 1984) to coarser grain sizes (higher content of sand and gravel, Jerosch, 2013) in the last decades, while finer grain sizes are deposited offshore. According to Bailard (1982), this might be caused by an increase of significant wave height to  $> 1.15$  m, where suspended sediment gets transported farther offshore than bedload (here assumed as gravelly sediments). The impact of these bigger particle mass of nearshore sediments on the resuspension to the water surface (where it is detectable by multispectral satellite imagery) is not yet investigated. Due to its higher mass, the particles experience a shorter times in suspension. Therefore, turbidity detectable by satellite imagery should be reduced.

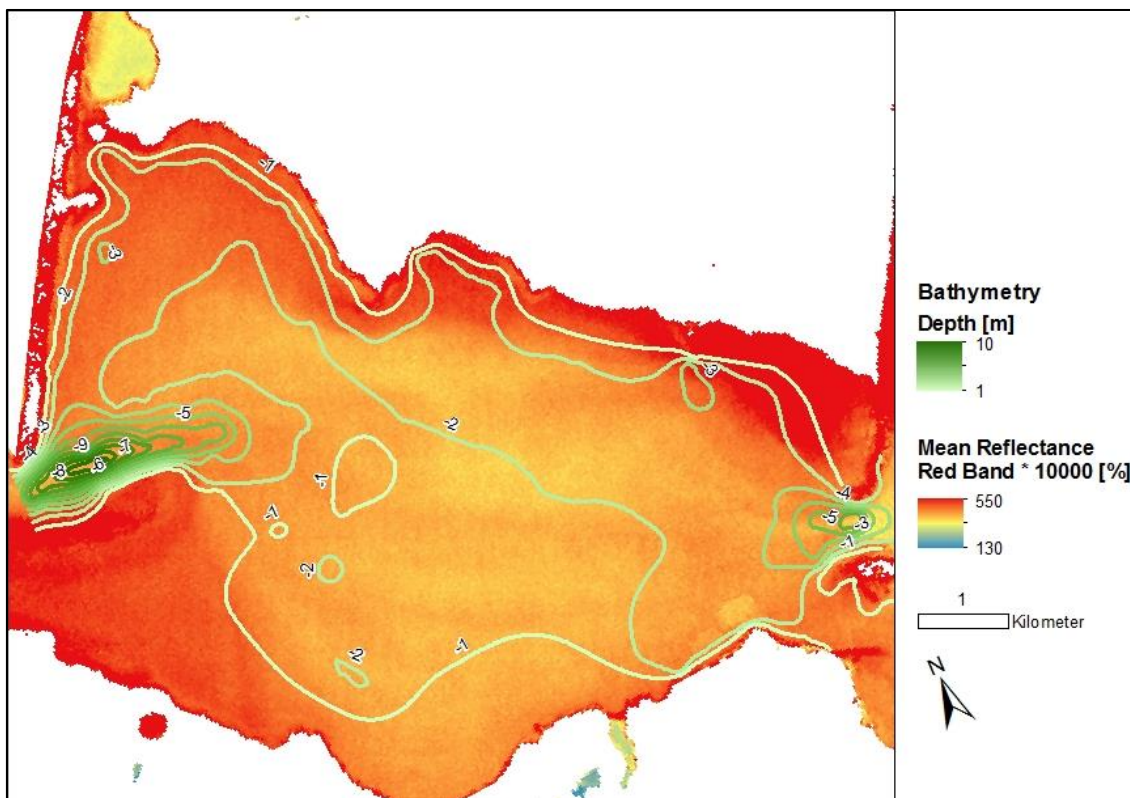


Figure 22: Bathymetry in the Workboat Passage (area between the Yukon main land and Herschel Island) with underlying turbidity calculations from this study during stable E wind conditions. Turbidity is higher in areas of higher depths near Herschel Island than in the center of the Workboat Passage, where depths are smaller. Turbidity at the in- and outflow of the Workboat Passage, where depths up to 10 m are reached, is low compared to the interior of the Workboat Passage. Nautical charts of the Beaufort Sea, Federal publications Inc.

#### 6.4 Comparison to other Modelling Approaches

To assess the accuracy of the results of this study, comparisons to the turbidity model from Nechad et al. (2009), the SPM model from Nechad et al. (2010) and the TSM

model from Tang et al. (2013) were made comparing output from these models and ours, as well as to the results of Doxaran et al. (2012, Figure 26).

The turbidity model from Nechad et al. (2009) uses the remote sensing reflectance (RRS) in the red band. Therefore for this study, RRS in the red band was calculated for all Landsat scenes with stable E wind conditions that were used in this study. The results received a low pass filter over 9x9 cells to eliminate all no data points resulting from the low signal – to – noise ratio over water (Landsat TM and ETM+).

The turbidity dispersal patterns are very similar, since both models use reflectances from the red band (Figure 23). The magnitude of the difference of the highest to lowest values is similar in both images. The two images are well correlated: the ArcMAP calculated correlation coefficient is 0.71 for the whole study area, including areas of high differences, for example in the delta of the Firth River SW of Herschel Island, where the lowpass filter modified the shape of the delta (Figure 23 (b)). The similarity of these two images shows the minor impact of the different atmospheric correction methods (SR and RRS), when calculating mean statistical parameters over a large number of scenes.

The red band SR values were compared to the derived turbidity values from the Nechad et al. (2009) model. The SR value of 550 corresponds to 15 FTU, which can be assigned to nearly clear water (a collection of turbidity formazin standards is given in the Appendix). Nonetheless, the turbidity values are higher in the vicinity of the coast, but rarely exceed 30 FTU (Figure 23, Figure 25). Despite the given error in such models (~ 6 %), this comparison shows low turbidity values along the coast of Herschel Island, although the E-winds transports material from the Mackenzie Delta to the study area. According to this comparison, our model is very sensitive to low turbidity values but should have issues in detecting high values, i.e. in the Mackenzie Delta.

The TSM model developed by Tang et al. (2013) uses two band ratios from the visible spectra: for low values, the ratio of (RRS green / RRS blue) is used and for high values (RRS red / RRS green). The threshold for low to high values is set to ~ 3 g/m<sup>3</sup>, corresponding to the band ratio (RRS red / RRS green) value of 0.6. The SPM model by Nechad *et al.* (2010) runs with either RRS from the red or the NIR band. Both bands received a 5 × 5 lowpass filter to eliminate failed atmospheric corrections. SPM was calculated for Landsat TM scene from September 12, 2011, to compare the results with



the ones from Doxaran et al. (2012), who calculated SPM from a MODIS scene of the same date (Figure 26).

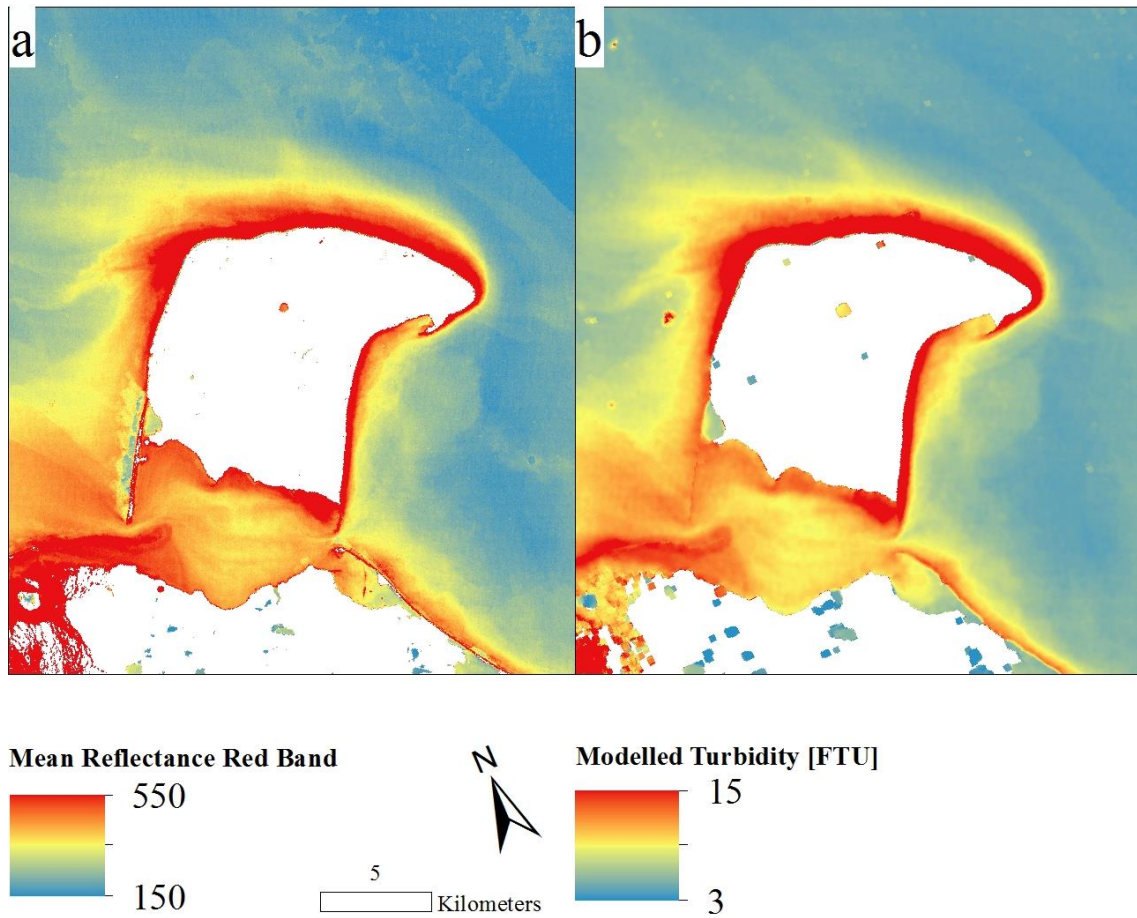


Figure 23: Optical comparison of (a) the mean surface reflectance in the red band derived in this study and (b) the modelled turbidity derived by the model from Nechad et al. (2009) under stable E wind conditions. The turbidity model from Nechad et al. (2009) uses mean remote sensing reflectance in the red band calculated with ACOLITE. Both modelling approaches show similar dispersal patterns. The calculated values in (b) indicate low turbidity values along the coast of Herschel Island in comparison to the ones detected in the Mackenzie Delta area (up to 90 FTU).

TSM results show high values in the vicinity of the coastline ( $> 77 \text{ g/m}^3$ , Figure 27 (a)), with a strong gradient towards very low values in the nearshore zone ( $1\text{-}2 \text{ g/m}^3$ ). These values are lower than calculated SPM values from Doxaran et al. (2012), while TSM values should be higher than SPM values at the same place (chapter 2.2). Calculated TSM values at a stripe extending from Collinson Head SE-wards are also lower than the ones calculated by Doxaran et al. (2012).

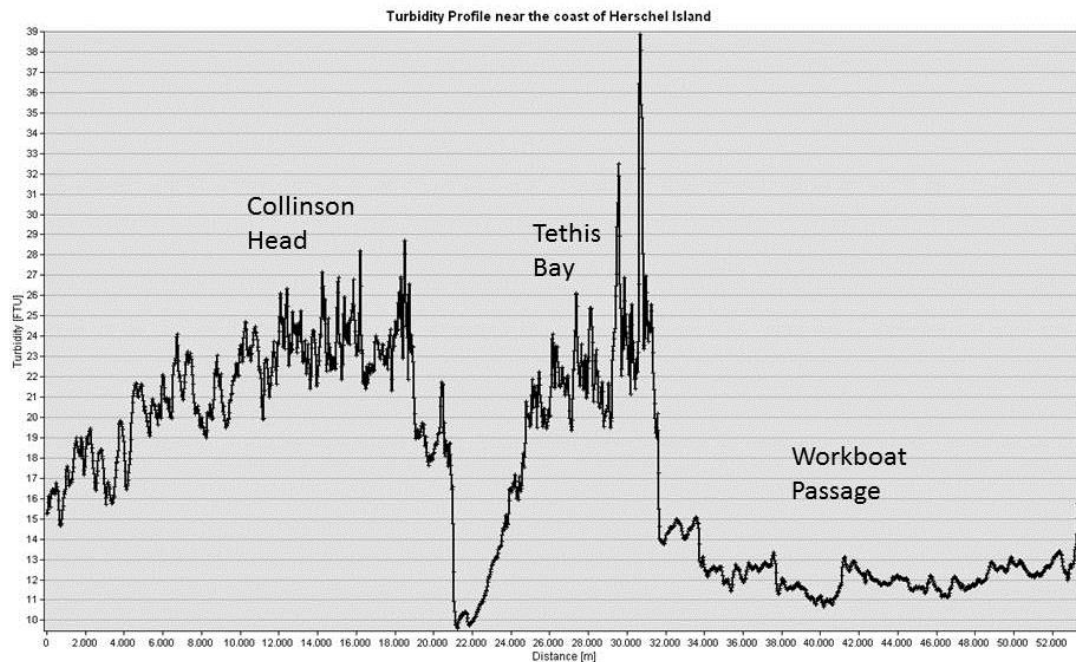


Figure 24: Turbidity profile along the coast of Herschel Island, extracted from the modelled turbidity from Nechad et al. (2009). Turbidity values rarely exceed 30 FTU in the nearshore zone. The transect profile is displayed in Figure 25. Geographical locations are roughly given along the profile. Highest values are present along the NE coast near Collision Head and in Thetis Bay. The area of Pauline Cove is neglected here, because the lowpass filter erased the coastline, so exact drawing of the profile line was not possible (~ 20000 – 24000 m). The highest value (39 FTU; ~ 31000 m) is expected to be a mixed pixel of water and land surface, so the turbidity value might not reflect reality.

SPM calculated from the NIR band shows very high background values of the coast and noisy striping (Figure 27 (b)). This is caused by the high absorption of water in the NIR, where low SPM values cannot be recognized. Near the coast, calculated SPM values are very high, with maximum values  $> 77 \text{ g/m}^3$ . These values have been calculated close to the Mackenzie Delta (Doxaran et al., 2012) and are thus unrealistic at remote areas such as Herschel Island.

SPM calculated from the red band shows much lower background values off the coast than the NIR calculated SPM ( $< 5 \text{ g/m}^3$ , Figure 27 (c)). This corresponds well to the results from Doxaran et al. (2012), who calculated similar SPM values in this area. Additionally, the noise disappeared in the low value areas due to the lower absorption of water in the red wavelengths. Calculated SPM values near the coast of Herschel Island are around  $10 - 30 \text{ g/m}^3$ , with a maximum at the NE coast. High values are also present at a stripe from Collision Head to the SE. Both features were similarly calculated by Doxaran et al. (2012).

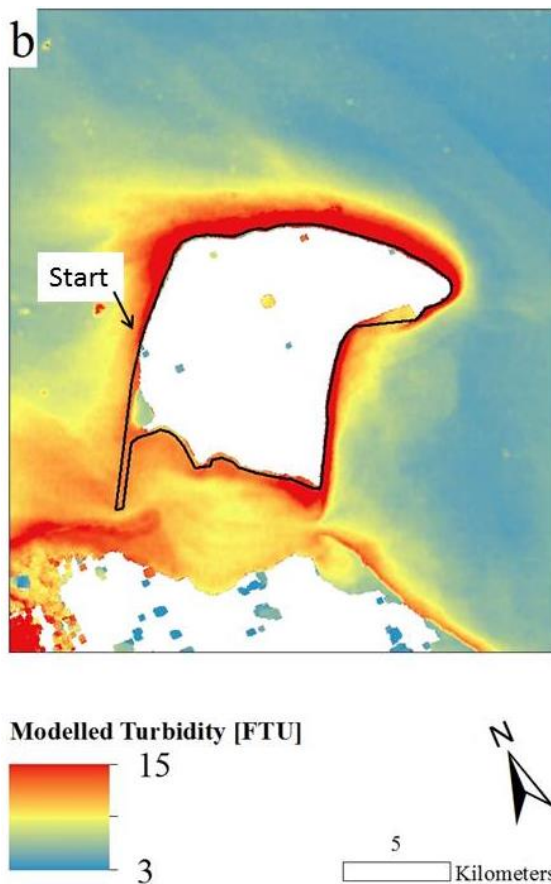


Figure 25: Positioning of the profile line presented in Figure 2Figure 4. The location of the starting point is given at the NW coast. The direction of the profile is northwards. Due to the lowpass filter, the areas around Pauline Cove, Osborn Point and Avadlek Spit are just roughly recognized and should be neglected.

Comparing the calculated values from the nearshore zone of Herschel Island and the Mackenzie Delta gives an idea about the accuracy concerning low SPM, TSM or turbidity values. SPM concentrations from September 12, 2011 east of Collinson Head were compared, where a smaller sediment plume exists, that is even detectable using medium spatial resolution remote sensing, with the maximum values in the delta zone (ignoring the area around the larger cloud, Table 3).

The results from Doxaran et al. (2012, Figure 26) are used here as a cautious reference, because this study used an extensive validation data set collected to the east in the Mackenzie Delta region. Comparing the other three modelling approaches to the results from Doxaran et al. (2012), best agreements are present in the SPM model from Nechad et al. (2010) using red band reflectance values, while the NIR based calculations provide the worst results. The red band based model calculates low and high values similar to Doxaran et al. (2012), while the NIR based model strongly overestimates every value.

The TSM model from Tang et al. (2013) slightly underestimates low values ( $< 10 \text{ g/m}^3$ ) in the nearshore zone compared to Doxaran et al. (2012). High values right close to the coast seem slightly overestimated compared to other TSM modelling approaches (Miller, R.L., McKee, 2004), but not unrealistic. However, general dispersal patterns are similar to Doxaran et al. (2012).

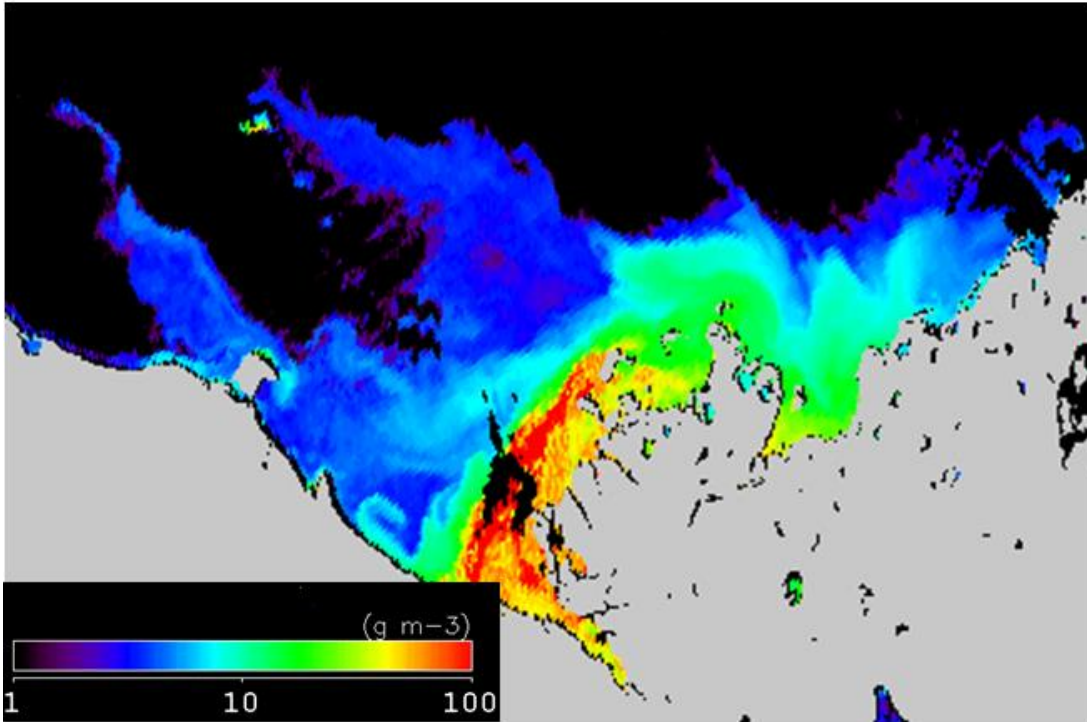
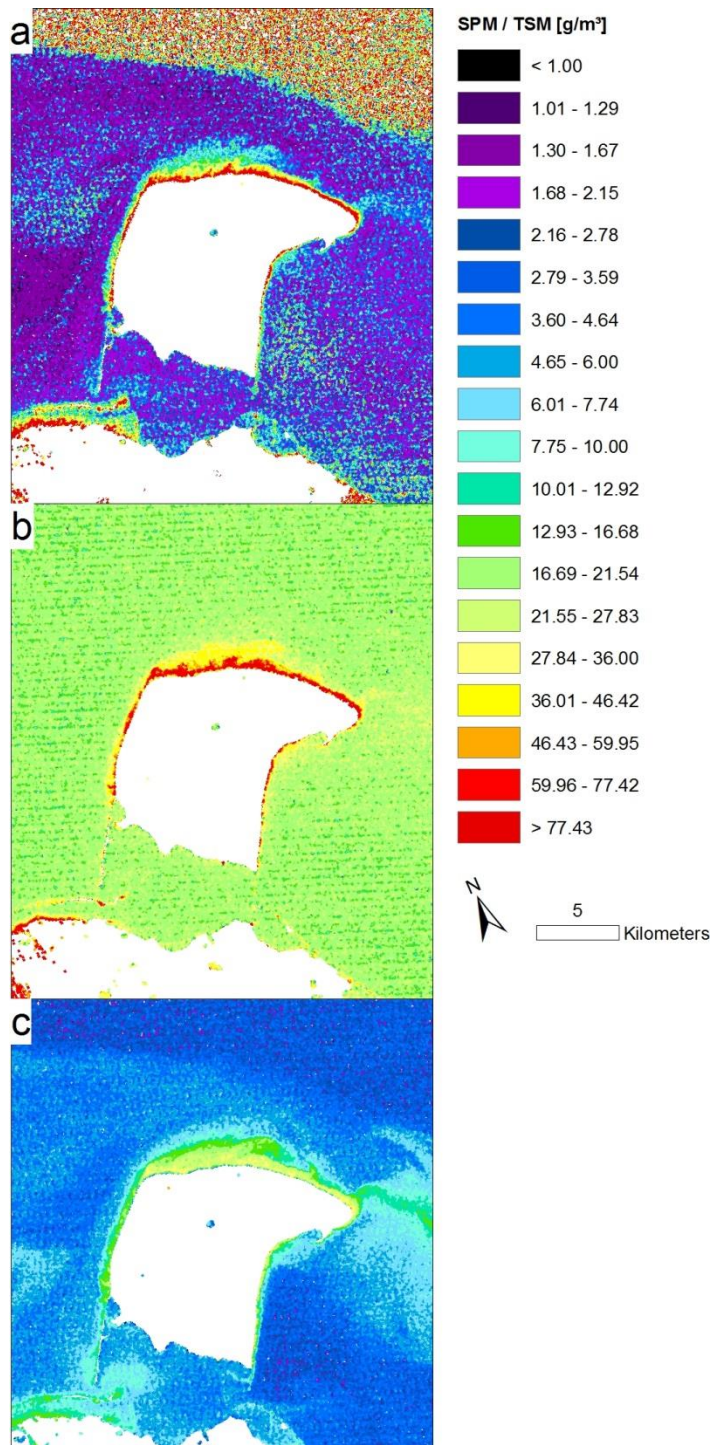


Figure 26: SPM model from MODIS aqua data calculated by Doxaran et al. (2012) at September 12, 2011.

The SPM model from Doxaran et al. (2012) calculates SPM concentrations of  $\sim 8 \text{ g/m}^3$  east of Herschel Island and maximum values values of  $80 - 90 \text{ g/m}^3$  in the delta zone (ratio  $\sim 1/10$ ). The SPM model from Nechad et al. (2010) calculates  $\sim 15 \text{ g/m}^3$  near Collinson Head and  $90 - 100 \text{ g/m}^3$  in the delta zone (ratio  $\sim 1/6$ ). The TSM model from Tang et al. (2013) calculates  $5 - 10 \text{ g/m}^3$  near Collinson Head and up to  $200 \text{ g/m}^3$  in the delta zone (ratio  $\sim 1/25$ ). The turbidity model from Nechad et al. (2009) calculates  $\sim 8$  FTU near Herschel Island and  $\sim 65$  FTU in the delta zone (ratio  $\sim 1/8$ ). The SR in the red band, that was used in this study, has values  $\sim 0.0045 \%$  east of Collinson Head and  $\sim 0.011 \%$  in the delta zone (ratio  $\sim 1/3$ ). The results from this study indicate, that the turbidity, SPM and TSM values in the nearshore zone of Herschel Island are higher than calculated by the models from Nechad et al. (2009, 2010), Doxaran et al. (2012) and Tang et al. (2013). This highlights the importance of specific tuning of SPM models for remote areas like Herschel Island. The sedimentation environment there differs significantly from the Mackenzie Delta, where validation datasets have been collected in the past.



Comparing these modelling results to the ones of this study provides an approximation for expected values regarding surface reflectance only. Turbidity values rarely exceed 30 FTU with the majority below 25 FTU. The surface reflectance value (red band) of 550 roughly corresponds to 15 FTU. SPM values in the coastal and nearshore zone range between 10 and 30  $\text{g}/\text{m}^3$ .

Figure 27: Comparison of the Landsat scene taken on September 12, 2011 with values calculated using (a) the TSM model from Tang et al. (2013), and the SPM models from Nechad et al. (2010) using (b) NIR and (c) red band reflectances. Values are displayed in a logarithmic scale. All three modelling approaches show similar dispersal patterns compared to Doxaran et al. (2012). (a) shows a wider range of values compared to Doxaran et al. (2012), while (b) overestimated all values. (c) gives the best approach to the given data.

|                 | Doxaran et al.<br>(2012, [g/m <sup>3</sup> ]) | Nechad et al.<br>(2010, [g/m <sup>3</sup> ]) | Tang et al.<br>(2013, [g/m <sup>3</sup> ]) | Nechad et al.<br>(2009, [FTU]) | <b>This study [%]</b> |
|-----------------|---|--|--|--------------------------------|-----------------------|
| Herschel Island | 8   | 15   | 5 - 10                                     | 8                              | <b>0.004</b>          |
| Mackenzie Delta | 80 - 90                                       | 90 - 100                                     | 200  | 65                             | <b>0.011</b>          |
| Ratio           | ~ 1/10  | ~ 1/6  | ~ 1/25                                     | ~ 1/8                          | ~ <b>1/3</b>          |

Table 3: Comparing modelled output values from different models and this study in the nearshore zone of Herschel Island (east of Collinson Head) and the Mackenzie Delta. Mentioned models are (from left to right): SPM model from Doxaran et al. (2012), SPM model from Nechad et al. (2010), TSM model from Tang et al. (2013), turbidity model from Nechad et al. (2009) and surface reflectance values from this study. The lower ratio (Herschel Island / Mackenzie Delta) of the 4 considered models compared to this study indicates higher values in the nearshore zone of Herschel Island than previously calculated.

## 6.5 Applicability of spatial data

The substantial advantages of using Landsat satellite imagery are the high spatial resolution and the long time series of comparable data (since 1983). This allows (i) the investigation of small scale hydrodynamic features along the coast of small islands such as Herschel Island and (ii) the comparison of data over more than three decades.

Since Satellites such as Sentinel 2 were launched, (i) is not relevant anymore; multispectral sensors with high spatial resolution are common and used widely for coastal research (Topouzelis et al., 2016). For example, Sentinel 2 has more bands available in the range from deep blue to SWIR than Landsat 8 with spatial resolutions up to 10 m (Drusch et al., 2012). One considerable advantage of Landsat is still the TIR channel.

The disadvantages of Landsat satellite imagery are the low temporal and radiometric resolution. While the temporal resolution correlates negatively to the spatial resolution (Hilker et al., 2009), the radiometric resolution could have been adjusted. For example, AVHRR, started in 1978, has a radiometric resolution of 10 bit (compared to 8 bit of Landsat TM) and is thus more suitable for ocean color remote sensing. However, Landsat was designed for land surface applications, where the higher radiometric resolution was not needed.

The USGS - provided cf-mask for distinguishing different surfaces (land, water, ice, clouds and cloud shadows) is a very useful tool for applications presented here. However, this algorithm has a certain amount of uncertainty (~ 10 %), that might occur due to missing test areas and unique environments (Foga et al., 2017, Figure 28). The

USGS itself reports issues in classifying bright surfaces such as sandy beaches. In this study, the cf-mask algorithm had major problems in detecting small land or water features, such as Avadlek Spit and Pauline Cove. While these Problems only occur in distinguishing land from water surfaces, the usage of threshold values in the NIR and SWIR band could be considered (Pushparaj and Hegde, 2017).

The use of ‘marine’ sensors such as MODIS would provide more suitable data for ocean color remote sensing with much higher temporal resolution (~ 1 day, Heim et al., 2014). However, spatial resolution in the Arctic is reduced to 1 km, making this sensor irrelevant for investigations of coastal and nearshore waters around small islands, where to many details tend to disappear (Doxaran et al., 2012).

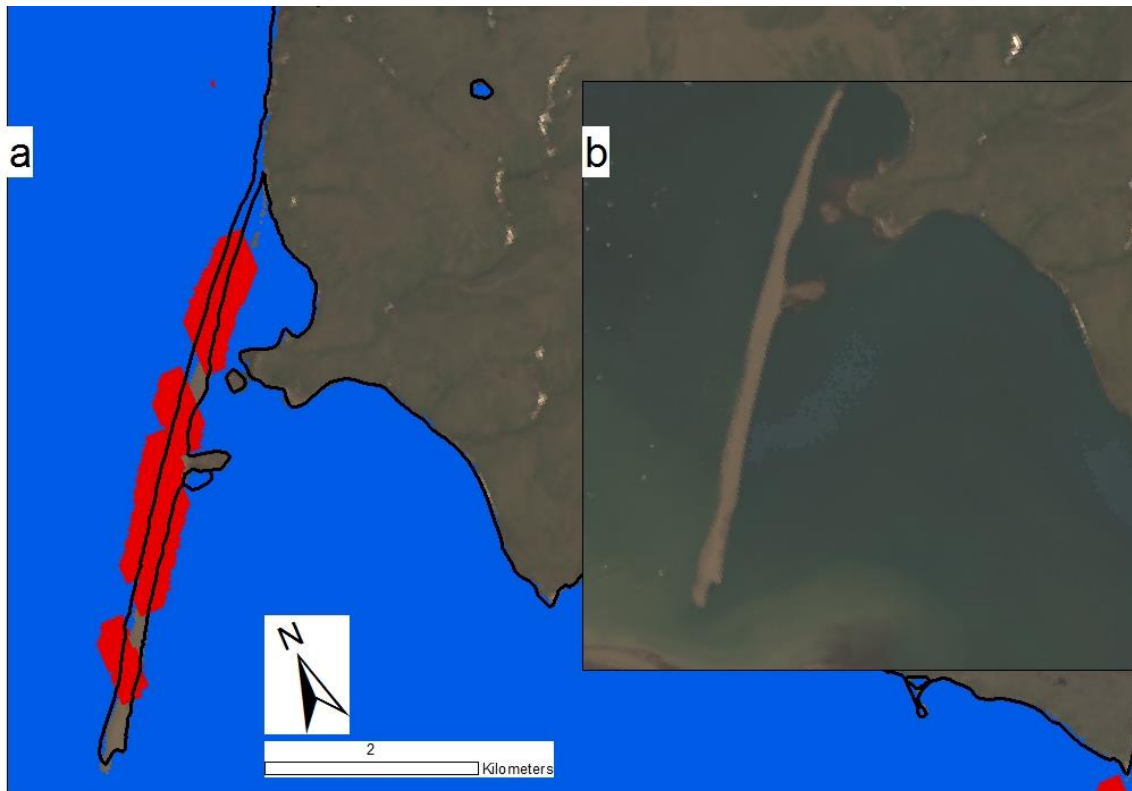


Figure 28: Example for the difficulties associated with using the USGS provided cf-mask from Landsat 8 Scene taken on July 15, 2015. (a): Applied cf-mask. Land area is transparent, water area blue and clouds red. The shoreline of Herschel Island is drawn in black. (b): True color image of the same scene and location as (a). Difficulties in detecting the water surfaces are clearly visible.

## 6.6 Outlook

---

The planned collection of *in-situ* data during the field campaign 2017 will allow the construction of an own model for turbidity, SPM and/or TSM, that is specifically tuned for the study area. Most existing models are (i) either designed for global usage (Nechad et al., 2009, 2010) or (ii) ‘contaminated’ by regional high values such as the Mackenzie River Plume (Doxaran et al., 2012; Tang et al., 2013). While (i) results in a non-specific tuning of the models, which likely will not display regional characteristics, (ii) may result in a non-realistic representation of low to medium scale values, because the focusses of such models are often high values.

The results of this Master’s thesis provide sufficient data for an improved understanding of sediment transport pathways in the southern Canadian Beaufort Sea. The impact of the Mackenzie River Plume on the sediment supply in the coastal and nearshore zone of Herschel Island is clearly shown. The bimodal wind pattern in southern Beaufort Sea has major impact on the sediment distribution at the Canadian Beaufort Shelf and hence the coastal area of Herschel Island.

Together with specially tuned models for the studied area, sediment budget could be calculated, including coastal erosion and Mackenzie River Plume input. Seasonal changes, such as the Mackenzie River discharge change, wind direction change and storm activity, can be considered. The turbidity models can be used to calculate sediment dispersal and hence the transport of organic compounds around the whole island and potentially contribute to updated nearshore carbon budget for the whole region.



## 7 Conclusion

---

The aim of this Master's thesis was to identify sediment pathways in the coastal and nearshore zone of Herschel Island. Therefore, 30 years of Landsat satellite imagery were analyzed under seasonal changing metrological forcing with a focus on turbidity and SST. Due to the lack of *in-situ* measurements, proxies have been used for both values (mean reflectance in the red band and at-sensor (uncorrected) temperature, respectively), resulting in a qualitative overview on nearshore transportation patterns in the study area.

The presented results show clear differences of both observed parameters during the two prevailing wind conditions (E and NW). During E wind conditions, turbidity and SST values showed significantly higher values in the nearshore zone, which can be interpreted as the influence on the Mackenzie River Plume. However, a comparison of the modelled turbidity proxy values with a globally tuned turbidity model from Nechad *et al.* (2009) shows still very low values: turbidity around the coast of Herschel Island rarely exceeds 30 FTU. Turbidity values around Herschel Island from this study are, relative to the Mackenzie Delta, higher than in other modelling approaches, indicating higher SPM concentrations in the nearshore zone of Herschel Island than previously thought and modelled (Doxaran *et al.*, 2012; Nechad *et al.*, 2009, 2010; Tang *et al.*, 2013).

The strong gradient of turbidity from the nearshore to the offshore zone under both wind conditions indicates an accumulation of eroded and transported material near the coast. Only small parts of it get transported offshore. However, tracing material far away from the coast gets difficult with satellite remote sensing, due to the limited penetration depth of light in water.

Turbidity is not only caused by transported suspended sediment from the Mackenzie River, but also by resuspension due to longshore currents or upwelling. While longshore currents likely have a big influence on turbidity along the Yukon coast, resulting in high turbidity in the Workboat Passage, upwelling takes place in areas of high turbidity and low SST. A main upwelling region was identified in the NW of Herschel Island during E wind conditions, where SST is significantly lower than at the SE coast of Herschel Island, while turbidity values are similar.

To improve the results of this study, *in-situ* measurements from the study area are needed to calibrate a model especially to the southern Beaufort Sea and the nearshore zone of Herschel Island. This data is planned to obtain during summer field season 2017. After the analysis of these samples, more exact values of turbidity, SST and SPM concentration can be calculated with the modelled data.

In order to achieve a wider understanding of sedimentation processes in the nearshore zone of Herschel Island, sedimentation and coastal erosion data should be taken into account regarding further studies. Therefore, the usage of higher temporal resolution spectral data should be considered.

## References

---

- Arrigo, K.R., van Dijken, G., and Pabi, S., 2008, Impact of a shrinking Arctic ice cover on marine primary production: *Geophysical Research Letters*, v. 35, p. 1–6, doi: 10.1029/2008GL035028.
- Bailard, J.A., 1982, Modeling On-Offshore Sediment Transport in the Surfzone: *Coastal Engineering*, p. 1419–1438, doi: 10.1061/9780872623736.087.
- Barker, T., 2007, Climate Change 2007 : An Assessment of the Intergovernmental Panel on Climate Change: *Change*, v. 446, p. 12–17, doi: 10.1256/004316502320517344.
- Bloesch, J., 1982, Inshore-Offshore Sedimentation Differences Resulting from Resuspension in the Eastern Basin of Lake Erie": *Can. J. Fish. Aquat. Sci.*, v. 39, p. 748–759.
- Brenon, I., and Hir, P. Le, 1999, Modelling the Turbidity Maximum in the Seine Estuary ( France ): Identification of Formation Processes: *Estuarine, Coastal and Shelf Science*, v. 49, p. 525–544, doi: 10.1006/ecss.1999.0514.
- Brigham-Grette, J., and Carter, L.D., 1992, Pliocene marine transgressions of northern Alaska: circumarctic correlations and paleoclimatic interpretations: *Arctic*, v. 45, p. 74–89.
- Burn, C.R., and Hattendorf, J.B., 2011, Toponymy of Herschel Island ( Qikiqtaryuk ), Western Arctic Coast , Canada: *Arctic*, v. 64, p. 459–464.
- Burn, C.R., and Zhang, Y., 2009, Permafrost and climate change at Herschel Island ( Qikiqtaruq ), Yukon Territory , Canada: *Journal of Geophysical research*, v. 114, p. 1–16, doi: 10.1029/2008JF001087.
- Bustamante, J., Pacios, F., Díaz-Delgado, R., and Aragonés, D., 2009, Predictive models of turbidity and water depth in the Doñana marshes using Landsat TM and ETM+ images: *Journal of Environmental Management*, v. 90, p. 2219–2225, doi: 10.1016/j.jenvman.2007.08.021.
- Carmack, E., and Wassmann, P., 2006, Food webs and physical-biological coupling on pan-Arctic shelves: Unifying concepts and comprehensive perspectives: *Progress in Oceanography*, v. 71, p. 446–477, doi: 10.1016/j.pocean.2006.10.004.
- Carson, M.A., Jasper, J.N., and Conly, P.M., 1998, Magnitude and sources of sediment input to the Mackenzie Delta, Northwest Territories, 1974-94: *Arctic*, v. 51, p. 116–124.
- Comiso, J.C., and Hall, D.K., 2014, Climate trends in the Arctic as observed from space: *Wiley Interdisciplinary Reviews: Climate Change*, v. 5, p. 389–409, doi: 10.1002/wcc.277.

- Couture, N.J., 2010, Fluxes of Soil Organic Carbon from eroding Permafrost Coasts, Canadian Beaufort Sea. Retrieved from eScholarship\_McGill (000026878). Montreal, QC: McGill University
- Dittmar, T., and Kattner, G., 2003, The biogeochemistry of the river and shelf ecosystem of the Arctic Ocean: a review: *Marine Chemistry*, v. 83, p. 103–120, doi: 10.1016/S0304-4203(03)00105-1.
- Dixon, R.K., Solomon, A.M., Brown, S., Houghton, R.A., Trexler, M.C., and Wisniewski, J., 1994, Carbon Pools and Flux of Global Forest Ecosystems: *Science*, v. 263, p. 185–190, doi: 10.1126/science.263.5144.185.
- Doerffer, R., Fischer, J., Stössel, M., Brockmann, C., and Grassl, H., 1989, Analysis of thematic mapper data for studying the suspended matter distribution in the coastal area of the German Bight (North Sea): *Remote Sensing of Environment*, v. 28, p. 61–73, doi: 10.1016/0034-4257(89)90105-3.
- Dogliotti, A.I., Ruddick, K.G., Nechad, B., Doxaran, D., and Knaeps, E., 2015, A single algorithm to retrieve turbidity from remotely-sensed data in all coastal and estuarine waters: *Remote Sensing of Environment*, v. 156, p. 157–168, doi: 10.1016/j.rse.2014.09.020.
- Doxaran, D., Devred, E., and Babin, M., 2015, A 50 % increase in the mass of terrestrial particles delivered by the Mackenzie River into the Beaufort Sea (Canadian Arctic Ocean) over the last 10 years: *Biogeosciences*, v. 12, p. 3551–3565, doi: 10.5194/bg-12-3551-2015.
- Doxaran, D., Ehn, J., Bélanger, S., Matsuoka, A., Hooker, S., and Babin, M., 2012, Optical characterisation of suspended particles in the Mackenzie River plume (Canadian Arctic Ocean) and implications for ocean colour remote sensing: *Biogeosciences*, v. 9, p. 3213–3229, doi: 10.5194/bg-9-3213-2012.
- Drusch, M., Del Bello, U., Carlier, S., Colin, O., Fernandez, V., Gascon, F., Hoersch, B., Isola, C., Laberinti, P., Martimort, P., Meygret, A., Spoto, F., Sy, O., Marchese, F., et al., 2012, Sentinel-2: ESA's Optical High-Resolution Mission for GMES Operational Services: *Remote Sensing of Environment*, v. 120, p. 25–36, doi: 10.1016/j.rse.2011.11.026.
- Dunton, K.H., Weingartner, T., and Carmack, E.C., 2006, The nearshore western Beaufort Sea ecosystem: Circulation and importance of terrestrial carbon in arctic coastal food webs: *Progress in Oceanography*, v. 71, p. 362–378, doi: 10.1016/j.pocean.2006.09.011.
- Dyke, A.S., and Prest, V.K., 1987, Late Wisconsinan and Holocene History of the Laurentide Ice Sheet: *Géographie physique et Quaternaire*, v. 41, p. 237, doi: 10.7202/032681ar.
- Federal Publications Inc., Nautical Charts of the Beaufort Sea, 1998 – 2016.

- Fichot, C.G., Kaiser, K., Hooker, S.B., Amon, R.M.W., Babin, M., Bélanger, S., Walker, S.A., and Benner, R., 2013, Pan-Arctic distributions of continental runoff in the Arctic Ocean: *Scientific Reports*, v. 3, p. 1053, doi: 10.1038/srep01053.
- Fissel, D. B., & Birch, J.R., 1984, *Sediment Transport in the Canadian Beaufort Sea*: Arctic Sciences Limited,.
- Foga, S., Scaramuzza, P.L., Guo, S., Zhu, Z., Dilley, R.D., Beckmann, T., Schmidt, G.L., Dwyer, J.L., Joseph Hughes, M., and Laue, B., 2017, Cloud detection algorithm comparison and validation for operational Landsat data products: *Remote Sensing of Environment*, v. 194, p. 379–390, doi: 10.1016/j.rse.2017.03.026.
- Fossheim, M., Primicerio, R., Johannesen, E., Ingvaldsen, R.B., Aschan, M.M., and Dolgov, A. V., 2015, Recent warming leads to a rapid borealization of fish communities in the Arctic: *Nature Climate Change*, v. 5, p. 673–677, doi: 10.1038/nclimate2647.
- Fritz, M., Vonk, J.E., and Lantuit, H., 2017, Collapsing Arctic coastlines: *Nature Climate Change*, v. 7, p. 6–7, doi: 10.1038/nclimate3188.
- Fritz, M., Wetterich, S., Schirrmeister, L., Meyer, H., Lantuit, H., Preusser, F., and Pollard, W.H., 2012, Eastern Beringia and beyond: Late Wisconsinan and Holocene landscape dynamics along the Yukon Coastal Plain, Canada: *Palaeogeography, Palaeoclimatology, Palaeoecology*, v. 319–320, p. 28–45, doi: 10.1016/j.palaeo.2011.12.015.
- Giovando, L.F., and Herlinveaux, R.H., 1981, a Discussion of Factors Influencing Dispersion of Pollutants in the Beaufort Sea: *Pacific Marine Science report*, v. 81.
- Gordeev, V. V., 2006, Fluvial sediment flux to the Arctic Ocean: *Geomorphology*, v. 80, p. 94–104, doi: 10.1016/j.geomorph.2005.09.008.
- Günther, F., Overduin, P.P., Sandakov, A. V., Grosse, G., and Grigoriev, M.N., 2013, Short- and long-term thermo-erosion of ice-rich permafrost coasts in the Laptev Sea region: *Biogeosciences*, v. 10, p. 4297–4318, doi: 10.5194/bg-10-4297-2013.
- Hansen, J., Ruedy, R., Sato, M., and Lo, K., 2010, Global surface temperature change: *Rev. Geophys.*, v. 48, p. RG4004, doi: 10.1029/2010RG000345.
- Heim, B., Abramova, E., Doerffer, R., Günther, F., Hölemann, J., Kraberg, A., Lantuit, H., Loginova, A., Martynov, F., Overduin, P.P., and Wegner, C., 2014, Ocean colour remote sensing in the southern laptev sea: Evaluation and applications: *Biogeosciences*, v. 11, p. 4191–4210, doi: 10.5194/bg-11-4191-2014.
- Héquette, A., and Hill, P.R., 1993, Storm-generated currents and offshore sediment transport on a sandy shoreface, Tibjak Beach, Canadian Beaufort Sea: *Marine Geology*, v. 113, p. 283–304.

- Hilker, T., Wulder, M.A., Coops, N.C., Linke, J., McDermid, G., Masek, J.G., Gao, F., and White, J.C., 2009, A new data fusion model for high spatial- and temporal-resolution mapping of forest disturbance based on Landsat and MODIS: *Remote Sensing of Environment*, v. 113, p. 1613–1627, doi: 10.1016/j.rse.2009.03.007.
- Hill, P. R., & Nadeau, O.C., 1989, Storm-dominated sedimentation on the inner shelf of the Canadian Beaufort Sea: *Journal of Sedimentary Research*, v. 59.
- Hill, P.R., Blasco, S.M., Harper, J.R., and Fissel, D.B., 1991, Sedimentation on the Canadian Beaufort Shelf: *Continental Shelf Research*, v. 11, p. 821–842, doi: 10.1016/0278-4343(91)90081-G.
- Hjulström, F., 1939, Transportation of detritus by moving water, *in* SP 10: *Recent Marine Sediments*, p. 5–31.
- Holland, M.M., and Bitz, C.M., 2003, Polar amplification of climate change in coupled models: *Climate Dynamics*, v. 21, p. 221–232, doi: 10.1007/s00382-003-0332-6.
- Holmes, R.M., McClelland, J.W., Peterson, B.J., Shiklomanov, I.A., Shiklomanov, A.I., Zhulidov, A. V., Gordeev, V. V., and Bobrovitskaya, N.N., 2002, A circumpolar perspective on fluvial sediment flux to the Arctic ocean: *Global Biogeochemical Cycles*, v. 16, p. 45-1-45–14, doi: 10.1029/2001GB001849.
- Hugelius, G., Strauss, J., Zubrzycki, S., Harden, J.W., Schuur, E.A.G., Ping, C., and Schirmermeister, L., 2014, Estimated stocks of circumpolar permafrost carbon with quantified: *Biogeoscience*, v. 11, p. 6573–6593, doi: 10.5194/bg-11-6573-2014.
- Hussain, I., Ahamad, K., and Nath, P., 2016, Water turbidity sensing using a smartphone: *RSC Advances*, v. 6, p. 22374–22382, doi: 10.1039/C6RA02483A.
- IPCC, 2013: *Climate Change 2013: The Physical Science Basis. Contribution of Working Group I to the Fifth Assessment Report of the Intergovernmental Panel on Climate Change* [Stocker, T.F., D. Qin, G.-K. Plattner, M. Tignor, S.K. Allen, J. Boschung, A. Nauels, Y. Xia, V. Bex and P.M. Midgley (eds.)]. Cambridge University Press, Cambridge, United Kingdom and New York, NY, USA, 1535 pp.
- Cover Jerosch, K., 2013, Geostatistical mapping and spatial variability of surficial sediment types on the Beaufort Shelf based on grain size data: *Journal of Marine Systems*, v. 127, p. 5–13, doi: 10.1016/j.jmarsys.2012.02.013.
- Jones, B.M., Arp, C.D., Jorgenson, M.T., Hinkel, K.M., Schmutz, J.A., and Flint, P.L., 2009, Increase in the rate and uniformity of coastline erosion in Arctic Alaska: *Geophysical Research Letters*, v. 36, p. 1–5, doi: 10.1029/2008GL036205.

- Klein, E.S., Nolan, M., McConnell, J., Sigl, M., Cherry, J., Young, J., and Welker, J.M., 2016, McCall Glacier record of Arctic climate change: Interpreting a northern Alaska ice core with regional water isotopes: *Quaternary Science Reviews*, v. 131, p. 274–284, doi: 10.1016/j.quascirev.2015.07.030.
- Lantuit, H., and Pollard, W.H., 2008, Fifty years of coastal erosion and retrogressive thaw slump activity on Herschel Island, southern Beaufort Sea, Yukon Territory, Canada: *Geomorphology*, v. 95, p. 84–102, doi: 10.1016/j.geomorph.2006.07.040.
- Lantuit, H., Overduin, P.P., Couture, N., Wetterich, S., Aré, F., Atkinson, D., Brown, J., Cherkashov, G., Drozdov, D., Donald Forbes, L., Graves-Gaylord, A., Grigoriev, M., Hubberten, H.W., Jordan, J., et al., 2012, The Arctic Coastal Dynamics Database: A New Classification Scheme and Statistics on Arctic Permafrost Coastlines: *Estuaries and Coasts*, v. 35, p. 383–400, doi: 10.1007/s12237-010-9362-6.
- Macdonald, R.W., Paten, D.W., and Carmack, E.C., 1995, Measurements in Water: *Journal of Geophysical research*, v. 100, p. 895–919.
- MacFarlane, N., and Robinson, I.S., 1984, Atmospheric correction of LANDSAT MSS data for a multirate suspended sediment algorithm: *International Journal of Remote Sensing*, v. 5, p. 561–576, doi: 10.1080/01431168408948837.
- Mackay, J.R., 1971, The Origin of Massive Icy Beds in Permafrost, Western Arctic Coast, Canada: *Canadian Journal of Earth Sciences*, v. 8.
- Manabe, S. and Stouffer, J., 1980, Sensitivity of a Global Climate Model to an Increase of CO<sub>2</sub> Concentration in the Atmosphere: *Journal of Geophysical research*, v. 85, p. 5529–5554.
- Mannino, A., Novak, M.G., Hooker, S.B., Hyde, K., and Aurin, D., 2014, Algorithm development and validation of CDOM properties for estuarine and continental shelf waters along the northeastern U.S. coast: *Remote Sensing of Environment*, v. 152, p. 576–602, doi: 10.1016/j.rse.2014.06.027.
- Masek, J.G., Vermote, E.F., Saleous, N.E., Wolfe, R., Hall, F.G., Huemmrich, K.F., Gao, F., Kutler, J., and Lim, T.K., 2006, A landsat surface reflectance dataset for North America, 1990-2000: *IEEE Geoscience and Remote Sensing Letters*, v. 3, p. 68–72, doi: 10.1109/LGRS.2005.857030.
- McClelland, J.W., Déry, S.J., Peterson, B.J., Holmes, R.M., and Wood, E.F., 2006, A pan-arctic evaluation of changes in river discharge during the latter half of the 20th century: *Geophysical Research Letters*, v. 33, p. 2–5, doi: 10.1029/2006GL025753.
- Miller, R.L., McKee, B.A., 2004, Using MODIS Terra 250 m Imagery to Map Concentrations of Total Suspended Matter in Coastal Waters: *Remote Sensing of Environment*, v. 93, p. 259–266.

- Mulligan, R.P., Perrie, W., and Solomon, S., 2010, Dynamics of the Mackenzie River plume on the inner Beaufort shelf during an open water period in summer: *Estuarine, Coastal and Shelf Science*, v. 89, p. 214–220, doi: 10.1016/j.ecss.2010.06.010.
- Nazeer, M., Nichol, J.E., and Yung, Y.-K., 2014, Evaluation of atmospheric correction models and Landsat surface reflectance product in an urban coastal environment: *International Journal of Remote Sensing*, v. 35, p. 6271–6291, doi: 10.1080/01431161.2014.951742.
- Nechad, B., Ruddick, K.G., and Neukermans, G., 2009, Calibration and validation of a generic multisensor algorithm for mapping of turbidity in coastal waters: *Remote Sensing of the Ocean, Sea Ice, and Large Water Regions*, v. Conference, p. 74730H, doi: 10.1117/12.830700.
- Nechad, B., Ruddick, K.G., and Park, Y., 2010, Calibration and validation of a generic multisensor algorithm for mapping of total suspended matter in turbid waters: *Remote Sensing of Environment*, v. 114, p. 854–866, doi: 10.1016/j.rse.2009.11.022.
- O'Brien, M.C., Macdonald, R.W., Melling, H., and Iseki, K., 2006, Particle fluxes and geochemistry on the Canadian Beaufort Shelf: Implications for sediment transport and deposition: *Continental Shelf Research*, v. 26, p. 41–81, doi: 10.1016/j.csr.2005.09.007.
- Pelletier, B.R., 1975, *Sediment Dispersal in the Southern Beaufort Sea.*
- Pelletier, B.R., Bornhold, B.D., Buckley, D.E., Costaschuk, S., Forbes, D.L., Lewis, C.F.M., Lewis, C.P., Matsumoto, E., Meagher, L., Walker, D.A., and Wong, S.C., 1984, *Marine Science Atlas Of The Beaufort Sea - Sediments*: 62 p.
- Peterson, B.J., 2006, Trajectory Shifts in the Arctic and Subarctic Freshwater Cycle: *Science*, v. 313, p. 1061–1066, doi: 10.1126/science.1122593.
- Pfalz, G., 2017, Lateral transport of sediment and organic matter, derived from coastal erosion, into the nearshore zone of the southern Beaufort Sea, Canada: *Technische Universität Dresden*, 86 p.
- Pushparaj, J., and Hegde, A.V., 2017, Estimation of bathymetry along the coast of Mangaluru using Landsat-8 imagery: *The International Journal of Ocean and Climate Systems*, p. 1–13, doi: 10.1177/1759313116679672.
- Radosavljevic, B., Lantuit, H., Pollard, W., Overduin, P., Couture, N., Sachs, T., Helm, V., and Fritz, M., 2015, Erosion and Flooding—Threats to Coastal Infrastructure in the Arctic: A Case Study from Herschel Island, Yukon Territory, Canada: *Estuaries and Coasts*, v. 39, p. 900–915, doi: 10.1007/s12237-015-0046-0.



- Raynolds, M.K., Walker, D.A., Ambrosius, K.J., Brown, J., Everett, K.R., Kanevskiy, M., Kofinas, G.P., Romanovsky, V.E., Shur, Y., and Webber, P.J., 2014, Cumulative geocological effects of 62 years of infrastructure and climate change in ice-rich permafrost landscapes, Prudhoe Bay Oilfield, Alaska: *Global Change Biology*, v. 20, p. 1211–1224, doi: 10.1111/gcb.12500.
- Ritchie, J.C., Cooper, C.M., and Schiebe, F.R., 1990, The relationship of MSS and TM digital data with suspended sediments, chlorophyll, and temperature in Moon Lake, Mississippi: *Remote Sensing of Environment*, v. 33, p. 137–148, doi: 10.1016/0034-4257(90)90039-O.
- Romanovsky, V.E., Smith, S.L., and Christiansen, H.H., 2010, Permafrost thermal state in the polar northern hemisphere during the international polar year 2007-2009: A synthesis: *Permafrost and Periglacial Processes*, v. 21, p. 106–116, doi: 10.1002/ppp.689.
- Ruddick, K., Park, Y., and Nechad, B., 2004, Meris imagery of belgian coastal waters: Mapping of suspended particulate matter and chlorophyll-A: European Space Agency, (Special Publication) ESA SP, p. 217–226.
- Scudder, G.G.E., 1997, Environment of the Yukon, *in* Danks, H.V. and Downes, H.A. ed., *Insects of the Yukon*, Ottawa, Biological Survey of Canada, p. 13–57, <http://scholar.google.com/scholar?hl=en&btnG=Search&q=intitle:Environment+of+the+Yukon#0>.
- Serreze, M.C., Holland, M.M., and Stroeve, J., 2007, Perspectives on the Arctic's Shrinking Sea-Ice Cover: *Science*, v. 315, p. 1533–1536, doi: 10.1126/science.1139426.
- Simpson, J.H., and Brown, J., 1987, The interpretation of visible band imagery of turbid shallow seas in terms of the distribution of suspended particulates: *Continental Shelf Research*, v. 7, p. 1307–1313, doi: 10.1016/0278-4343(87)90034-3.
- Solomon, S.M., 2005, Spatial and temporal variability of shoreline change in the Beaufort-Mackenzie region, northwest territories, Canada: *Geo-Marine Letters*, v. 25, p. 127–137, doi: 10.1007/s00367-004-0194-x.
- Stein, R., and MacDonald, R.W., 2014, *The Organic Carbon Cycle in the Arctic Ocean* (R. Stein & R. W. Macdonald, Eds.): Springer-Verlag Berlin Heidelberg, 363 p., doi: 10.1007/978-3-642-18912-8.
- Stirling, I.A.N., and Parkinson, C.L., 2006, Possible Effects of Climate Warming on Selected Populations of Polar Bears ( *Ursus maritimus* ) in the Canadian Arctic: v. 59, p. 261–275.
- Storey, J., Scaramuzza, P., Schmidt, G., and Barsi, J., 2005, Landsat 7 Scan Line Corrector-Off Gap-Filled Product Gap-Filled Product Development Process, *in* *Global Priorities in Land Remote Sensing*,.

Syvitski, J.P.M., 2002, Sediment discharge variability in Arctic rivers: Implications for a warmer future: *Polar Research*, v. 21, p. 323–330, doi: 10.3402/polar.v21i2.6494.

Tang, S., Larouche, P., Niemi, A., and Michel, C., 2013, Regional algorithms for remote-sensing estimates of total suspended matter in the Beaufort Sea: *International Journal of Remote Sensing*, v. 34, p. 6562–6576, doi: 10.1080/01431161.2013.804222.

- Tanré, D., Kaufman, Y.J., Herman, M., and Mattoo, S., 1997, Remote sensing of aerosol properties over oceans using the MODIS/EOS spectral radiances: *Journal of Geophysical Research: Atmospheres*, v. 102, p. 16971–16988, doi: 10.1029/96JD03437.
- Tanski, G., Lantuit, H., Ruttor, S., Knoblauch, C., Radosavljevic, B., Strauss, J., Wolter, J., Irrgang, A.M., Ramage, J., and Fritz, M., 2017, Transformation of terrestrial organic matter along thermokarst-affected permafrost coasts in the Arctic: *Science of the Total Environment*, v. 581–582, p. 434–447, doi: 10.1016/j.scitotenv.2016.12.152.
- Thomson, J., and Rogers, W.E., 2014, Swell and sea in the emerging Arctic Ocean: *Geophysical Research Letters*, v. 41, p. 3136–3140, doi: 10.1002/2014GL059983.
- Topouzelis, K., Charalampis Spondylidis, S., Papakonstantinou, A., and Soulakellis, N., 2016, The use of Sentinel-2 imagery for seagrass mapping: Kalloni Gulf (Lesvos Island, Greece) case study, *in* Fourth International Conference on Remote Sensing and Geoinformation of the Environment, doi: 10.1117/12.2242887.
- US Geological Survey, 2016, Landsat—Earth observation satellites (ver. 1.1, August 2016): U.S. Geological Survey Fact Sheet 2015–3081:, doi: 10.3133/fs20153081.
- Van Vliet, M.T.H., Franssen, W.H.P., Yearsley, J.R., Ludwig, F., Haddeland, I., Lettenmaier, D.P., and Kabat, P., 2013, Global river discharge and water temperature under climate change: *Global Environmental Change*, v. 23, p. 450–464, doi: 10.1016/j.gloenvcha.2012.11.002.
- Vanhellemont, Q., and Ruddick, K., 2014, Turbid wakes associated with offshore wind turbines observed with Landsat 8: *Remote Sensing of Environment*, v. 145, p. 105–115, doi: 10.1016/j.rse.2014.01.009.
- Vonk, J.E., Sánchez-García, L., van Dongen, B.E., Alling, V., Kosmach, D., Charkin, A., Semiletov, I.P., Dudarev, O. V., Shakhova, N., Roos, P., Eglinton, T.I., Andersson, A., and Gustafsson, Ö., 2012, Activation of old carbon by erosion of coastal and subsea permafrost in Arctic Siberia: *Nature*, v. 489, p. 137–140, doi: 10.1038/nature11392.
- Walsh, J.E., Fetterer, F., Scott Stewart, J., and Chapman, W.L., 2017, A database for depicting Arctic sea ice variations back to 1850: *Geographical Review*, v. 107, p. 89–107, doi: 10.1111/j.1931-0846.2016.12195.x.
- Wang, X.L., Feng, Y., Swail, V.R., and Cox, A., 2015, Historical changes in the Beaufort-Chukchi-Bering Seas surface winds and waves, 1971-2013: *Journal of Climate*, v. 28, p. 7457–7469, doi: 10.1175/JCLI-D-15-0190.1.
- Wukelic, G.E., Gibbons, D.E., Martucci, L.M., and Foote, H.P., 1989, Radiometric calibration of Landsat Thematic Mapper thermal band: *Remote Sensing of Environment*, v. 28, p. 339–347, doi: 10.1016/0034-4257(89)90125-9.

Yang, D., Shi, X., and Marsh, P., 2015, Variability and extreme of Mackenzie River daily discharge during 1973-2011: *Quaternary International*, v. 380–381, p. 159–168, doi: 10.1016/j.quaint.2014.09.023.

## Appendix

---

Equations of the SPM model

$$C_L = \begin{cases} 1, & \text{if } R(\text{Red}) \leq 0.04 \\ 0, & \text{if else} \end{cases}$$

$$C_M = \begin{cases} 1, & \text{if } 2 \leq R\left(\frac{\text{Red}}{\text{NIR}}\right) \leq 4 \\ 0, & \text{if else} \end{cases}$$

$$C_H = \begin{cases} 1, & \text{if } R([\text{Red} + \text{NIR}]/2) \geq 0.03 \\ 0, & \text{if else} \end{cases}$$

$$C_1 = \begin{cases} 1, & \text{if } C_L + C_M + C_H = 0 \\ 0, & \text{if else} \end{cases}$$

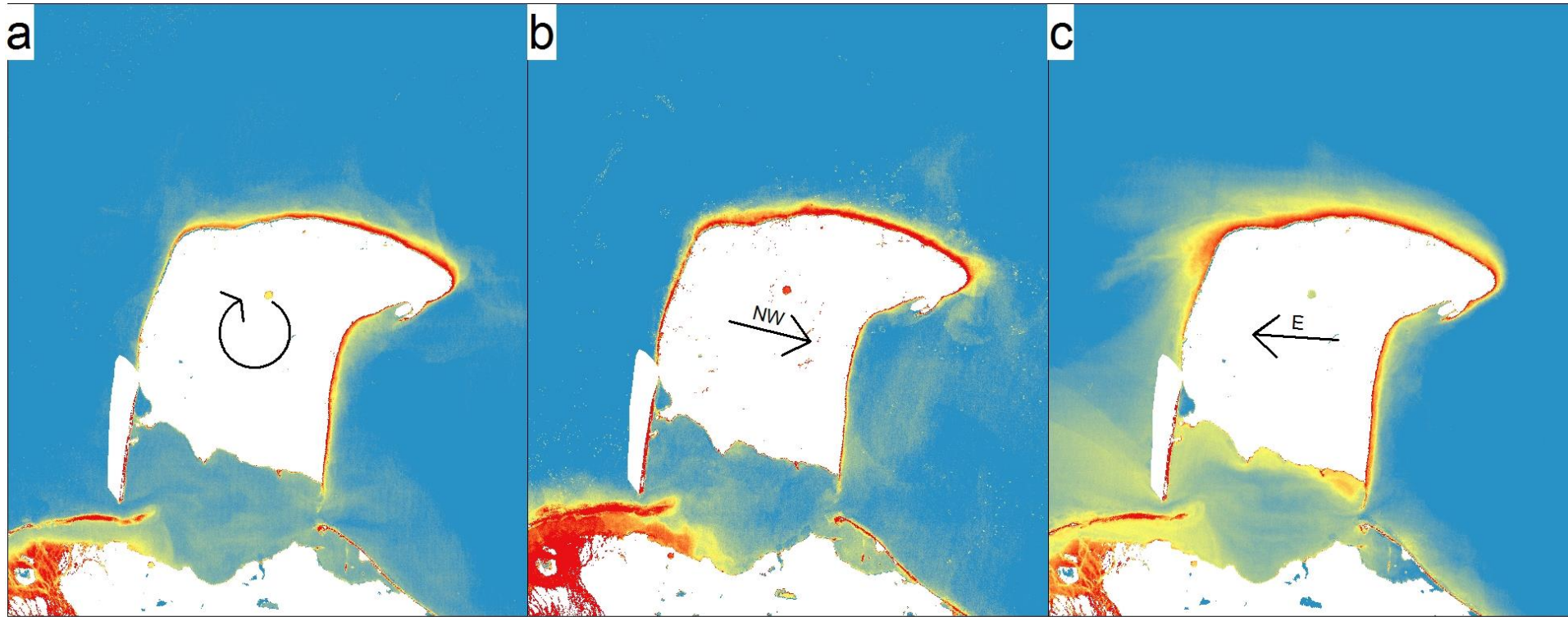
$$M_L = 100 \times R(\text{Red})^{0.86}$$

$$M_M = 7.41 \times R\left(\frac{\text{Red}}{\text{NIR}}\right)^{0.86}$$

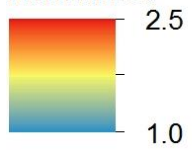
$$M_H = 662.25 \times R\left(\frac{\text{Red} + \text{NIR}}{2}\right)^{0.86}$$

MATLAB Script for creating Box and Whisker Plots with different colors for corresponding geographical orientations.

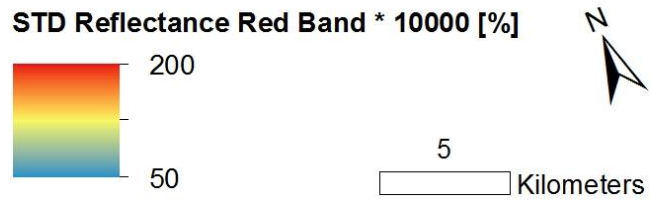
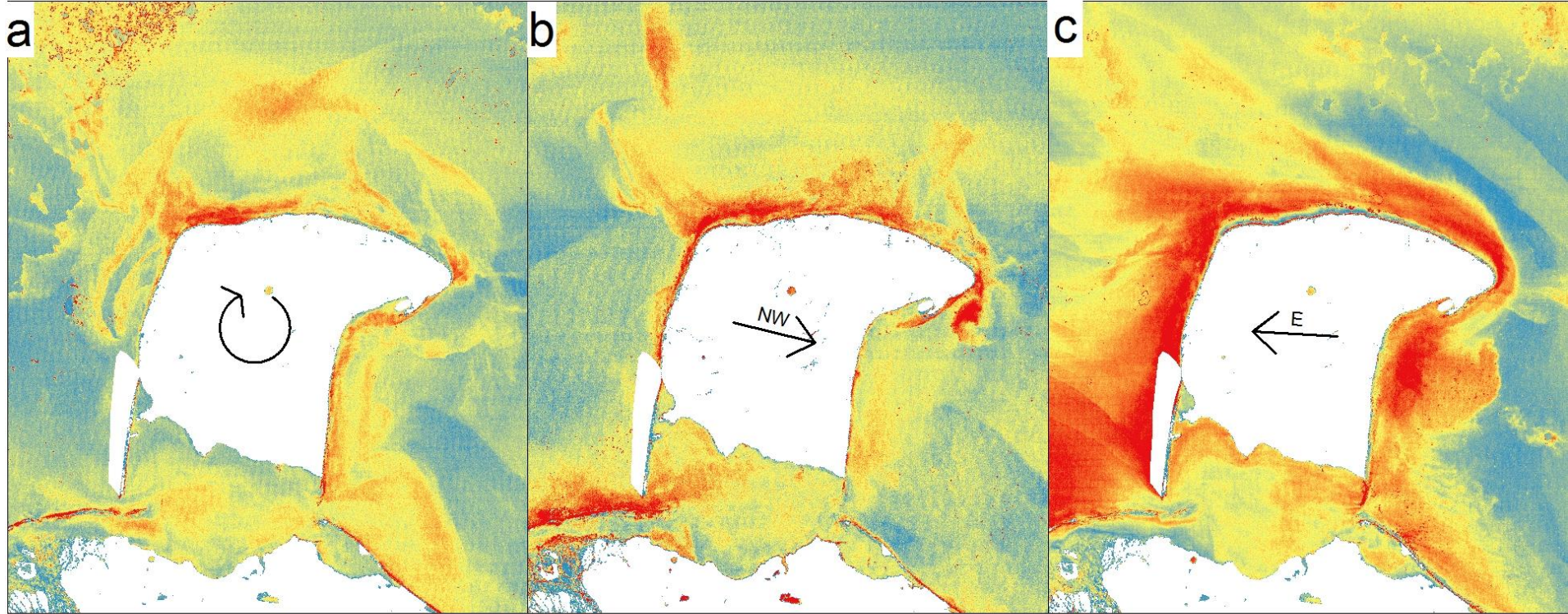
```
%% Build Boxplot with different colors for different orientations
x = load('e_all_2.txt'); %load data
boxplot(x, 'Notch', 'on') %notches indicate median
    h = findobj(gca, 'Tag', 'Box');
    for j=11:17 %count from back on
        patch(get(h(j), 'XData'), get(h(j), 'YData'), 'b');
    end
    for j=8:10
        patch(get(h(j), 'XData'), get(h(j), 'YData'), 'g');
    end
    for j=5:7
        patch(get(h(j), 'XData'), get(h(j), 'YData'), 'c');
    end
    for j=1:4
        patch(get(h(j), 'XData'), get(h(j), 'YData'), 'y');
    end
    title('Mean Surface Reflectance (red band) during stable E ...
           wind conditions')
    xlabel('Zone ID')
    ylabel('Mean Surface Reflectance *10000 [%]')
```



**Mean Reflectance Red Band  
Normalized**

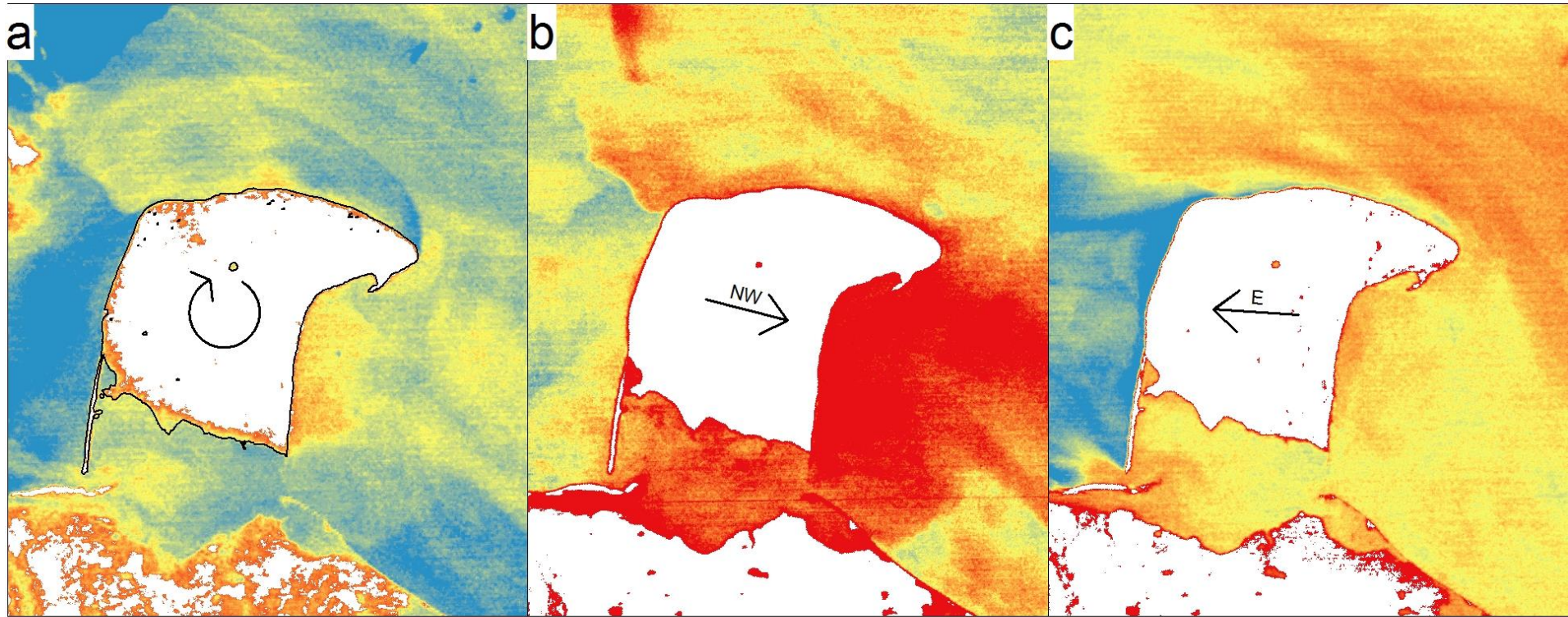


Normalized mean surface reflectance in the red band, that was used as proxy for turbidity, for (a) changing wind conditions, (b) stable NW wind conditions and (c) stable E wind conditions. Prevailing wind conditions are mentioned with arrows in the centre of each picture. The number of used scenes per wind condition can be seen in Table . Red areas indicate areas of high turbidity, white areas indicate land surfaces or areas of failed atmospheric correction.

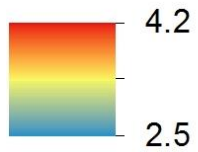


Standard Deviation of surface reflectance in the red band, that was used as proxy for turbidity, for (a) changing wind conditions, (b) stable NW wind conditions and (c) stable E wind conditions. Prevailling wind conditions are mentioned with arrows in the centre of each picture. The number of used scenes per wind condition can be seen in Table . Red areas indicate areas of high STD, white areas indicate land surfaces or areas of failed atmospheric correction.





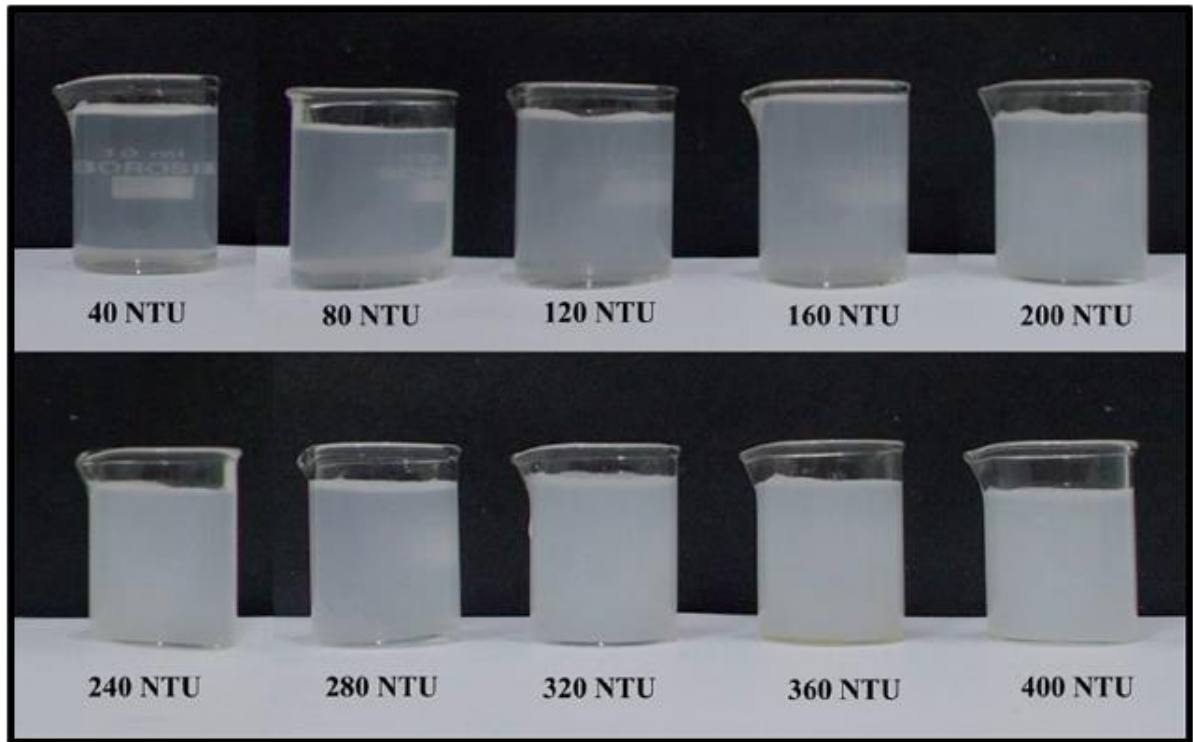
**STD At-Sensor Temperature (°C)**



5 Kilometers



Standard Deviation of at-sensor (uncorrected) temperature from thermal infrared channels, for (a) changing wind conditions, (b) stable NW wind conditions and (c) stable E wind conditions. Prevailing wind conditions are mentioned with arrows in the centre of each picture. The number of used scenes per wind condition can be seen in Table . Red areas indicate areas of high STD, white areas indicate land surface areas. Land surface areas were eliminated using the difference of land and SST. The shoreline of Herschel Island is drawn in black in figure (a), since the elimination was not distinct.



Selection of turbidity formazin standards (Hussein et al., 2016).

## Danksagung

---

Auch wenn am Ende nur mein Name auf dieser Masterarbeit steht, waren doch sehr viel mehr Leute daran beteiligt, denen ich hiermit meinen Dank aussprechen möchte.

An erster Stelle stehen dort meine Betreuer Hugues und Frank, die mir jederzeit mit Rat und Tat zur Seite standen. Natürlich gilt mein Dank auch Biggi, die, auch wenn sie nicht als Betreuer aufgeführt wird, erheblichen Anteil an der fachlichen Ausrichtung dieser Arbeit hat. Ebenso habe ich David zu danken, der mit seiner Kombination aus Fach- und Regionalwissen entscheidende Impulse bei der Entwicklung dieser Arbeit gab.

Allen anderen Kollegen vom AWI gilt mein Dank für die freundliche Arbeitsatmosphäre, sei es bei der täglichen Arbeit im Büro, auf Herschel oder während der obligatorischen Kaffeepause nach dem Mittag.

Die Anfertigung einer solchen Arbeit ist nicht ohne Freunde und Familie möglich. Manche von euch haben fachlich durch Diskussionen und Anregungen zu dieser Arbeit beigetragen, andere haben mich beim Bier trinken einfach nur auf andere Gedanken gebracht. Spezieller Dank gilt hierbei Steven, der dieser Arbeit einen professionelleren Anstrich verpasst hat.

Anne. Ich weiß nicht, wie ich dir angemessen in einem Satz danken soll. Ohne dich würde nicht nur diese Arbeit anders aussehen, sondern noch viele weitere Dinge meines Lebens.

Falls sich jemand nicht angemessen gewürdigt fühlt, bitte ich dies zu entschuldigen. Ich könnte mit Sicherheit eine weitere Masterarbeit nur über die mir entgegengebrachte Hilfe und Unterstützung schreiben.

## Eigenständigkeitserklärung

---

Hiermit versichere ich, dass ich die vorliegende Arbeit selbständig verfasst und keine anderen als die angegebenen Quellen und Hilfsmittel verwendet habe. Alle von Autoren wörtlich übernommenen Stellen, wie auch sich an die Gedanken anderer Autoren eng anlehrende Ausführungen meiner Arbeit, sind unter Angabe der Quelle kenntlich gemacht. Außerdem versichere ich, dass diese Arbeit in gleicher oder ähnlicher Fassung noch nicht Bestandteil einer Studien- oder Prüfungsleistung war.

Potsdam, 9. Oktober 2018

---

Konstantin Paul Klein